Investigating the influence of printing parameters, extruder design and material properties on the microstructure of high-temperature polymer composites in large-scale additive manufacturing.

M.X. van der Vaart

Delft University of Technology

CEAD

TU Delft

Investigating the influence of printing parameters, extruder design and material properties on the microstructure of high-temperature polymer composites in large-scale additive manufacturing.

by

M.X. van der Vaart

to obtain the degree of Master of Science

at the Delft University of Technology,

to be defended publicly on Thursday, April 3rd, 2025, at 8:45 AM.

Student number:	4753887	
Project duration:	September 1, 2024 – April 16, 2025	
Thesis committee:	Dr. G.A. Filonenko,	TU Delft, Supervisor
	Dr. M.J.M Hermans	TU Delft
	Ir. M. Muilwijk,	CEAD B.V.

An electronic version of this thesis is available at http://repository.tudelft.nl/.

Preface

The aim of this thesis is to investigate the problems arising during the printing of high-temperature polymer composites using an extruder system, as well as their effect on the microstructure of the printed material. This is done by analysing the printing parameters and microstructure using characterisation methods like microscopy. I chose this subject because, in the world of material science, I am particularly interested in polymer materials and the mechanics behind polymer materials. Combining this with the fascinating technology of additive manufacturing is a perfect combination for me to grow in this field.

For helping me in this learning process, I want to thank my supervisor from CEAD, Mark Muilwijk, and my supervisor from the TU Delft, Georgy Filonnenko. Furthermore, I want to thank Marcel Hermans for being part of my thesis committee and all the colleagues at CEAD who were always ready to help me with questions. Lastly, I want to thank my family and girlfriend, Rozemarijn Schraven, for supporting me in this sometimes emotionally turbulent time and particularly to my father, Frank van der Vaart, for taking the time to give me feedback on this report.

I hope after reading this thesis, the reader is as excited about large-scale additive manufacturing and polymer composite processing as I was during the investigating process and expands the reader's knowledge about this still upcoming technology.

M.X. van der Vaart
Delft, March 2025

Summary

Large-scale additive manufacturing for high-temperature polymer composites presents challenges in printability and microstructure, limiting its overall application. As it prevents certain industries from benefiting from the potential automation and reduction in waste. This thesis investigates the influence of printing parameters and extruder design on the printability and microstructure of high-temperature polymer composites.

To address this, a series of experiments were conducted to analyse the effects of various printing parameters, which are material number, printing dimensions, volumetric output, and heating zone temperatures. Additionally, the impact of nozzle pressure and design modifications, such as nozzle insulation, was evaluated. The microstructure was assessed using microscopy to determine the void content.

The results indicate that nozzle insulation significantly affects the required torque and void content of semi-crystalline polymer composites. However, heating zone 1 was identified as a limiting factor for high-temperature amorphous polymer composites, as its heating band did not provide sufficient heat to the barrel. Furthermore, the experiments revealed that viscosity plays a crucial role in both the extruder system's performance and the microstructure of printed parts.

These findings highlight the importance of optimizing printing parameters and extruder design to expand the applicability of high-temperature polymer composite printing, for example, a greater range of volumetric outputs. It is recommended that additional pressure and temperature sensors be installed between different screw regions for better insight into extrusion behaviour. Additionally, a nozzle design for viscosity measurement is proposed as a cost-effective alternative to high-temperature rheology testing. Lastly, implementing a heated hopper is suggested to homogenize the granulate temperature before extrusion, further improving process stability and as a solution to the problems with heating in heating zone 1.

Contents

List of Figures

List of Tables

Nomenclature

This part still needs to be done

Abbreviations

Abbreviation	Definition
ANOVA	Analysis of Variance
Avg	Average
CNC	Computer Numerical Control
CRDZ	Continuous Rotating Displacement Zone
DSC	Differential Scanning Calorimetry
FDM	Fused Deposition Modelling
FFF	Fused Filament Fabrication
HDPE	High-density Polyethene
LAC	Linear Attenuation Coefficient
Micro-CT	Micro Compute Tomography
PC	Polycarbonate
PE	Polyethene
PEEK	Polyether Ether Ketone
PEKK	Polyether Ketone Ketone
PESU	Polyether Sulphone
PIR	Post-Industrial Recyclate
PPS	Polyphenylene sulphide
Std	Standard deviation

Symbols

Symbol	Definition	Unit
A	The pre-exponential constant	[s^{-1}]
C_p	Heat capacity at constant pressure	[$J/mol * K$]
D_b	The inner diameter of the barrel	[m]
D_s	The outer diameter of the screw	[m]
e	The flight width	[m]
E_a	The activation energy for viscous flow	[J/mol]
F	The F-value for ANOVA analyses	[$-$]
F_d	Shape factor for the drag flow	[$-$]
F_p	Shape factor for the pressure flow	[$-$]
F_s	Surface area	[m^2]
f_F	Friction coefficient between polymer and barrel surface	[$-$]

Symbol	Definition	Unit
f_l	Correction term for leakage flow through the flight clearance	[$-$]
f_v	Friction coefficient between polymer and screw surface	[$-$]
G	Gibbs free energy	[J]
ΔG	Difference in free Gibbs energy between two phases	[J]
ΔG_v	Difference in Gibbs energy per volume unit between crystal and liquid state	[J/m^3]
H_e	Enthalpy	[$J/mol * K$]
H	Flight height	[m]
H_{Bead}	Height of the printed bead	[m]
H_{opt}	Optimal flight height	[m]
k	The flow consistency index	[$Pa * s^n$]
L_s	The axial distance of one complete turn of the flight known as the Lead	[m]
$M_{material}$	Material number	[$-$]
N	The frequency of rotations	[rpm]
N_{data}	The number of datasets or the number of tests performed	[$-$]
P	Dimensionless pressure	[$-$]
P_{back}	Backpressure	[Pa]
ΔP_{feed}	Pressure difference in the feeding zone	[Pa]
ΔP_{comp}	Pressure difference in the compression zone	[Pa]
ΔP_{meter}	Pressure difference in the metering zone	[Pa]
Q_h	The heat flow per second	[J/s]
Q_v	Volumetric output	[m^3/s]
r_c	The critical nuclei radius	[m]
r_n	Radius of the nucleus	[m]
R	Gas constant	[$J * mol^{-1} * K^{-1}$]
T_1	Temperature at surface 1	[K]
T_2	Temperature at surface 2	[K]
T_m	The melting point	[K]
T	The temperature of the polymer melt	[K]
v_b	A constant velocity in direction b	[m/s]
v_bx	The x component of the constant velocity in direction b	[m/s]
v_by	The y component of the constant velocity in direction b	[m/s]
W	The width of the pitch	[m]
W_{bead}	Width of the printed bead	[m]
Z_s	Dimensionless distance along the screw length	[$-$]
$x..$	The mean value of the whole matrix or mean value of all tests	[$-$]
$x.j$	Mean value of column j or the mean value of each test	[$-$]
xij	Value in the matrix at the ij-th position or the i-th position of the j-th test	[$-$]

Symbol	Definition	Unit
y	Distance on coordinate axis along the screw channel	[m]
z	Distance on the coordinate axis down the screw channel	[m]
I	The transmitted intensity	[W/m^2]
I_0	The incident X-ray intensity	[W/m^2]
x	Thickness of the sample	[m]
α_c	The drag flow coefficient	[m^3]
β_c	The pressure flow coefficient	[m^3]
δ_f	The clearance between barrel diameter and the screw outer diameter	[m]
η	The spindle or screw speed	[rpm]
η_{actual}	Actual screw speed	[m/s]
γ_c	The filtration flow coefficient	[m^3]
γ_s	The surface tension energy created by the difference between crystal and liquid state	[J/m^2]
κ_c	The head geometrical constant	[m^3]
λ	Thermal conductivity	[$kg * m * s^{-3} * K^{-1}$] or [$J * s^{-1} * m^{-1} * K^{-1}$]
μ	Viscosity	[$kg * m^{-1} * s^{-1}$] or [$Pa * s$]
μ_c	Linear attenuation coefficient	[m^{-1}]
ϕ	The angle between the flight and normal plane to the axis known as the helix angle	[°] or [rad]
ϕ_{opt}	Optimal helix angle	[°] or [rad]
τ	Shear stress	[$kg * m^{-1} * s^{-2}$] or [Pa]
$\dot{\gamma}$	Shear rate	[s^{-1}]
θ_b	The angle at which the flat plate moves to the down channel direction	[°] or [rad]

1 Introduction

The introduction explains the motivation and problem, followed by the research scope and research questions arising from the literature findings and reasoning about the problems.

1.1. Motivation and problem introduction

The advancement of 3D printing offers benefits by reducing waste in manufacturing processes that require frequent design modifications. Unlike traditional material removal processes such as Computer Numerical Control (CNC) machining, 3D printing uses additive manufacturing, which minimises excess material usage. Compared to other production techniques, additive manufacturing has great benefits regarding automation possibilities, decreasing the personnel needed to create a product. An example of this is boats made of high-density polyethene (HDPE). Now, these boats are made by welding different HDPE parts to each other, requiring many hours of skilled welding personnel.

Another example is the production of large patterns for sand-casting moulding, generally made of wood or metal, requiring a skilled worker. Automatisation allows the 3D printer to be used in a push of the bottom production and work continuously compared to a worker. ”Therefore, since its development in the mid-1980s, the market for 3D printing has experienced consistent growth, driven by its potential to innovate across various industries” [21]. The upscaling and development of 3D printers have further broadened their industrial applications. However, this upscaling and development introduces new design challenges that must be addressed to fully exploit the technology’s potential.

One particular challenge is using 3D printing in high-end applications, such as parts for the aviation industry. Printing with high-temperature thermoplastic polymers is required for these high-end applications, as these polymers have good mechanical and thermal properties. The problem with high-temperature polymers is their high melting and processing temperature due to their high thermal stability. Resulting in higher requirements from the system. Due to these higher requirements, the printability of high-temperature polymers is currently limited, and the quality of printed material is low due to the amount and shape of voids in the microstructure. These voids weaken the mechanical strength of the printed structures and, in the case of large macro voids, could result in unwanted textures, limiting the effectiveness and applicability of large-scale 3D printing. A high-end application with great potential is the production of seals between piping; the void content must be very low for this application to work correctly. Therefore, a better understanding of why these voids are created is needed as to what factors influence this process.

Another significant problem with the printability of high-temperature polymers is layer adhesion between deposited layers. There are two crucial factors in this problem. The first is the large difference between the printed polymer temperature and ambient temperature, resulting in faster cooling. The second is the time the system needs to finish one layer, also known as the layer time. The layer time is influenced by the length of the path and the speed the system needs to take to finish one layer. For the speed, it is important to have a range of volumetric outputs at which the system can operate, which is currently limited for high-temperature polymers.

This is due to problems with the need for high forces to extrude the high-temperature polymers, lowering printing speed, thus decreasing layer time, and increasing the problem with the printing layer adhesion. Another aspect of layer adhesion is the semi-crystalline nature of high-temperature polymers such as Polyether ether ketone (PEEK), Polyether ketone ketone (PEKK) and Polyphenylene sulphide (PPS). The semi-crystalline nature decreases the mobility of the polymer chains as it cools down below its crystallisation temperature, decreasing layer bond strength, further explained in section 2.2.10.

So, addressing the printability problems for high-temperature polymer composites in large-scale additive manufacturing is motivated by the desire to increase the potential applications for which the process could decrease production cost, time and waste.

1.2. Research Scope

The problem with the printability of high-temperature polymers due to poor layer adhesion is outside the scope of this thesis as research has already been performed by Consul et al., and a solution has already been proposed to solve this problem with their LEAM technology. ”Using continuous spectrum light to heat the material just before the nozzle welds the layers together” [23]. Also, CEAD itself works on integrating a previous layer temperature sensor, which gives feedback on the printing speed so it stays within the desired range.

Therefore, this thesis aims to examine the influence of improving printability by analysing the data generated by sensors on the system and the void content visible in the microstructure of high-temperature polymer composites. It will also examine the influence of printing parameters on semi-crystalline and amorphous polymers and potential extruder design improvements. The printing parameters are used as input for the system to operate. These printing parameters are the material number, printing dimensions, volumetric output, and the temperatures of heating zones, further explained in section 5.1.

1.3. Research Questions

Given the challenges associated with the printability of high-temperature polymer composites, as discussed in section 1.1 and the research gap found due to reviewing the literature as given in section 2, the following research question for this thesis is proposed.

”What is the influence of printing parameters, extruder design and material properties on printability and microstructure of high-temperature polymer prints?”

To accompany the research question, Further sub-research questions are proposed:

1. *”What is the influence of printing parameters on the printability and microstructure of high-temperature polymer composite prints?”*
2. *”Which aspect of extruder design influences the printability and the microstructure of high-temperature polymer composite prints, and how could they be improved to minimize void content?”*

2

Fundamental and Literature research

This chapter explains the fundamentals and the findings from the literature to give the reader an understanding and insights into the problems and motivation of what this thesis will explore and where the research questions are based on.

2.1. Fundamentals

This section describes the fundamental knowledge needed to understand this thesis. It begins by explaining high-temperature polymers and polymer physics, followed by the fused granulate additive manufacturing technology.

2.1.1. High-temperature thermoplastic polymers

The difference between thermoplastics and thermosets is thermoplastics can soften as heat is applied, after which it can be reshaped and hardened when cooled, creating a reversible process. In contrast, thermosets harden irreversibly and can not be reshaped due to the formation of irreversible cross-links between polymer chains, limiting the mobility of chains at elevated temperatures.

High-temperature thermoplastic polymers are, therefore, polymers which become softer and reformable at relatively high temperatures. These are also often called high-performance polymers because they retain their desirable properties when exposed to harsh conditions like high temperatures. ”These conditions also include but are not limited to corrosive environments and high pressures” [6]. An essential part of the strength of high-performing polymers is the bonding energy of atoms, which, when higher, makes it harder to break the polymer chains. ” The bond energy of $\mathrm{C-C}$ is $83\,\mathrm{kcal\,mol^{-1}}$, $\mathrm{C=C}$ is $145\,\mathrm{kcal\,mol^{-1}}$, $\mathrm{C-H}$ is $99\,\mathrm{kcal\,mol^{-1}}$, $\mathrm{C-F}$ is $123\,\mathrm{kcal\,mol^{-1}}$” [6].

Furthermore, the aromatic components in the backbone increase the overall strength of the polymer chain. This is due to the resonance-stabilisation estimated to be adding between ”$40\,\mathrm{to}\,70\,\mathrm{kcal\,mol^{-1}}$” [6]. Resonance stabilisation is due to the de-localisation of the electron, as it is not strictly localised due to the π orbital system representing the double bond of the aromatic ring, shown in figure 2.1. This decreases the total energy in the system, therefore adding more stability.

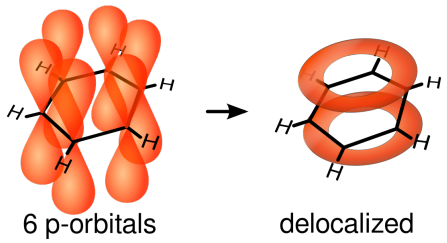

Figure 2.1: Aromatic π system [3].

2.1.2. Crystallinity

As explained in the book written by Van der Vegt and Govaert [24], Crystallinity in polymer science is influenced by polymer chain alignment, creating a lattice structure. In polymers, the structure never fully crystallises but creates regions of crystal structure; these polymers are called semi-crystalline polymers. Not all polymers create crystalline structures; polymers that do not create a crystalline structure have a random structure, also known as an amorphous structure and these are called amorphous polymers. In figure 2.2, a classification is shown on the most commonly used polymers divided by amorphous/semi-crystallinity and the different categories based on the long-term service temperature of the polymers.

Crystallisation in polymers primarily depends on the regularity of the polymer chain, which is influenced by the characteristics of the side groups. Symmetry plays an important role, as crystallinity increases when identical atoms or groups are positioned opposite each other in the chain. Similarly, asymmetrical side groups with minor size differences and consistent placement along one side of the chain enhance crystallinity. The rigidity of the chain, which often results from unsaturation, also contributes to the likelihood of crystallisation. Additionally, the chain must mostly adopt a cis or trans configuration to maintain the structural regularity needed for crystallisation. However, it is essential to note that not all polymers crystallise spontaneously, as sometimes the crystallisation rate is too slow for the crystallisation to occur under typical conditions.

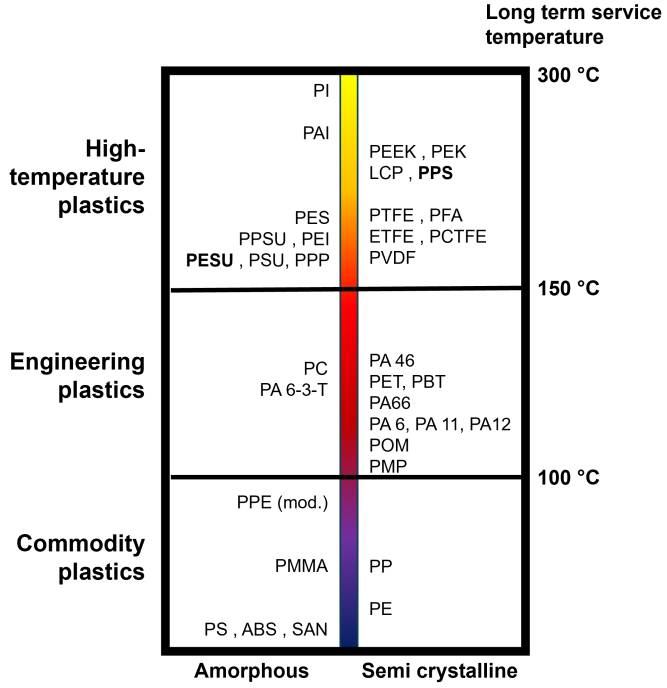

Figure 2.2: Classification of polymers based on the long-term service temperature and if it is semi-crystalline or amorphous

Crystallisation has two stages: nucleation formation and crystal growth. The condition for creating crystals is they have formed from a nucleus. Nucleus creation has two types: Heterogeneous nucleation and homogeneous nucleation. Heterogeneous nucleation is due to impurities or additives enhancing crystallisation. Homogeneous nucleation can be due to the presence of nuclei due to fluctuations in density and conformations of the polymer chain.

At the melting point, the nucleation speed is zero and increases by lowering temperatures, creating an undercooling of the polymer melt. If we assume the nucleus to be spherical at a specific temperature, then two factors influence the radius of the crystal: The decrease of free enthalpy due to the difference between crystal and liquid state and the increase of free enthalpy due to the formation of a surface between crystal and liquid, creating a surface tension given by equation 2.1 [24].

$$\Delta G = -\frac{4}{3}\pi * r_n^3 * \Delta G_v + 4\pi * r_n^2 * \gamma_s \tag{2.1}$$

With ΔG_v the difference in free enthalpy per volume unit between crystal and liquid state, γ_s the surface tension energy created by the difference between crystal and liquid state, r_n radius of the nucleus. If the temperature stays constant, a specific maximum radius is also known as the critical nuclei sizes needed for crystallisation. This critical radius is calculated by setting the derivative of equation 2.1 equal to zero, resulting in equation 2.2 [24].

$$r_c = \frac{2\gamma_s}{\Delta G_v} = \frac{2\gamma_s * T_m}{\Delta H * (T_m - T)} \tag{2.2}$$

With r_k the critical nuclei radius, T_m the melting point, T the temperature of the polymer melt and ΔH the change in enthalpy due to phase transformation. The equation states when increasing the degree of undercooling denoted by $(T_m - T)$, the smaller the critical nucleus radius becomes; therefore, more nuclei become stable and undergo the crystallisation process.

The growth of crystals is driven by the difference in free enthalpies between the liquid and crystal state, which increases with decreasing temperature. However, an opposing factor is the mobility needed for the polymer chains to untangle and glide along each other. Therefore, it is influenced by the melt viscosity of the polymer. The melt viscosity becomes higher at lower temperatures and also depends on the length of the polymer chains. For this reason, crystallisation rates can differ. These opposing forces result in a difference in crystallisation rate at different temperatures and a maximum, as shown in figure 2.3. Generally, the maximum crystallisation rate becomes less at longer polymer chain lengths.

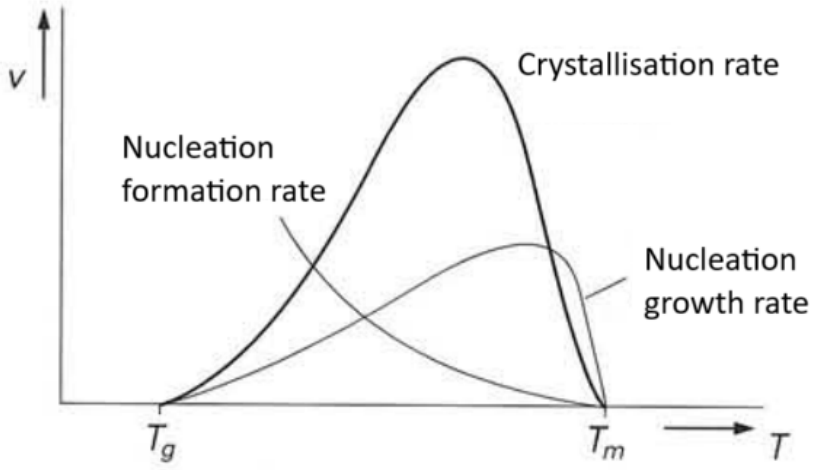

Figure 2.3: Crystallisation rate graph [24].

2.1.3. Viscosity of polymer melts

In liquids, viscosity can be understood as the internal resistance to flow, which arises from momentum transport between a series of thin fluid layers under a shear force. So when this shear force is applied, it creates a velocity gradient, as shown in figure 2.4. The force per unit area needed to make this momentum is known as the shear stress. The speed at which these layers move relative to each other is known as the shear rate.

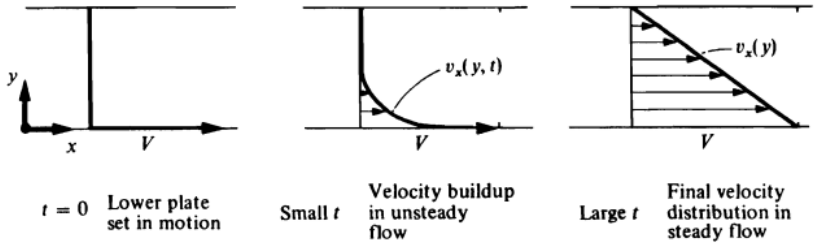

Figure 2.4: Velocity profile of fluid flow between two parallel plates [19].

In thermoplastic polymer melts the polymer chains can move separately from each other. However, the chains do entangle; therefore, when a force is applied, the chains need to untangle in order to flow. Unlike other liquids like water, polymers require more force to flow, resulting in higher viscosity than other liquids.

The viscosity of polymers is very dependent on molecular mass. When molecular mass is higher, the polymer chains are longer or have large side groups, resulting in more entanglements. This requires more force to untangle, making it harder for the polymer melt to flow.

Fluids can exhibit different flowing behaviours visually represented by figure 2.5 showing shear stress versus shear rate graph.

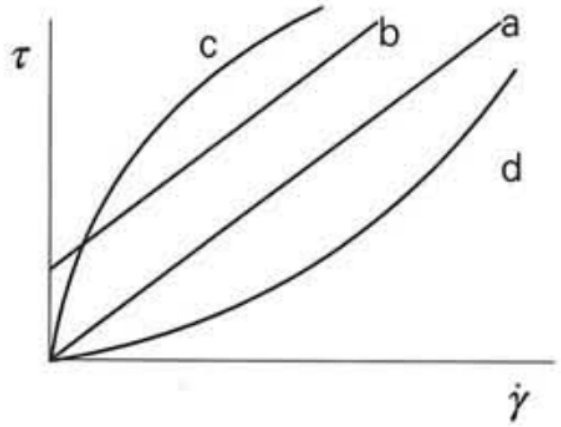

Figure 2.5: Shear stress versus shear rate graph of the different flowing behaviours: a = Newtonian, b = Bingham plastic, c = Pseudoplastic, d = Dilatant [24].

Fluids like water exhibit Newtonian flowing behaviour, meaning the shear stress is linearly related to the shear rate, resulting in a constant viscosity as shown in equation 2.3 [24]. However, polymer melts usually exhibit pseudoplastic flowing behaviour, meaning less shear stress is needed with an increasing shear rate, resulting in a viscosity dependence on the shear rate. To quantify this, the power law describes the relationship between shear stress and shear rate shown in equation 2.4 [24]. Inserting the power law 2.4 into the viscosity equation 2.3 results in the equations for the viscosity of pseudoplastic given by equation 2.5.

$$\mu = \frac{\tau}{\dot{\gamma}} \tag{2.3}$$

$$\tau = k * (\dot{\gamma})^n \tag{2.4}$$

$$\begin{aligned} \mu &= k * (\dot{\gamma})^{n-1} \\ \mu &= k^{\frac{1}{n}} * \tau^{\frac{n-1}{n}} \end{aligned} \tag{2.5}$$

With μ the viscosity, k the flow consistency index, $\dot{\gamma}$ shear rate and n power law index. For pseudoplastic flow behaviour, the power law index is smaller than one. It should be noted that the power law fails for small power law index values.

Viscosity also depends on the temperature of the polymer melt due to the increased mobility of chains at higher temperatures. This dependency is generally described by the Arrhenius equation shown in equation 2.6 [24].

$$\mu = A * e^{\frac{E_a}{R*T}} \tag{2.6}$$

With μ the viscosity, A the pre-exponential constant, E_a the activation energy for viscous flow, R gas constant and the T absolute temperature of the polymer melt.

2.1.4. Thermal conductivity

Thermal conductivity is a material property that determines how much energy per second flows through one meter of material for every degree of temperature difference. In other words, it is how well the material conducts heat. It is defined by equation 2.7 [24].

$$\frac{Q_h}{t} = \lambda * F_s * \frac{T_1 - T_2}{d_c} \tag{2.7}$$

with Q_h the heat flow per second, λ the thermal conductivity, t the time, F_s surface area, d_c thickness and T_1, T_2 the surface temperatures.

Generally, polymers have relatively low thermal conductivity compared to other materials, such as metals. This can pose difficulties with processes using heating to melt the polymer to create products like the extrusion process. "Using fillers like fibres can increase the thermal conductivity by three to fourfold." [24], therefore selecting the right filler material can help with heating up the polymers.

2.1.5. Fused granulate additive manufacturing

The book by Lafleur and Vergnes [13] gives an overview of polymer extrusion based on different studies over the years, giving a good overview of what information is available on the extrusion process. One of the chapters is about the single-screw extruder. What becomes clear in the book is that the extruder exists of different screw regions, all having a different function and, therefore, various mechanisms influencing a certain region.

The main geometrical characteristic of a single screw extruder system consists of three different zones. The first zone is the feed zone, also known as the solid conveying zone, with a constant channel department and the transported material in a solid state. This zone contains two sub-zones: a friction-based zone where the material is still in a completely solid state and transported forward, which is governed by friction generated at the barrel's interface. The second subzone is a region where, at the barrel interface, a small molten polymer film is formed. This small molten polymer film develops a velocity gradient, creating a shear stress on the compacted solid particles and a forward transport in the extruder. The film's thickness gradually increases until it researches the flight gap's height. This tends to be right before the next zone. So, the feed zone has two functions: compacting the solid particles to reach a higher density, reducing the amount of air between particles and heating up the solid particles, so the molten polymer film researches the height of the flight gap at the start of the melting zone.

The second zone is the melting zone, also known as the compression zone, where sold material progressively melts. Here, the molten film becomes thicker than the flight gap, resulting in the scrapping of molten material and creating a molten melt pool at the trailing flight. The channel geometry differs along the zone as the channel depth decreases, creating back pressure. This back pressure is intended to push potentially entrapped air out of the polymer melt.

The third zone is the metering zone, where only molten material is present and has a constant channel depth. This channel depth is smaller than the channel depth of the feed zone. This region homogenises and stabilises the flow before the polymer melt enters the nozzle or region right before the nozzle.

2.2. Literature review

This section reviews the existing literature on large-scale composite additive manufacturing, identifying past research and highlighting the knowledge gaps this thesis aims to address.

2.2.1. Difference between inter-bead and intra-bead voids

The literature on 3D printed materials identifies two primary types of voids: inter-filament (or inter-bead) voids and intra-filament (or intra-bead) voids, as discussed by Jang et al. [7] and Papon and Haque [17]. In industry terminology, ”bead” refers to the material after it has been printed, while ”filament” refers to the material before printing. Consequently, this review adopts the terms inter-bead and intra-bead voids to describe voids within 3D printed structures.

Inter-bead voids are the gaps between adjacent beads of printed material. These voids are influenced by several critical parameters: layer height, extrusion rate, print rate, and nozzle diameter. Jang et al. [7] conducted an extensive study on high solids-loaded polymer composite filaments, which exhibit stiffer behaviour and are less prone to deformation.

When a high solids-loaded filament is extruded through a circular nozzle, it tends to retain its circular cross-section if not properly deformed, leading to significant inter-bead voids. Performance metrics in their study included mean line width, the aspect ratio between width and height, and cross-sectional area. Additionally, micro-computed tomography and optical scanning were employed to visualise and quantify the void area between printed layers below and above a critical printing height.

The findings from Jang et al. suggest that in stiffer, high solids-loaded filaments, print parameters, particularly the nozzle height, greatly influence the formation of inter-bead voids. The critical nozzle height is the most crucial factor in determining the extent of voids between layers, showing the importance of precise control over this parameter in reducing defects.

On the other hand, Intra-bead voids are voids within the bead itself, typically resulting from trapped air during the printing process. While Jang et al. did not specifically study intra-bead voids, they noted the likelihood of air bubbles being trapped during ink preparation, especially in highly packed particle filaments. However, the study did not include these voids in its void area measurements, leaving a gap in understanding the full impact of intra-bead voids on the material properties.

Further research by Papon and Haque explored the effects of nanofibre concentrations and nozzle geometries on void content and tensile properties in fused deposition modelling (FDM) Papon and Haque. Their work highlighted that inter-bead voids are largely determined by the geometry of the printed beads and the thermodynamic parameters that govern solidification. Intra-bead voids were linked to the melt flow characteristics, which can lead to air entrapment and subsequent defects during solidification.

Another defect in 3D printing is the bonding defect between printed layers. This defect arises when the thermal energy of the semi-molten material is insufficient to raise the interface temperature between layers above the glass transition temperature or the crystallisation temperature. Failure to achieve this temperature results in weak layer bonding and structural weaknesses.

Despite these insights, the research by Jang et al. and Papon and Haque was limited to small-scale nozzle components and did not involve pellet extruders commonly used in large-scale additive manufacturing. This highlights the need for further investigation into the upscaling of these processes, particularly concerning the formation and impact of intra-bead voids. Although the existing studies mention the possible formation of these voids due to factors like water evaporation, they do not provide an analysis.

Further literature research on the formation of intra-bead voids due to the extrusion process was scarce to non-existent. This resulted in analysing different aspects of the extrusion process to investigate the influence of extruder design and input parameters on the formation of intra-bead voids.

2.2.2. Design hurdles due to upscaling

The study by Shah et al. [21] discusses the various challenges faced in the design of large-scale 3D printers, particularly those encountered in the market at the time. The paper includes designing and

testing a prototype for large-scale printing with thermoplastic polymers. However, the focus is predominantly on fused filament fabrication (FFF), which utilises filament produced from pellets rather than directly employing a pellet extruder.

One key issue is the increased mass of filament spools, which leads to higher torque demands on the motors. To mitigate this, the authors suggest a pellet extruder fed by a hopper could be a more effective solution. Pellet extruders offer several advantages, such as greater versatility and the ability to use recycled materials. However, the paper also notes a drawback: pellet extruders are slower than standard 3D printers. Confusingly, the authors later state that ”They are also typically much heavier, which can pose vibrational issues during fast printing” [21], creating a contradiction that is not fully addressed in the discussion.

Another significant challenge discussed is warping, a common issue resulting from temperature differentials during printing. As illustrated in Figure 2.6, warping needs more precise environmental control and can lead to increased printing times. The authors suggest that a wider nozzles could be used to reduce printing time and mitigate this issue. However, these design challenges, while important, fall outside the primary scope of the research question and are not explored in detail.

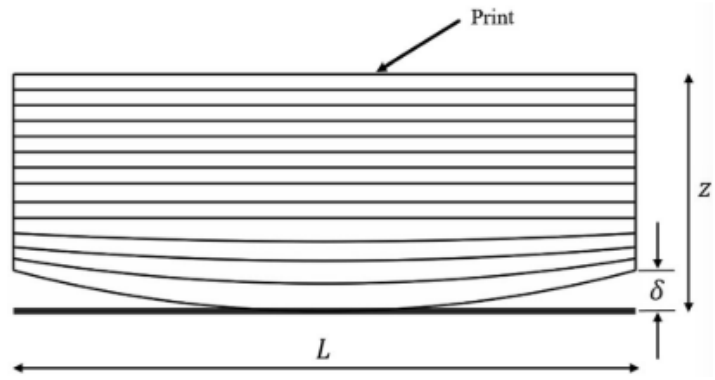

Figure 2.6: Visualization of warping [21].

2.2.3. Extruder design in pellet operated 3D printers

In the book by Krishnanand et al. [12], a chapter examines the design of extruders in pellet-operated 3D printers, with particular attention to single-stage and double-stage extruder designs. The author explains the challenges of different flexible and non-flexible materials and how these influence the extruder’s operation. Unlike fused filament fabrication (FFF), which uses a continuous filament, pellet-operated 3D printers can handle flexible materials due to the mitigation of buckling issues, as illustrated in Figure 2.7.

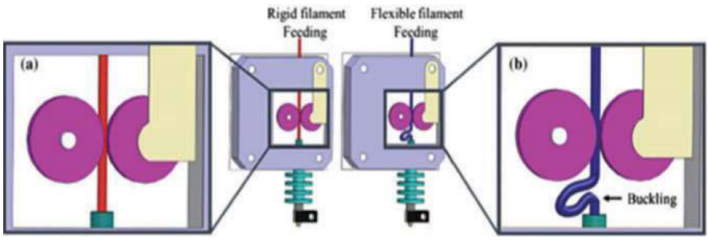

Figure 2.7: Geometry of a square pitched single flighted screw [12].

The double-stage extruder design offers more control over the extrusion process. In this setup, as shown in figure 2.8, the first stage is responsible for melting the material and increasing pressure. In contrast, the second stage focuses on plasticising and precisely controlling the flow of the melted material. The screw speed in the first stage directly affects the pressure in the second stage, providing

a means of regulating the extrusion process. Additionally, a vent hole is strategically placed between the two stages to allow trapped air to escape, thereby improving the quality of the extruded material.

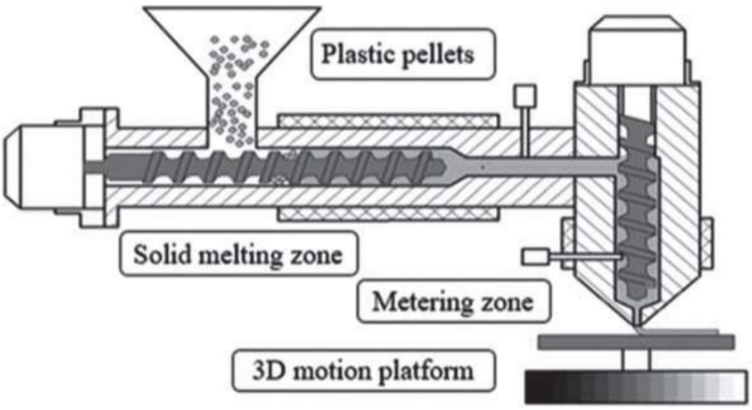

Figure 2.8: [12].

One specific case discussed involves a single-screw extruder design, further explored in the work of Wankhade and Bahaley [26], which describes the development of a plastic filament extruder for producing 1.75 mm diameter ABS filament, which is comparable to fused granulate additive manufacturing. The 3D printer used by Wankhade and Bahaley uses a horizontal 3D filament-making machine made out of a hopper onto a cylinder containing a screw for extrusion. This system is similar to the nozzle design of CEAD's pellet extruders. However, a noticeable difference is in the orientation of the extruder in the paper, which is horizontal compared to the vertical orientation of the pellet extruders of CEAD.

The volumetric flow of the extruder is generated by three distinct types of flow: drag flow, driven by the screw's rotation; pressure flow, resulting from pressure differences; and flow filtration, which occurs due to the clearance between the screw and the barrel. The equation for calculating volumetric flow is presented in Equation 2.8 [26], with each type of flow represented by a specific coefficient: α_c the drag flow coefficient, β_c the pressure flow coefficient, and γ_c the filtration flow coefficient. κ_c the head geometrical constant and η spindle or screw speed also play critical roles in determining flow rates.

$$Q_v = (\frac{\alpha_c * \kappa_c}{\kappa_c + \gamma_c + \beta_c}) * \eta \tag{2.8}$$

The flow coefficients and the head geometrical constant are calculated using the equations in 2.9 [26], which consider factors such as D_s the outer diameter of the screw, L_s the axial distance of one complete turn of the flight known as the Lead, h_c the initial channel depth, ϕ the angle between the flight and normal plane to the axis known as the helix angle, e the flight width, m number of channels, L The axial length of the screw, and δ_f the clearance between barrel diameter and the screw outer diameter.

$$\begin{aligned} \alpha_c &= \frac{\pi * m * D_c * h_c * (\frac{L_s}{m} - e) * \cos\phi^2}{2} \\ \beta_c &= \frac{m * h_c^3 * (\frac{L_s}{m} - e) * \sin\phi * \cos\phi}{12 * L} \\ \gamma_c &= \frac{\pi^2 * D_c^2 * \delta^3 * \tanh\phi}{10 * e * L} \\ \kappa_c &= \frac{\pi * D_c^4}{128 * L} \end{aligned} \tag{2.9}$$

However, the analysis presented in the book does not account for the influence of viscosity on drag flow, an important factor in extrusion processes. Moreover, there is a lack of detailed explanation or

references for determining the specific percentages for each section of the screw length, as well as for the calculation of the helix angle. The calculation of melting power is also incomplete, as it does not consider the contribution of friction-induced heat generation within the extruder.

2.2.4. Screw design development for 3D printing biopolymer pellets

The paper by Whyman, Arif, and Potgieter [28] provides a detailed examination of an extrusion system tailored for 3D printing with biopolymer pellets. The study presents three of the most commonly used screw designs, along with their corresponding pressure profiles, as illustrated in Figure 2.9

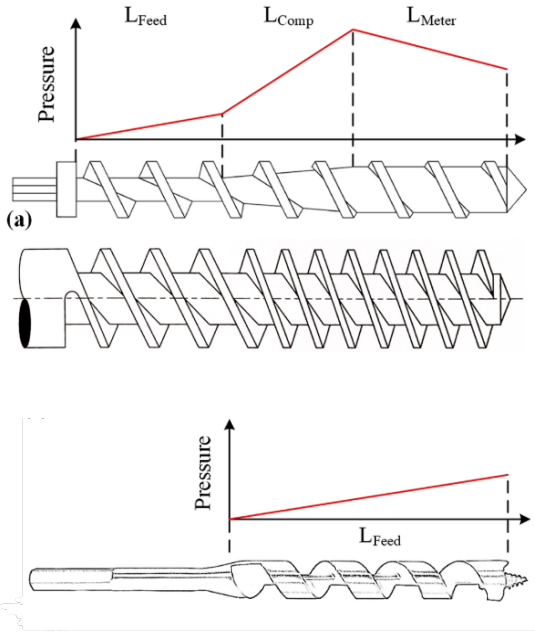

Figure 2.9: Three extruder screw designs, with corresponding pressure profile [28].

As shown in Figure 2.9, a transparent pressure gradient opposes the direction of material flow. The figure also highlights the distinct pressure gradients within the three primary zones of the screw: the feed zone, the compression zone, and the metering zone. The total back pressure generated across these zones is calculated by using Equation 2.10 [28].

$$P_{back} = \Delta P_{feed} + \Delta P_{comp} + \Delta P_{meter} \tag{2.10}$$

Due to the smaller setup size and the associated challenges with weight restrictions for a sufficiently powerful motor, the chosen design was an auger drill bit. This decision eliminates the compression and metering zones, simplifying the back pressure calculation to account solely for the feed zone, which is an important part of reducing void content.

2.2.5. Pressure influence

Chapter 6, section 3 of the book by Tadmor and Gogos [22] offers a detailed examination of the single extruder functioning as a pump, with an emphasis on the geometric parameters, as illustrated in Figure 2.10. While the basic concepts are laid out, evaluating the model reveals some limitations that could impact its applicability in real-world scenarios.

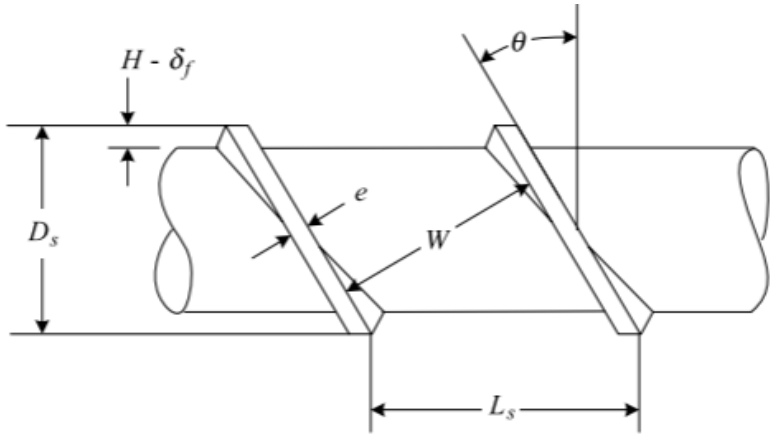

Figure 2.10: Geometry of a square pitched single flighted screw [22].

With L the axial length of the screw, D_s the outer diameter of the screw, D_b the inner diameter of the barrel, H the height of the flight, W the width of the pitch, L_s the axial distance of one complete turn of the flight known as the Lead, e the flight width, θ the angle between the flight and normal plane to the axis known as the helix angle and δ_f the clearance between barrel diameter and the screw outer diameter.

The model presented simplifies the complex geometry of the screw and barrel system into an unwound rectangular channel with the barrel surface becoming a flat plate and moving with v_b a constant velocity in direction b as depicted in Figure 2.11. Which can be subdivided into x directional velocity of v_{bx} and z directional velocity v_{bz} given by equations 2.12 and 2.13 [22]. This transformation allows for a more straightforward mathematical treatment but at the cost of key factors, such as the influence of curvature and varying cross-sectional areas along the screw's length. These simplifications may result in deviations from actual performance, especially in non-ideal conditions where factors like back pressure, die geometry, and non-Newtonian fluid behaviours are prevalent.

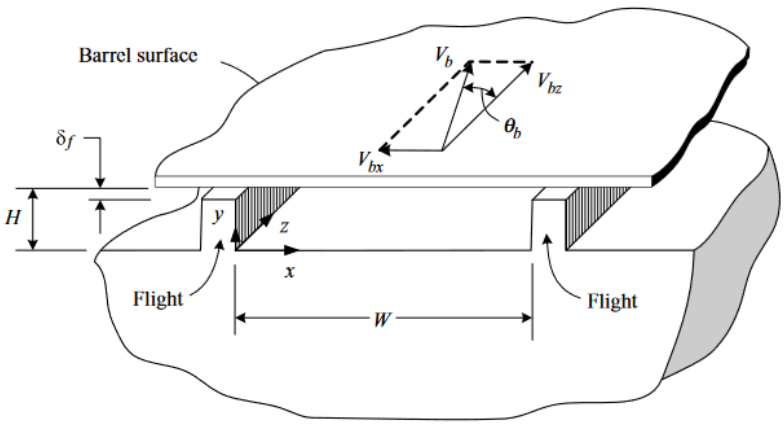

Figure 2.11: Geometry of the unwound channel [22].

$$v_b = \pi N D_b \tag{2.11}$$

$$v_{bx} = v_b \cos\theta_b \tag{2.12}$$

$$v_{bz} = v_b \sin\theta_b \tag{2.13}$$

With N the frequency of rotations and θ_b the angle between at which direction the flat plate moves to the down channel direction.

The isothermal Newtonian model assumes a constant temperature and viscosity throughout the process. However, this assumption fails to capture the thermal gradients and variable shear rates in the polymer extrusion process, particularly in large-scale or high-volumetric output processes. Not including these factors can lead to inaccuracies in predicting the flow rate and pressure distribution, ultimately affecting the reliability of the extruder's performance predictions.

The assumptions outlined in the model, such as incompressible flow, steady-state conditions, and fully developed flow, simplify the equations, enabling an analytical approach to solution derivation. However, these assumptions do not necessarily reflect the complexities encountered in the extruder process. For example, the assumption of incompressibility might not hold in scenarios involving high pressures or compressible materials, leading to potential errors in the calculated flow rates.

From the x-directional equation of the Navier stokes, the velocity profile in the channel can be estimated. A Vector field of the cross-channel with an aspect ratio of 5 is shown in figure 2.12

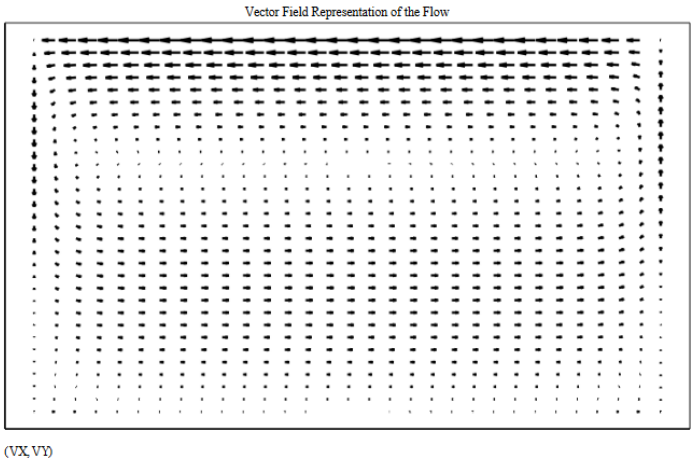

Figure 2.12: Vector field of the xy plane flow [10].

With the z-directional velocity profile, a net volumetric flow rate can be calculated and integrated over $\zeta = y/H$ and $\chi = x/W$ resulting in the equation and to represent the actual situation better; a term f_L is introduced to describe the continuous leakage flow from downstream location to upstream locations 2.14 [22].

$$Q_v = \frac{v_{bz} W H}{2} F_d + \frac{W H^3}{12\mu} \left(-\frac{\delta P}{\delta z} \right) F_P (1 + f_L) \tag{2.14}$$

F_d and F_p are shape factors for drag and pressure flow calculated by equations 2.15 and 2.16 [22], which it becomes apparent that both functions are only influenced by H/W ratio.

$$F_d = \frac{16W}{\pi^3 H} \sum_{i=1,3,5}^{\infty} \frac{1}{i^3} \tanh\left(\frac{i\pi H}{2W} \right) \tag{2.15}$$

$$F_p = 1 - \frac{192H}{\pi^5 W} \sum_{i=1,3,5}^{\infty} \frac{1}{i^d} \tanh\left(\frac{i\pi W}{H} \right) \tag{2.16}$$

Furthermore, the model's handling of leakage flow in equation 2.17 [22] introduces a corrective term, f_L, to account for the leakage from downstream to upstream. However, it is tricky to determine the precise fluid viscosity between the fight and barrel.

$$f_L = \left(\frac{\delta_f}{H}\right)^3 \frac{e}{W}\frac{\mu}{\mu_f} + \frac{\left(1+\frac{e}{W}\right)\left[\frac{1+\frac{e}{W}}{\tan^2\theta} + \frac{6\mu v_{bz}(H-\delta_f)}{H^3\left(\frac{\delta p}{\delta z}\right)}\right]}{1+\frac{\mu}{\mu_f}\left(\frac{H}{\delta_f}\right)^3\frac{e}{W}} \tag{2.17}$$

The paper's authors also describe the challenges of non-Newtonian viscosity, non-isothermal effects, and geometric factors such as curvature correction. As the authors acknowledge, these elements introduce complexity that prevents analytical solutions. Such a model would provide more accurate predictions of flow dynamics, enhancing the design optimisation of extrusion systems.

In conclusion, the model presented by Tadmor and Klein provides a helpful starting point for understanding the basic mechanics of single-screw extrusion; its limitations are recognised assumptions made while simplifying the mathematics and do not fully capture the complexities of real-world extrusion processes. Therefore, careful consideration is needed when applying the model to non-Newtonian fluids in the presence of thermal differences and complex geometries.

2.2.6. Shear thinning influence on design optimilization

In their paper, Orisaleye et al. [16] delve into the dynamic behaviour of single screw extruders within the food industry; mainly focus is to optimise design parameters for processing shear-thinning plastics, also known as pseudoplastic. The authors propose a model that uses rheological characteristics to predict and perform optimising both the channel depth and helix angle of the screw within the constraints of the power-law index range $\left(\frac{1}{\sqrt{2}} \leq n \leq 1\right)$.

The authors derive their mathematical model using the Navier-Stokes equations to describe the flow in the down-channel, or z-direction, of a rectangular channel. The assumptions made by Orisaleye et al. are comparable to those made by Tadmor and Gogos and aimed at simplifying the mathematics of the extrusion process. For instance, they assume steady flow conditions, negligible inertial forces, and an isothermal material in the channel. While these assumptions enable analytical solutions, they also introduce limitations. For example, assuming a constant temperature disregards the thermal gradients in extrusion processes, mainly when dealing with pseudoplastic materials with highly temperature-dependent viscosity. This could lead to an inaccurate prediction of flow characteristics, as the model does not account for the temperature-induced viscosity variations that occur during extrusion. However, it simplifies the Navier-Stokes equation for the z-direction to equation 2.18 [16].

$$\frac{dp}{dz} = \frac{d}{dy}\left(\mu\frac{dv_z}{dy}\right) \tag{2.18}$$

Together with the power law for shear dependence of viscosity and introducing dimensionless parameters using the screw diameter as a base parameter, the equation for the optimum channel depth and optimal helix angle is obtained as given in equation 2.19 and 2.20 [16].

$$\Phi_{opt} = \tan^{-1}\left[\frac{(2n^2+n)^{\frac{1}{2}}}{2n+1}\right] \tag{2.19}$$

$$H_{opt} = \left[\frac{(n+1)}{n}\left(\frac{dP}{dZ_s}\right)^{\frac{-1}{n}}\cos\phi\right]^{\frac{n}{n+1}} \tag{2.20}$$

Moreover, the assumption is that negligible leakage flow might not hold in practical applications, especially in systems where precise control over flow rates and pressure is critical. Neglecting this aspect could result in deviations between the model's predictions and the actual performance of the extruder. Similarly, assuming that the material exhibits purely viscometric behaviour with only one velocity component v_z oversimplifies the flow dynamics that can occur in an extruder.

Another oversight in the model is not including the variations in helix angle and channel depth along the screw length. The channel depth may vary much. By not accounting for variations, the model potentially overlooks factors that influence the efficiency and output of the extrusion process.

Another shortcoming of the paper is the absence of a complete figure illustrating the dimensions and geometry used in their analysis. Such a figure would have provided clearer insight into how the various parameters interact and affect the extrusion process.

In summary, the work of Orisaleye et al. offers insights into the behaviour of shear-thinning materials in single screw extruders. However, the model's reliance on simplifying assumptions raises concerns about its applicability to more complex scenarios. The neglect of factors such as temperature variation, leakage flow, and geometric changes along the screw suggests that the model may not fully capture the extrusion process.

2.2.7. Friction coefficient influence

In the chapter on single-screw extruder design of the book written by Lafleur and Vergnes, "The flow of the material results from the action of the screw flights on the polymer in contact with the inner wall of the barrel. If the polymer sticks to the screw, the extrusion does not proceed. On the other hand, the flow improves if the polymer sticks to the barrel." [13].

Further in the book, an explanation is given for grooved barrels, which are used to increase the adherence of particles to the barrel wall. Also, the importance of friction coefficients and the ratio between the barrel and screw is explained. However, the friction coefficients are difficult to determine as they are influenced by the material, contact pressure and interface properties. An assumption can be made that the pressure and material are consistent at a given place in the channel. Thus, only interface properties are important. Roughness is a factor in interface properties that can deviate from the material. Investigating the influence of the roughness of the barrel on printing parameters could result in interesting findings.

A model by Tadmor and Gogos is also described in the book for the solid conveying zone, with assumptions like the solid is in contact with the barrel, the screw and the flights, the depth of the channel is constant, and the density of the material is continuous.

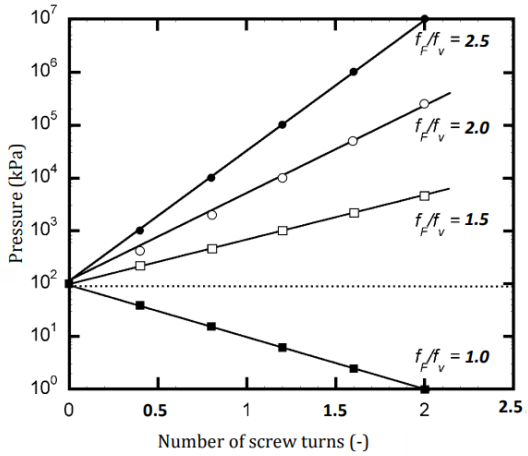

Figure 2.13: Pressure vs the number of screws turns for different friction coefficient ratios [13].

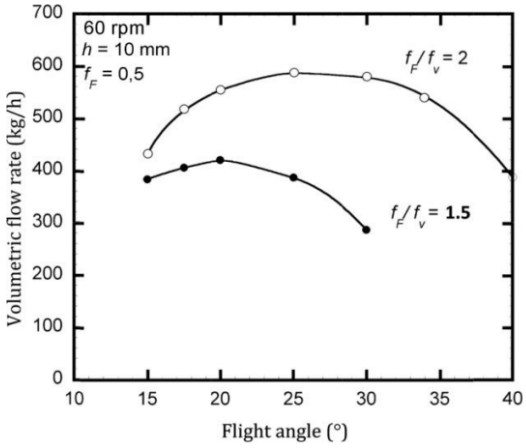

Figure 2.14: Volumetric flow rate vs flight angle for different FOC ratios [13].

From this model, it is found that "the flow rate of the solid depends on the geometry of the feed zone and the friction coefficients via the ϕ angle and is proportional to the rotation speed of the screw" [13], where friction coefficient between polymer and screw is denoted as f_v and the friction coefficient between polymer and barrel f_F.

The potential flow rate is greater, with a higher friction coefficient on the barrel. However, optimisation of the flight angle should also be considered, as shown in figure 2.14.

To conclude, the importance of the friction coefficient is highlighted, and the problems with properly determining the friction coefficients are mentioned. However, it gives a valuable inside into the importance of surface interactions between the polymer melt and the screw and barrel of the extruder.

2.2.8. Thermodynamic influence

Research on the melting of ABS filament was performed by Curmi and Rochman [5] and by Altınkaynak et al. [1].

Both papers make use of the Tadmor analytical model for single screw extruders based on the melting behaviour in a screw extruder first studied by Maddock. Therefore, the Maddock melting mechanism is named after Maddock. This describes that first, the polymer melts as a thin film in between solid pellets and the screw channel. However, the Tadmor model assumes constant solid bed velocity along the length of the screw, which is known to be not correct due to the complex interaction between solid particles. The Tadmor model can predict the ratio of the filled channel with the solid bed.

The paper by Altınkaynak et al. uses a three-dimensional finite element simulation and performed screw freezing experiments to compare to the numerical simulations to predict the velocity profile. A cross-section of a velocity profile is shown in figure 2.15. It is also interesting to note that the molten polymer melt pool accumulates at the farthest part of the channel extrusion direction, as shown in figure 2.16.

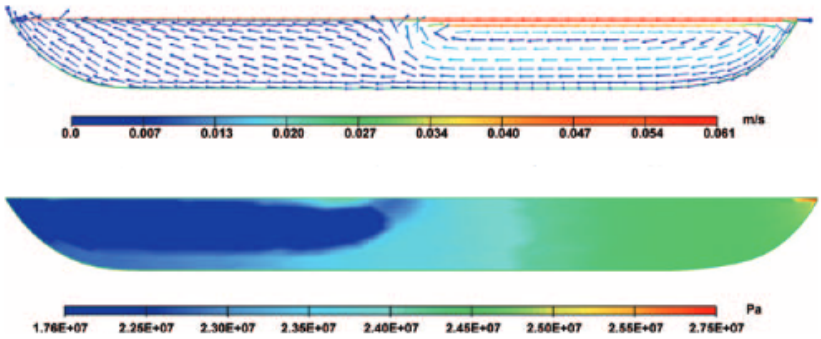

Figure 2.15: Velocity (top) and pressure (bottom) profile at cross section 12 times the screw diameter[1].

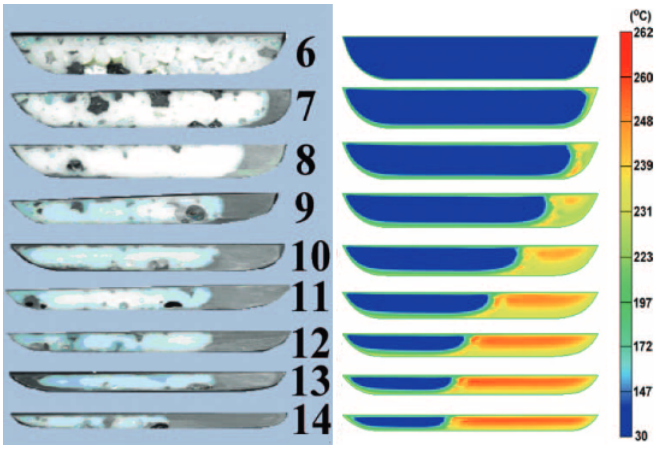

Figure 2.16: Melting profile done by screw freezing experiment (right) and by Tadmor model (left) [1].

Both are exciting studies and give a general idea of the melting behaviour and velocities profile. This knowledge could be considered in finding a solution to the void reduction, as shown in figure 2.16.

2.2.9. Barrier screw designs and Maddock mixing element

Barrier screw designs, including Maddock mixing elements, are commonly used in extrusion processes to enhance the efficiency and quality of material melting and mixing. As explained by Rauwendaal [20], these designs offer significant advantages in optimising the optimising performance of extruders by managing the distribution of solid and melted material within the screw channel.

A barrier screw introduces an additional flight, known as the barrier flight, which has a smaller height than the primary flight. This design effectively divides the screw channel into two sections: one where the melted polymer accumulates and another where the solid material is retained. As the solid material melts, it transitions from the solid bed channel to the melt pool, gradually increasing the proportion of the melted polymer along the screw length as shown in figure 2.17.

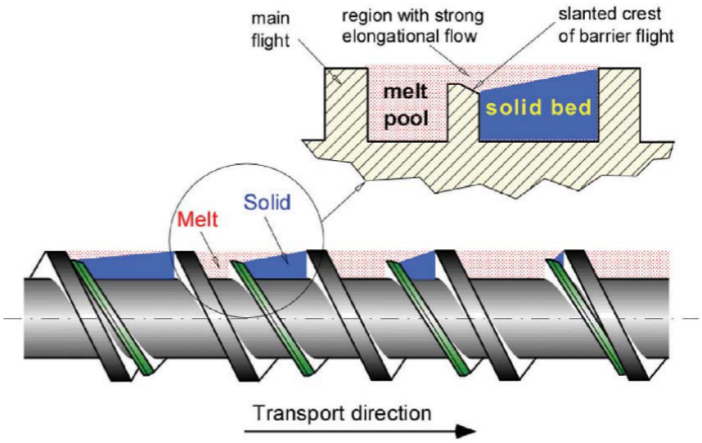

Figure 2.17: Cross section of the concept of barrier screw design[20].

However, barrier screws are not without their drawbacks. Introducing a barrier flight increases viscous dissipation, leading to higher melt temperatures and greater power consumption. The shearing flow created by the flat barrier flight can also result in lower stresses within the melt and less effective dispersion of agglomerates and droplets. This is problematic in applications requiring high-quality mixing, where uniform dispersion is critical.

To address some of the limitations of traditional barrier screws, advanced designs such as the Maddock mixing element and the Continuous Rotating Displacement Zone (CRDZ) barrier have been developed. These designs aim to enhance elongational flow, which is more effective for mixing homogenisation shearing flow.

The Maddock mixing element, as shown in Figure 2.18, incorporates a spiral structure that generates elongational flow, improving the dispersion of additives and the homogeneity of the melt. The CRDZ design, as shown in Figure 2.19, developed by Rauwendaal Extrusion Engineering, further enhances this effect by introducing a continuous rotating displacement zone that promotes efficient mixing and reduces the risk of overheating.

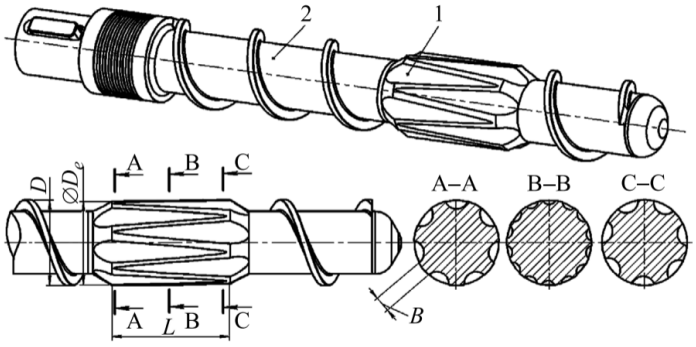

Figure 2.18: Cross section of Maddock mixing design[18].

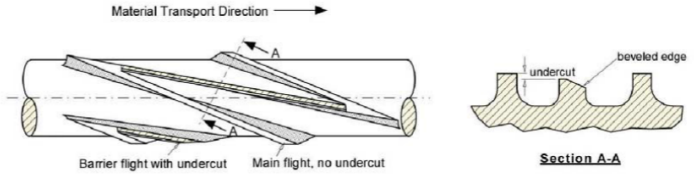

Figure 2.19: Cross section of CRDZ design [20].

Performance testing of these designs on a 130 mm extruder, as reported by Rauwendaal, demonstrated that the CRDZ design achieved higher specific throughput, lower specific energy consumption, and lower melting temperatures compared to the Maddock design as shown in figure 2.20. These results suggest that the CRDZ design may offer better performance in applications requiring high throughput and efficient energy use.

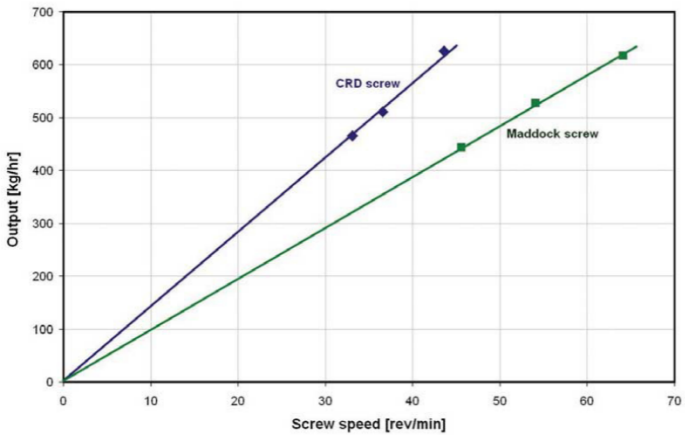

Figure 2.20: Specific throughput vs screw speed of CRDZ and Maddock design[20].

However, it is essential to approach these findings with some caution. The research was published by a researcher with a patent on the CRDZ design, raising potential concerns about bias. Moreover, the original paper was not accessible for independent verification, further limiting the ability to evaluate the reported results critically.

In a related study, Podyman, Dvoinos, and Novik [18] developed a mathematical model to evaluate the homogenisation process of polyethene (PE) composites with silicone rubber using a single-extruder screw equipped with a Maddock element. This model, which was experimentally verified, provided

insights into the impact of the Maddock element's geometric dimensions on the mixing quality and melt temperature as shown in Figure 2.21.

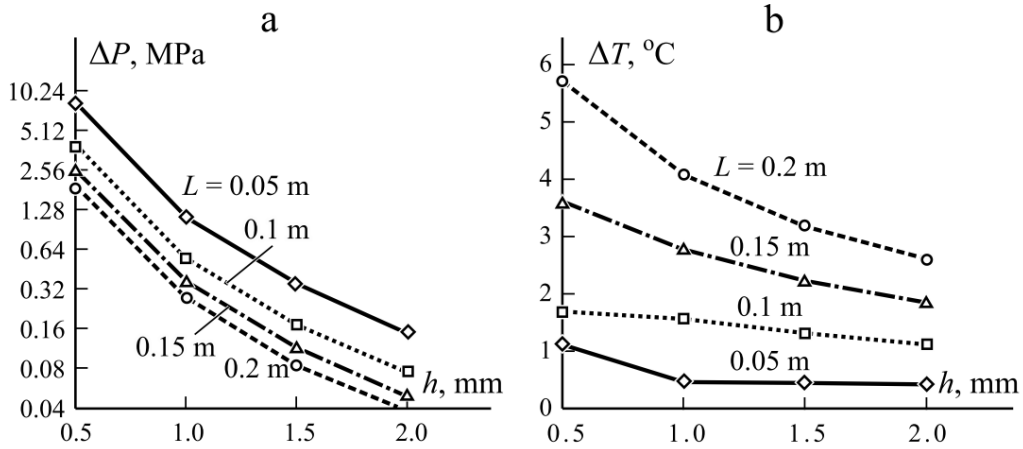

Figure 2.21: Graph a Hydraulic resistance vs gap height and Graph b the overheating temperature vs gap height[18].

The study found that the proposed model effectively calculated the final melt temperature and the degree of deformation within the (PE) composite. It also demonstrated that increasing the channel length of the Maddock element or incorporating a spiral structure could enhance both deformation and mixing efficiency. For materials with a low coefficient of friction, the study highlighted the need to experimentally test the extruder's pressure characteristics to ensure optimal performance. Additionally, the research suggested that in industrial production, implementing a cascade system with cooling between extruders could prevent overheating, thereby improving the overall quality of the final product.

In conclusion, barrier screw designs, particularly advanced configurations like the Maddock and CRDZ elements, offer benefits for the extrusion of complex materials. They focus mostly on enhancing mixing and offer some benefits for enhancing the melting process. However, it is unknown what effect these screw designs will have on reducing voids. Also, independent validation of these designs is important to ensure that performance claims are reliable and applicable across different extrusion scenarios.

2.2.10. Layer adhesion

Layer adhesion is an important part of improving the overall use of 3D printing as it increases the mechanical strength in the normal direction of the printing. Consul et al. [4] investigated the layer adhesion, also known as the interlaminar strength of large-scale additive manufacturing of polyether ether ketone (PEEK) carbon composites. The reason for testing PEEK is due to its high crystallisation rate introducing problems with laminar strength. It uses a model to measure the degree of bonding based on the reptation time, which is the time a long polymer chain needs to move through an entangled network.

"Three elements are needed to determine the degree of healing: interface temperature at which bonding occurs, welding time at interface temperature, and if the material is amorphous or semi-crystalline, which determines if healing can happen." [4]. The next step in the research is investigating the crystallisation behaviour through differential scanning calorimetry; this technique gives inside at which temperature melting and crystallisation occur, which is more extensively explained in section 3.2.2.

The results of mechanical three-point bending tests correlate with the predictions of the relaxation times and DSC curves. It is stated that "The underlying theory of fusion bonding, considering the material amorphous until the onset of crystallisation, seems to be valid." [4]. This means that although crystallisation starts under the melting point as explained in section 2.1.2, the effect on the mobility of polymer chains is not significant enough till the onset of crystallisation temperature is reached.

This research highlights the importance of the movement of polymer chains for interlaminar bonding strength, for which the reaction time and crystallisation rate play important parts.

2.3. Knowledge gap

Performing this literature research gives an interesting insight into extruder design aspects and material properties that can potentially influence the microstructure of high-temperature polymer printed material, specifically the void content. It discusses problems for printability due to upscaling to large-scale additive manufacturing and explains different models related to volumetric output and pressure inside extruders. Furthermore, it touches on design optimisation for shear-thinning polymers and different screw designs like the barrier screw and Maddock mixing element. Lastly, it goes into depth about the research done on the melting mechanisms. However, there was little to no information on analysing microstructure in composite large-scale additive manufacturing due to printing parameters and extruder design. This means there is a knowledge gap on how the extruder design, material properties and printing parameters influence the microstructure of polymer composites in large-scale additive manufacturing.

3

Methods and materials

This chapter explains the production and characterisation method for the samples produced for this thesis. It further outlines all the materials used based on data-sheets and general information from the literature.

3.1. Production method

This section explains all the equipment for producing additive-manufactured prints, which are used to investigate the influence of printing parameters and extruder design on printability and microstructure.

The complete system is called the box printer, as is shown in figure 3.1; it is named the box printer as the machine is made to only create boxes. The box printer only uses a 3-axis system, also known as a gantry system, compared to the 7-axis system of robotic printers. Giving robotic printers more flexibility in their reach and the possibility to change their printing orientations. The box printer is equipped with a bead layer temperature sensor, which can measure the bead temperature in both the x directions, giving an inside look at the surface temperature of the previous bead in one direction and of the bead, which is freshly printed in the other x direction. The box printer also measures the screw speed and torque force the servo applies to the screw. The system is set up so that the screw speed is linked to the volumetric output. It should be noted that the box printer is also an older system; therefore, it works slightly differently compared to newer printers and has an older type of servo. Furthermore, the system slows down and speeds up at every corner, which correlates with slowing down and speeding up of the screw speed and creating fluctuations in the servo torque, screw speed, and nozzle pressure at every corner. Therefore, average values are used to filter out these fluctuations.

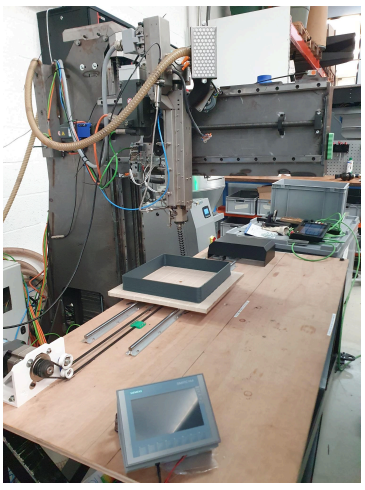

Figure 3.1: Box printer.

Furthermore, due to a delay in volumetric output, when the screw speeds up or slows down, the corners show the differences in bead thickness. Therefore, samples are taken from the middle section between two corners. Looking at the requirements for testing the printability and influence on microstructure and working around the limitations of the box printer results in a setup sufficient enough to perform the tests. It also has the benefit that it doesn't require sophisticated software and knowledge like robotic printers. As this thesis focuses on the performance and microstructure of high-temperature polymer composites, the printing shape and limitation in reachable printing area and orientation are unimportant. Another reason for using the box printer is it has a nozzle pressure sensor, which generates valuable data to better understand the system. This nozzle pressure sensor is not installed in other systems.

The box printer has a display where input settings can be inserted. In the program tab, as shown in figure 3.2, here are the bead dimensions and tool-path settings by adjusting the box side length and corner radius. In the extra settings on the programme tab, as shown in figure 3.3, the material number and printing speed explained in section 5.1.1 and first layer extrusion can be put in. Where the first layer extrusion is a volumetric output multiplier for only the first layer for better print-bed adhesion.

Figure 3.2: Box printer programme tab display.

Figure 3.3: Box printer programme extra settings display.

In the extruder tab, the heating zones can be inserted into the right column as shown in figure 3.4 corresponding to the heating zones highlighted in figure 3.5. The left column is the barrel temperature measured by the thermocouples inside the barrel.

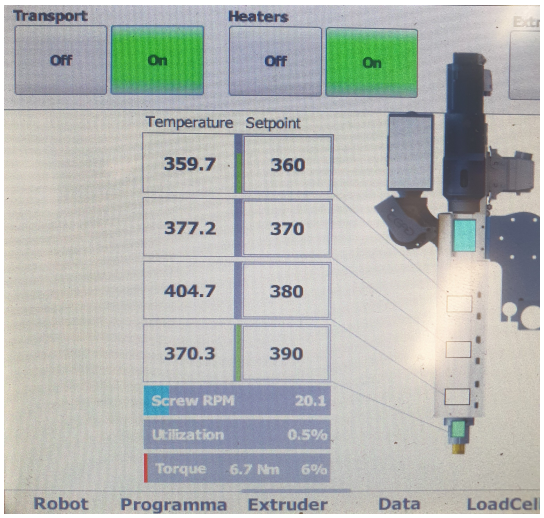

Figure 3.4: Box printer extruder tab-display.

On the box printer is an S25 extruder, of which a cross-section is shown in figure 3.5. The S25 extruder has four heating zones; the first heating zone corresponds to the feed/solid conveying zone. The second heating zone is the melting/compression zone. The third is the metering/molten zone. The fourth does not correspond to a screw zone but to a hollow region before the nozzle. Each heat zone is heated with ceramic heating bands, and heating is regulated by thermocouples, positioned at the red arrows in figure 3.5 and placed a couple of millimetres from the barrel wall.

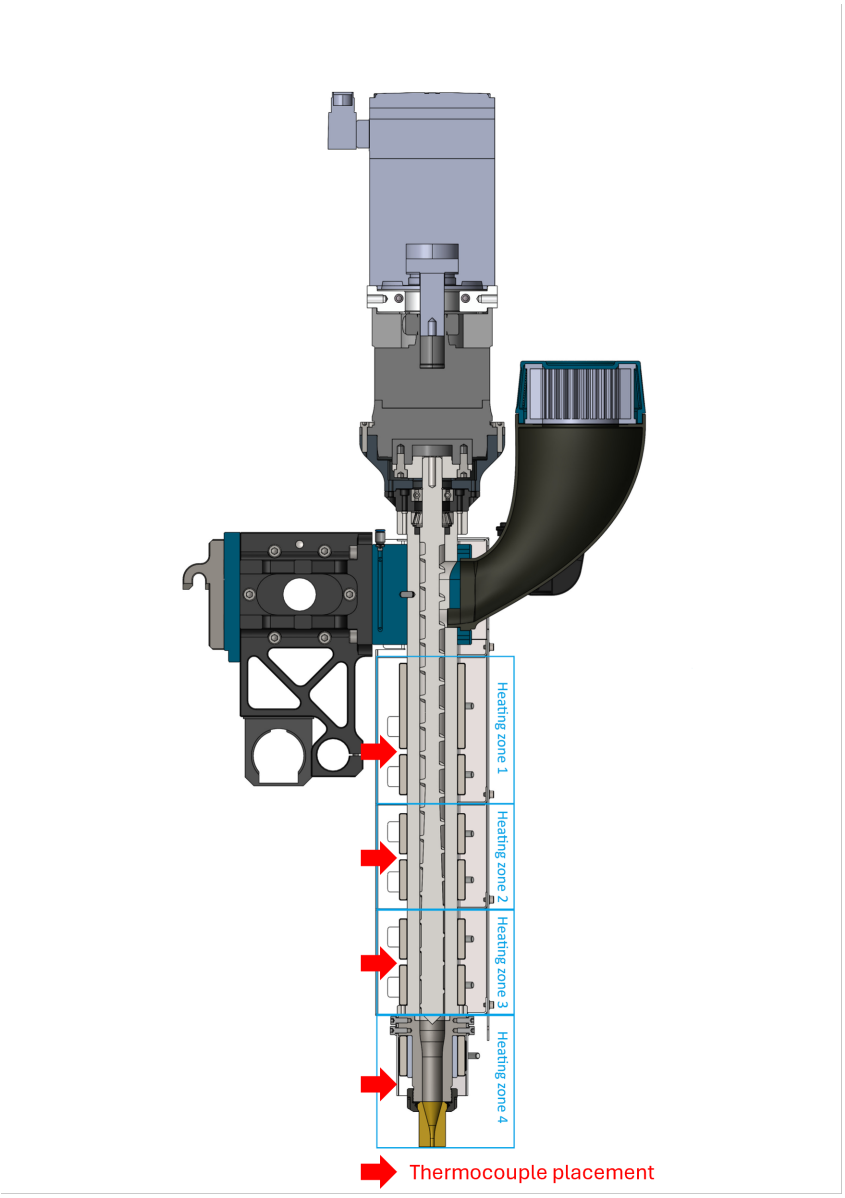

Figure 3.5: Cross section extruder with heating zones labelled.

3.2. Characterisation methods

This section explains all the characterisation methods for analysing the microstructure, specifically the voids and other material properties characterisation methods needed to analyse the printing process.

3.2.1. Microscopy

The microscope used is the VHX700N Digital Microscope at the TU Delft, shown in figure 3.6. Microscopy makes it possible to analyse the microstructure and void content. There are typically three types of lighting on a microscope. The first one is transmitted illumination, where the light travels through the sample, which is only possible for transparent materials. The second and third are known as reflected illuminations. Which can be divided into coaxial illumination, where ”the lighting travels along the same direction as the lens’s optical path and is used to view flat surfaces.”[11] and Ring illumination where the light reflects on an angled surface, which typically works better if the sample is textured or has an irregular surface. All three lightings are shown in figures 3.7, 3.8 and 3.9, where A is the microscopic lens, B is the glass plate, C is the sample, and D is the light source.

Figure 3.6: VHX700N Digital Microscope.

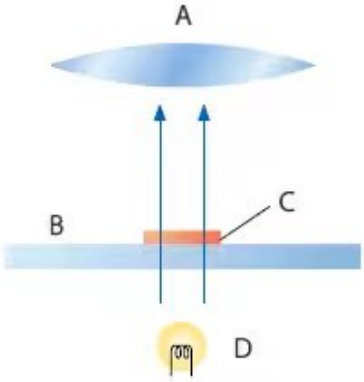

Figure 3.7: Lateral illumination visualisation [11].

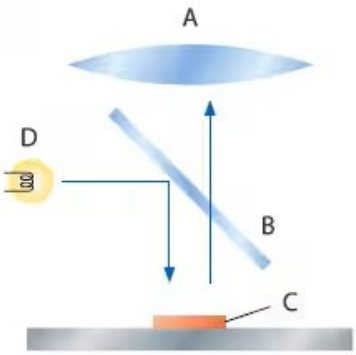

Figure 3.8: Coaxial illumination visualisation [11].

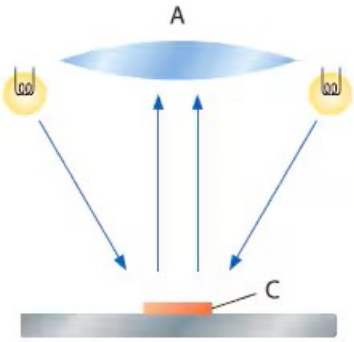

Figure 3.9: Ring illumination visualisation [11].

Lateral illumination does not result in usable images, as the samples are not fully transparent, so this method has not been used to characterise the microstructure. Coaxial illumination shows great contrasts between flat surfaces and irregular surfaces. As the irregular surface scatters, the light results in darker spots in the pictures. This is an excellent tool for looking at voids, as these are irregularities in the otherwise flat surface created by grinding and polishing. Ring-illuminated pictures are also taken to have an alternative view of the microstructure, giving more insight into the understanding of the microstructure. Figure 3.10 shows a microscopic picture with 500 times magnification of a coaxial and figure 3.11 for ring illumination. A step-by-step guide on how to generate the same microscopic pictures and void content measurements is given in appendix C.

To measure the void content, a program is used that measures the area of the voids and compares it to the total selected area, resulting in a void content percentage as shown in figure 3.6. This is done by using the pixel intensity threshold by brightness. ”However, despite the good results that can be achieved, this method can be very sensitive to the illumination conditions during the acquisition of the images and the type of material being analysed” [14]. Therefore, sample preparation plays an important role, as proper grinding and polishing influence the flatness of the surface, which creates a big contrast between fibres, voids and polymer when coaxial illumination is used.

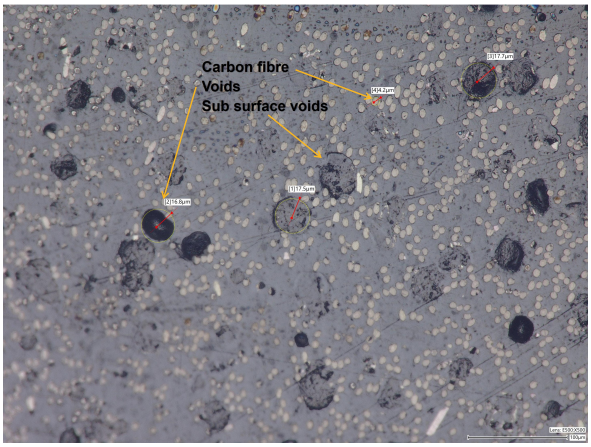

Figure 3.10: Coaxial illuminated microscopic picture taken at x500 magnification of a PPS sample.

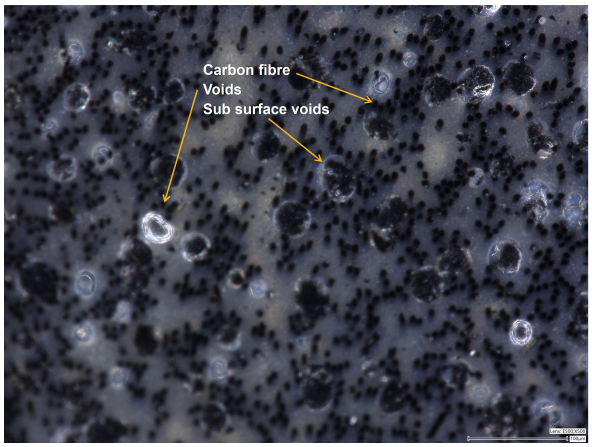

Figure 3.11: Ring illuminated microscopic picture taken at x500 magnification of a PPS sample.

Furthermore, threshold parameters are manually selected, thus giving a bit of uncertainty to the measured void content, which should be considered when analysing the void content results. However, when comparing similar samples with similar settings, results gives valuable insides in an increase or reduction of void content.

Sample preparation involves grinding and polishing to create an even and smooth surface. For each test, one sample is prepared in two directions: perpendicular and parallel to the printing direction, which cross-sections are visually shown in figure 3.12. As only one sample is prepared per test, it is essential to try to work as consistently as possible and consider the possibility of interpreting outliers as standard data. For each side, six different positions are measured at a magnification of x100 to ensure the whole sample's averages are taken. Also, areas smaller than 100 μm^2 are excluded from the measurement to eliminate any selection due to imperfections from grinding and polishing, such as minor scratches or small areas around the fibres, which are probably created due to small parts of the fibre breaking during the grinding step. The reason this is a valid step is that when a sample is very well ground and polished, these areas are then not visible, as shown in figure 3.10.

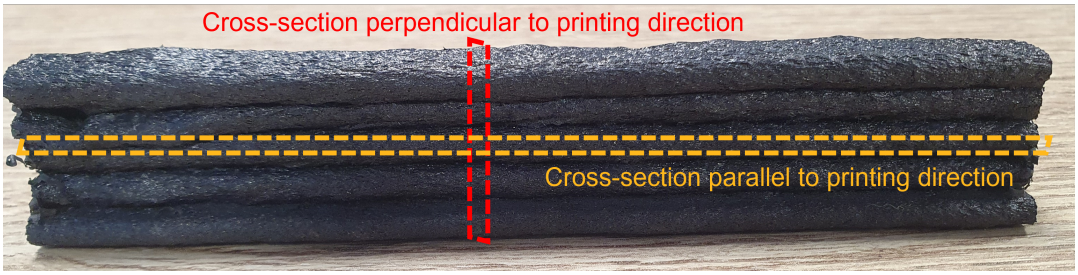

Figure 3.12: Bead cross-section visualisation.

3.2.2. Differential Scanning Calorimetry (DSC)

The Differential Scanning Calorimetry (DSC) used is the PerkinElmer Diamond DSC machine at the TU delft. Differential Scanning Calorimetry (DSC) is a thermal analysis technique. "It determines quantitatively the amount of heat absorbed or evolved by a sample compared to a reference during a specific thermal transition" [15]. To understand the data, one needs to know the thermodynamics behind the phase transitions. In thermal dynamics, there are first and second-order thermodynamic quantities. First-order thermodynamic quantities are given by equation 3.1 [15] and can be expressed as the first derivative of Gibbs free energy (G). Second-order thermal quantities are second derivations of free energy, such as the as given by equation 3.2 [15].

$$\left(\frac{\partial G}{\partial T}\right)_p = -S$$
$$\left(\frac{\partial G}{\partial T}\right)_T = V \tag{3.1}$$
$$\left(\frac{\partial \frac{G}{T}}{\partial \frac{1}{T}}\right)_p = H$$

$$\frac{\partial}{T}\left[\frac{\partial G}{\partial T}\right]_P = \left(\frac{\partial H}{\partial T}\right) T = C_p \tag{3.2}$$

First-order transitions are transitions in which the free energy is continuous as a function of a given variable, such as volume, pressure, and temperature. However, the first-order derivatives are discontinuous or step-like. Second-order transitions are transitions that have a change in slope with first-order quantities.

DSC measurements are performed based on the energy absorption over temperature. Thus, discontinuity is visible at second-order transitions like the glass transition temperature as shown in figure 3.13. Continuous peaks are observed for first-order transitions like melting and crystallisation as shown in figure 3.14.

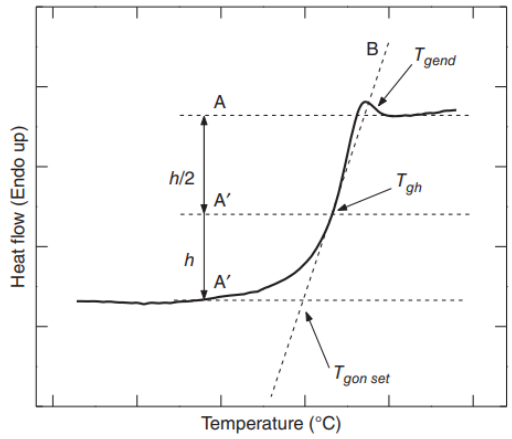

Figure 3.13: Graph of glass transition visualisation [15].

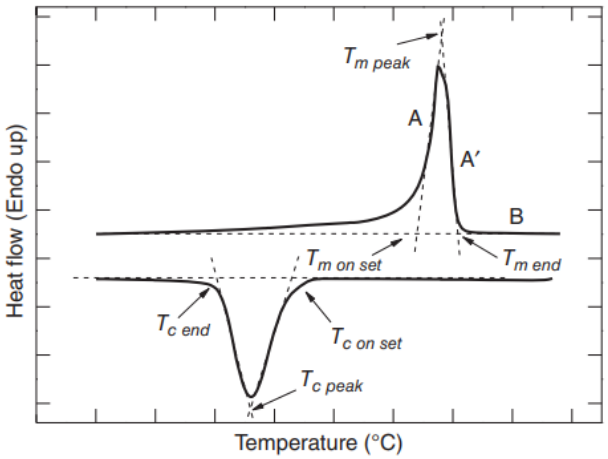

Figure 3.14: Graph of Melting and crystallisation visualisation [15].

Thermal transitions such as glass transition, melting, and crystallisation do not occur at a specific point but over a range of temperatures. There is an onset temperature at which the transition starts a peak, which is usually the value given to the thermal transition, and a temperature at which the transition is done.

3.2.3. Micro Compute Tomography (Micro-CT)

The Micro-computed tomography (Micro-CT) used is the ZEISS Xradia context micro-CT at the TU delft. It works on the principle of using X-ray with a cone-beam geometry as the source and a rotational sample holder as shown in figure 3.15.

The X-rays pass through the sample, and some of the X-rays are absorbed depending on the linear attenuation coefficient (LAC) denoted by μ_c. "The LAC depends on the density and an atomic number of the material and the applied X-ray energy" [25]. The X-ray detection plate captures the difference in intensity of the X-rays passing through the sample as shown in figure 3.16. The relationship between the difference in intensity and the LAC is described by the Lambert-Beer equation as shown in equation 3.3 [25].

$$I = I_0 * e^{-\mu_c * x} \tag{3.3}$$

"Where I is the transmitted intensity, I_0 is the incident X-ray intensity, μ_c is the Linear attenuation coefficient, and x is the thickness of the sample." [25].

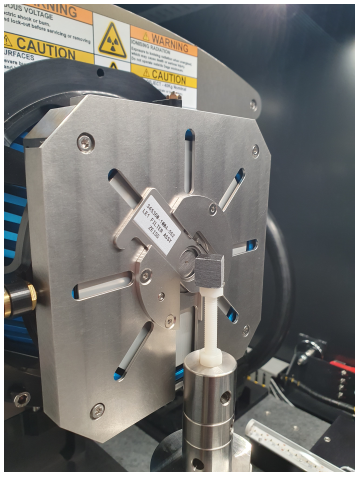

Figure 3.15: Micro-CT sample holder with the sample in front of the X-ray source.

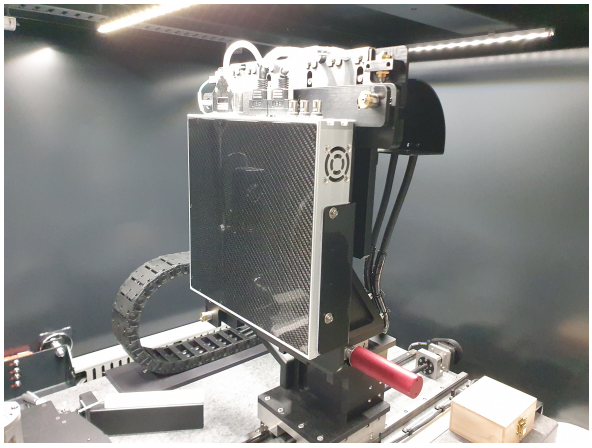

Figure 3.16: Micro-CT X-ray detection plate.

The difference in intensities of the x-ray measured generates a 2D image, as shown by figure 3.17. By rotating the image, multiple 2D images are generated at different angles. By processing these images a 3D images is generated. The benefit of this method is that it gives the possibility to look inside the sample without destroying it compared to having to cut the sample open as with microscopy.

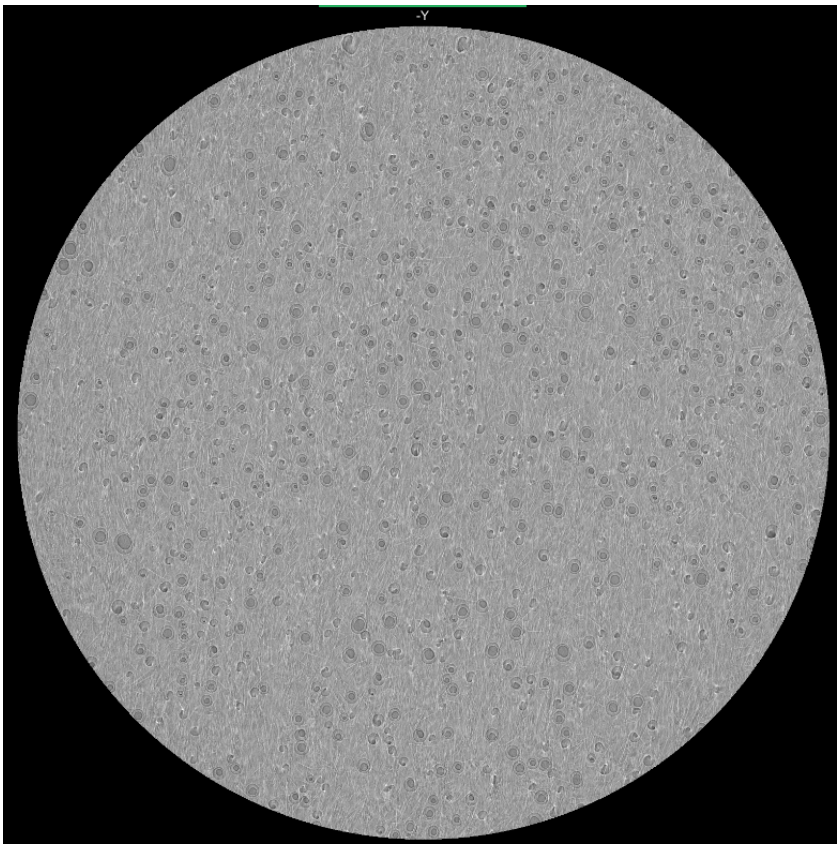

Figure 3.17: Micro-CT measurement layer 150.

3.3. Materials

This section explains the materials based on data-sheets provided by suppliers and additional information gathered from books like the Handbook of Polymers by Van der Vegt and Govaert [24] and the molecular structures of the monomers are given so the reader can better understand the different materials.

3.3.1. Polyphenylene sulphide (PPS)

The grade of Polyphenylene sulphide (PPS) made by Witcom, is PPS-2023/240 with 50% Post-industrial recyclate (PIR), which means 50% is recycled material which ”is separated from the waste stream during a manufacturing process” [9]. In this case, the waste stream is from the aviation industry. What is known about PPS is its high crystallinity, which generally has a melting point of around 280 to 290 degrees Celsius. It has good mechanical properties and high thermal resistance. Figure 3.18 shows the monomer molecular structure.

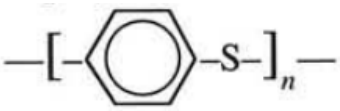

Figure 3.18: Molecular structure PPS repeating unit [24].

PPS has an aromatic ring, which results in a higher overall strength of the polymer chain due to the resonance-stabilisation effect as explained in section 2.1.1.

3.3.1.1. DSC measurement

This grade of PPS is relatively new; there is little information in the data sheet provided, which is given in Appendix A.1. Attempts were made to perform the DSC measurement, which resulted in unclear results; therefore, contact was made with Witcom, which performed a successful DSC measurement shown in figure 3.19. With which it is able to validate the melting point and crystallisation point.

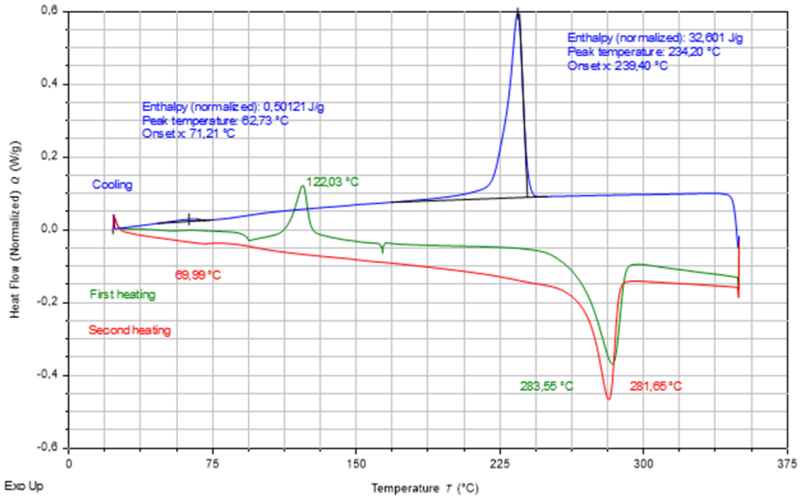

Figure 3.19: Differential Scanning calorimetry measurement of the Witcom PPS grade.
Side-note: The x-axis is in steps of 18.75 Degrees Celsius.

The DSC measurement in figure 3.19 shows two heating cycles, where the first heating cycle, compared to the second, has a peak visible at 122 degrees Celsius, indicating a cold crystallisation appearing due to its heat history. Cold crystallisation occurs When the polymer is gradually heated above the glass transition temperature, and the polymer chains gain enough mobility to reorientate and form crystal structures. This only happens when the previous heating history results in a fully or partially

amorphous structure. Amorphous structures are created due to the material being quickly cooled from a molten state, also known as quenching.

In both the first and second cycle, a peak is observed, which starts at around 240 degrees Celsius and is also known as the onset temperature point of melting. The peaks have a maximum between 280 and 285 degrees Celsius, indicating the temperature at which the most energy is absorbed and, thus, the highest melting rate. Both peaks end around a temperature of 290 degrees Celsius, indicating the melting transition is finished.

The blue cooling curve shows a peak starting at 239 degrees Celsius, indicating the onset temperature for the crystallisation transition. The peak is maximum at around 234 degrees Celsius, indicating the highest crystallisation rate, and ends at around 185 degrees Celsius. Between the onset and end, the bulk of crystallisation takes place.

3.3.1.2. Microscopy measurement

Microscopic void content measurements are performed on the granulate and for PPS the average void content is 14.3% and a standard deviation of 5.5%. Figure 3.20 shows a microscopic picture at x20 magnification of a couple of granulates under ring illumination.

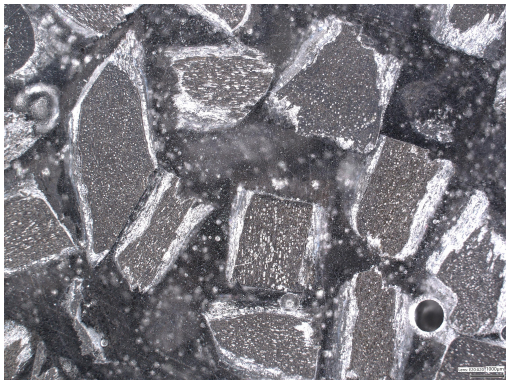

Figure 3.20: Ring illuminated microscopic picture taken at x20 magnification of a couple of PPS granulates.

The granulate has a cylindrical shape; however, its shape and size are inconsistent. The void content is relatively high with quite some variation between each granulate. This inconsistency in shape and void content tells us something about the consistency of the granulate production process. It is likely also influenced due to the use of 50% post-industrial recyclate.

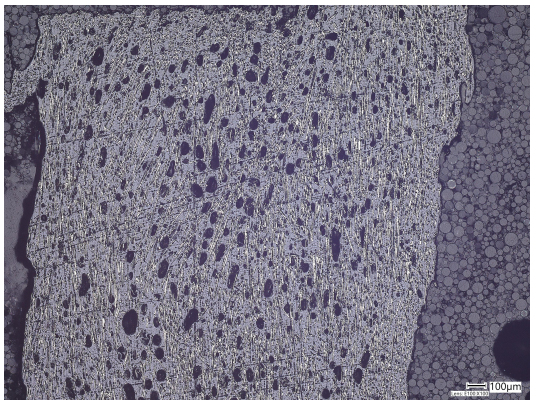

Figure 3.21: Coaxial illuminated microscopic picture taken at x100 magnification of PPS granulate at position 2.

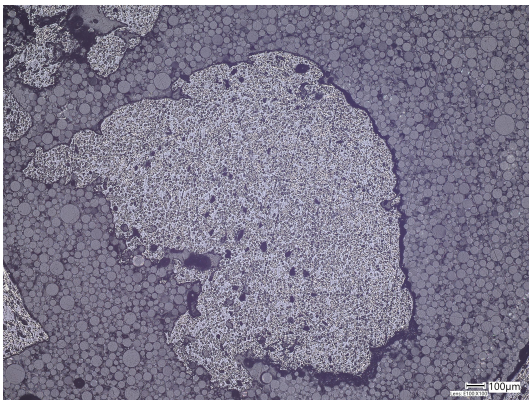

Figure 3.22: Coaxial illuminated microscopic picture taken at x100 magnification of PPS granulate at position 3.

3.3.2. Polyether sulphone (PESU)

The grade of polyether sulphone, also known as PESU or PES, is the Electrafil PESU 1810 3DP. An interesting fact is that the carbon fibre content is not given; however, under the microscope, the number of fibres visible is similar to those of PPS. Thus, an estimation could be made that fibre content is somewhere around 30%. What is generally known about PESU is that it has an amorphous structure and good thermal and mechanical properties. The molecular structure of the monomer is given in figure 3.23.

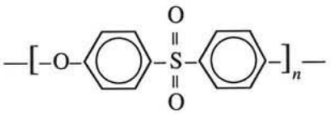

Figure 3.23: Molecular structure PESU repeating unit [24].

PESU has two aromatic rings, which results in a higher overall strength of the polymer chain due to the resonance-stabilisation effect as explained in section 2.1.1, an ether component given by the oxygen component connected to two other components introducing a more flexible part in the polymer chain and lastly a sulphone component is presently shown as the sulphide with two double-bonded oxygen atoms which presents a more rigid part in the polymer chain.

3.3.2.1. Microscopy measurement

Microscopic void content measurements are performed on PESU granulate, and the average void content is 5.4% and a standard deviation of 3.0%. In figure 3.24, a microscopic picture at x20 magnification of a couple of granulates under ring illumination is shown. The granulate has a cylindrical shape and a relatively low void content.

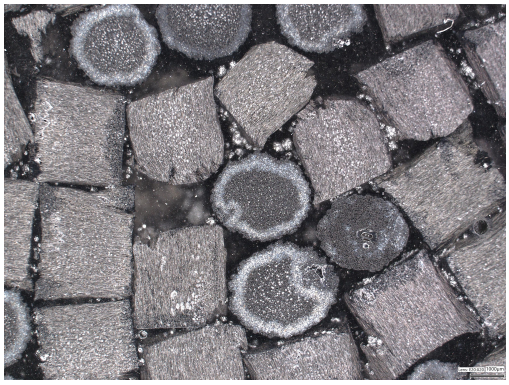

Figure 3.24: Ring illuminated microscopic picture taken at x20 magnification of a couple of PESU granulates.

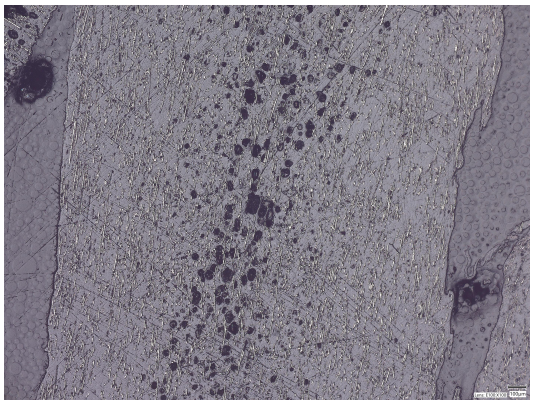

Figure 3.25: Coaxial illuminated microscopic picture taken at x100 magnification of PESU granulate at position 4.

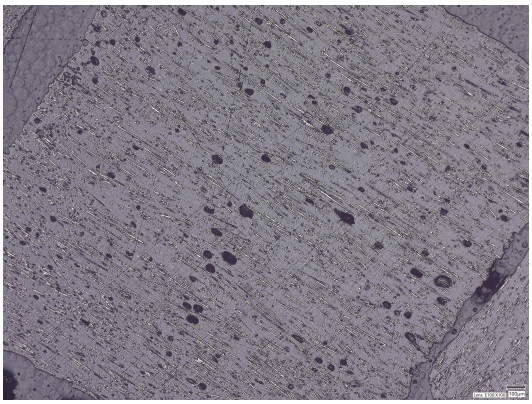

Figure 3.26: Coaxial illuminated microscopic picture taken at x100 magnification of PESU granulate at position 6.

3.3.3. Polycarbonate (PC)

The grade of polycarbonate, also known as PC, is Airtech - Dahltram C-250CF, with 20 % carbon fibre content. Polycarbonate generally has a glass transition temperature of around 140 degrees Celsius and is, therefore, not considered a high-temperature polymer but an engineering polymer. It is known for its good mechanical properties, especially its impact resistance. The molecular structure of the monomer is given in figure 3.27.

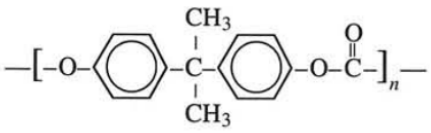

Figure 3.27: Molecular structure PC repeating unit [24].

3.3.3.1. Microscopy measurement

Microscopic void content measurements are performed on the granulate, and for PC, the average void content is 5.5% and a standard deviation of 2.5%. Figure 3.24 shows a microscopic picture at x20 magnification of a couple of granulates under ring illumination. The granulate has a cylindrical shape and a relatively low void content.

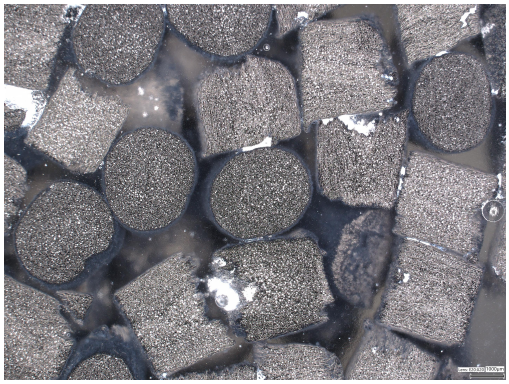

Figure 3.28: Ring illuminated microscopic picture taken at x20 magnification of a couple of PC granulates.

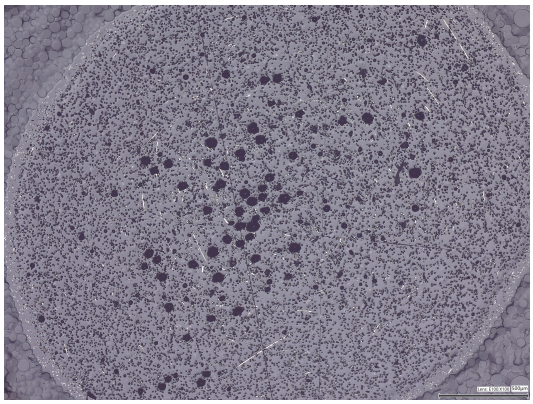

Figure 3.29: Coaxial illuminated microscopic picture taken at x100 magnification of PC granulate at position 1.

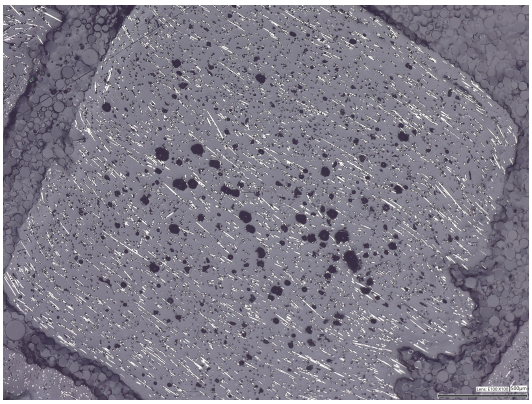

Figure 3.30: Coaxial illuminated microscopic picture taken at x100 magnification of PC granulate at position 2.

4

Analysing variation

Before any tests can be performed, understanding the variation of void content due to the system and characterisation methods is needed. Therefore, this chapter explains the variation in void content by testing the system to gain insight into the variation of the system, which gives an understanding of what kind of variation can be expected within a sample, known as part variation and the difference between different printed samples with the same printing parameters known as part-to-part variation. Lastly, it looks at the differences in void content between the characterisation techniques of microscopy and micro-CT.

4.1. Variation test

The variation tests are performed to see if there is or is not a significant difference between the datasets representing different samples from the same print sample in the section of 4.1.1, also known as part variation and between different print samples with the same input settings in section 4.1.2 also known as part-to-part variation.

As for each variation test, three samples are used to generate three corresponding datasets; therefore, an analysis of variance (ANOVA) is used to analyse if there is statistically a significant difference, as described in the book by Buijs [2]. ANOVA is a one-sided test, which is suitable in this case as we want to investigate if there is a difference and do not look if this difference is positive or negative. To perform the ANOVA, a null hypothesis needs to be determined. In this case, the null hypothesis is ”There is no significant difference between the averages of the datasets”. The alternative hypothesis is ”There is a significant difference between the averages of the datasets”.

Whether the null hypothesis is accepted or rejected depends on if the calculated F-value is higher or lower than the critical F-value. When it is higher, the null hypothesis is rejected; when it is lower, it is accepted. The F-value is calculated by equation 4.1 [2], which looks at the ratio of variation between the dataset to the variation of the values within the datasets.

$$F = \frac{\frac{SS_B}{df_B}}{\frac{SS_W}{df_W}} \tag{4.1}$$

These variations are calculated by dividing the sum of squares within the data group SS_w and between data groups SS_b by their respective degrees of freedom df_w and df_b as calculated by equations 4.2 [2].

$$
\begin{aligned}
SS_W &= \sum_{j=1}^{N_{data}} \sum_{i=1}^{n_j} (x_{ij} - x_{.j})^2 \\
SS_B &= \sum_{j=1}^{N_{data}} \sum_{i=1}^{n_j} (x_{.j} - x_{..})^2 = \sum_{j=1}^{N_{data}} n_j (x_{.j} - x_{..})^2 \\
df_w &= N_{data} - 1 \\
df_B &= \sum_{j=1}^{N_{data}} (n_j - 1)
\end{aligned}
\tag{4.2}
$$

With N_{data} the number of datasets or the number of tests performed, $x_{..}$ the mean value of the whole matrix or mean value of all tests, $x_{.j}$ mean value of column j or the mean value of each test, x_{ij} value in the matrix at the ij-th position or the i-th position of the j-th test, n_j number of positions in the column j or test j. With all the sum of squares and degrees of freedom.

The critical F-value is determined using F-tables as given in appendix B, with a significance of 0.05. This means there is an acceptance of a 5% chance the null hypothesis is rejected when it should not have been rejected, which is a standard in statistics. Using the table and the degrees of freedom calculated by equations 4.2 gives the critical F-value.

It is important to state that only one print test is performed for each measurement apart from the variation tests. As a result, the data provides insight but cannot be considered statistically robust, as variation and outliers can influence the results. However, the variation test does give some insight into the magnitude of variation that can be expected when looking at the results. In the last variation test in section 4.1.3, variation between characterisation methods, namely microscopy and micro-CT, is tested.

4.1.1. Part variation test

The Part variation test is performed on the PESU grade described in section 3.3.2, table 4.1 contains the input settings for the print test. Where the input settings are based on previous testing knowledge, data-sheets and test results from chapter 6. For the part variation test, the average void content, the standard deviation of the void content, average screw speed, average screw torque, and average nozzle pressure are measured, and results are shown in table 4.2. It also contains the overall average void content and standard deviation when the different tests are considered one dataset. This determines what variation can be expected for the void content results.

Input parameters	Units	**Test 2**
Material number	[-]	1950
Nozzle diameter	$[mm]$	4
Bead dimensions (WxH)	$[mm]$	6x2
Printing speed	$[mm/s]$	50
Temp. Hz 1	$[^{\circ}C]$	360
Temp. Hz 2	$[^{\circ}C]$	370
Temp. Hz 3	$[^{\circ}C]$	380
Temp. Hz 4	$[^{\circ}C]$	390

Table 4.1: Printing parameters input settings part variation test.

The part variation test where three samples are taken from printing test two results are shown in table 4.2, where the overall average (Avg) and standard deviation (Std) of the void content is considering gathered from considering all data one dataset.

Test [–]	Avg void [%]	Std void [%]
2.1	7.1	2.0
2.2	8.4	1.7
2.3	6.5	1.1
overall	7.3	1.8

Table 4.2: Results void content measurements on part variation tests.

The measured averages are around the value of 7.3% with a deviation of 1.8%. To know if there is or isn't a significant difference between the averages of the samples, an ANOVA is performed as following the explanation in section 4.1. This result is in the ANOVA table shown in table 4.3.

Variation source [–]	degree of freedom df [–]	Sum of squares SS [$\%^2$]	Mean square MS [$\%^2$]	F-value [–]
Between groups (B)	3 - 1	11.6	5.8	1.8
Within groups (W)	18 - 3	48.7	3.2	
Total (T)	18 - 1	60.3		

Table 4.3: ANOVA table for part variation test.

With the degrees of freedom from table 4.3, the critical F-value is 4.77. Therefore, the calculated F-value is lower than the critical F-value, meaning the null hypothesis can be accepted. Thus, there is no significant difference between the parts test. Therefore, the difference within the sample can be explained by randomness.

4.1.2. Part to Part variation test

The Part-to-part variation test is performed on PESU grade described in section 3.3.2, table 4.4 contains the input settings for the print testing. Where the input settings are based on previous testing knowledge, data sheets and test results from chapter 6. The average void content and standard deviation results are shown in table 4.5 together with the overall average void content and standard deviation of when the different tests are considered one dataset. This gives inside in what kind of variation in void content can be expected and considered when looking at further results, due to part to part variation.

Input parameters	Units	Test 1	Test 2	Test 3
Material number	[-]	1950	1950	1950
Nozzle diameter	$[mm]$	4	4	4
Bead dimensions (WxH)	$[mm]$	6x2	6x2	6x2
Printing speed	$[mm/s]$	50	50	50
Temp. Hz 1	$[^\circ C]$	360	360	360
Temp. Hz 2	$[^\circ C]$	370	370	370
Temp. Hz 3	$[^\circ C]$	380	380	380
Temp. Hz 4	$[^\circ C]$	390	390	390

Table 4.4: Printing parameters input settings part-to-part variation test.

From each printing test dataset, the average and standard deviation are calculated. Furthermore, the overall average and standard deviation are calculated by considering the three different datasets as one big dataset. Table 4.5 shows the data for the variation between different printing tests.

Test [−]	Avg void [%]	Std void [%]	Avg screw speed [rpm]	Avg screw torque [Nm]	Avg nozzle pressure [Bar]
1	6.4	0.5	17.4	41.5	23.5
2	7.1	2.0	17.4	40.6	23.3
3	9.4	1.0	17.4	43.4	23.7
overall	7.6	1.9	17.4	41.8	23.5

Table 4.5: Results void content measurements on part-to-part variation tests

So, the measured averages are around the value of 7.6% with a deviation of 1.9%. Also, for this test, an ANOVA is performed with the results in table 4.6.

Variation source [−]	degree of freedom df [−]	Sum of squares SS [%^{2}]	Mean square MS [%^{2}]	F-value [−]
Between groups (B)	3 - 1	30.8	15.4	6.03
Within groups (W)	18 - 3	38.3	2.6	
Total (T)	18 - 1	69.1		

Table 4.6: ANOVA table for part-to-part variation test.

As this test has the same degrees of freedom, the critical F-value is again 4.77, meaning this time, the calculated F-value is higher than the critical F-value. Therefore, the null hypothesis is rejected, meaning there is a significant difference between the part-to-part test results. As the tests are performed on the same day after each other, it is unlikely to be due to variations in ambient temperature and humidity. Therefore, it is likely due to the inconsistency of the extruder or to unknown phenomena occurring while performing the different tests. Inconsistencies of the extruder could be related to the older servo, as small fluctuations can also be detected in the average screw speed.

Since both part and part-to-part variation tests show similar overall averages and standard deviations, a deviation of approximately 2% should be kept in mind when analysing further test results to account for these variations

4.1.3. Variation microscopy to micro-CT void measurements

A PC grade described in section 3.3.3 is used to compare microscopy results to micro-CT. This is done to investigate the variation between a destructive and non-destructive void content measurement. To see if sample surface preparation potentially influences the void content measurements. The polycarbonate print is made on a flexbot, which does not use a material number, but with a general screw multiplier working on a percentage-based value. However, to determine this multiplier, the same steps of measuring the bead dimensions and changing the multiplier are used for the material number. Table 4.7 shows the printing test input settings. The results of average void content and standard deviation of the polycarbonate for both microscopy and micro-CT measurements are shown in table 4.8.

Input parameters	Units	Test 2
Nozzle diameter	[mm]	12
Bead dimensions (WxH)	[mm]	20x4
Temp. Hz 1	[$^\circ C$]	288
Temp. Hz 2	[$^\circ C$]	299
Temp. Hz 3	[$^\circ C$]	316
Temp. Hz 4	[$^\circ C$]	338

Table 4.7: Printing parameters input settings microscopy to micro-CT comparison test performed on PC.

A micro-CT and microscopy void measurement is performed on the same (PC) printing test sample. This gives valuable insight into the difference in characterisation techniques and their void content selection. The void content results of the microscopy and micro-CT void content determinations are shown in table 4.8.

Test [–]	**Cross-section** [–]	**Avg void** [%]	**std void** [%]
Microscopy	Parallel	8.3	1.0
Microscopy	Perpendicular	6.3	0.4
Micro-CT	3D	10.5	-

Table 4.8: Results void content measurements on variation Mico-CT and Microscopy test.

The microscopic and micro-CT results differ by about 2.5 % to 4 % in void content measurement results. A potential reason for the slightly higher void content in the micro-CT could be the micro-CT measuring across multiple beads. It also measures potential air entrapment between printed beads. With microscopy, positions are carefully taken to ensure measurements are only performed inside the bead, not at bead intersections. Another difference is the threshold selection shown in figures 4.1 and 4.2 for micro-CT and microscopy, respectively. It shows the difference in void selection due to the different programs used. It also shows the micro-CT has less contrast than the microscopy, making it harder to use the threshold method. The contrast could be increased by using a smaller sample and optimizing measuring parameters like the voltage of the x-ray source. This highlights that it is not the characterisation method that matters most but the sample preparation, correct measuring and void selection method.

Overall, the void contents are relatively close to each other, and the difference can be explained by the difference in the accuracy of the threshold selection and the inclusion of inter-bead surfaces in the micro-CT sample.

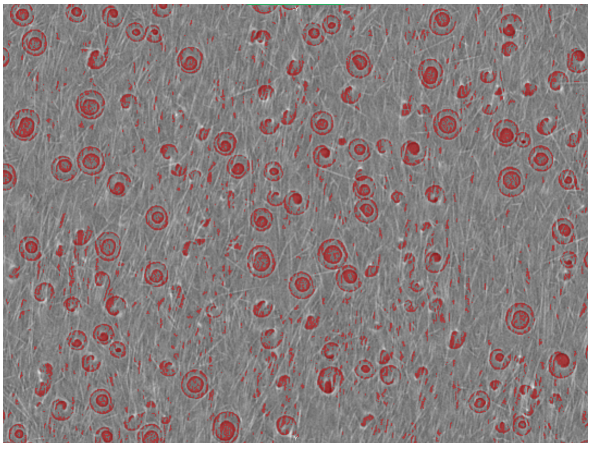

Figure 4.1: Micro-CT measurement of PC horizontal cross-section at layer 150.

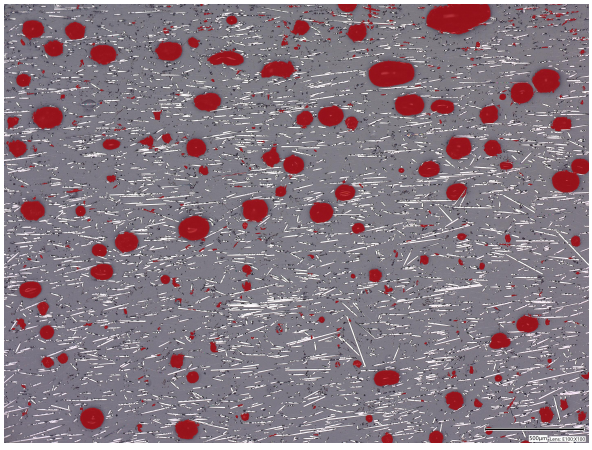

Figure 4.2: Microscopy measurement of PC horizontal cross-section at position 1.

5

Experiments

This chapter provides an overview, with each section explaining the purpose of the experiment, what the printing input settings are and how the tests are performed. The first section is about all the tests performed to understand the influence of printing parameters. The second section is about the influence of design changes.

5.1. Printing parameters

The printing parameters are the system's inputs. They are the material number, printing dimensions, volumetric output, and the temperatures of heating zones.

5.1.1. Material number

A certain volume of material is transported through the extruder per revolution of the screw turns. This volume is dependent on the geometry of the screw as explained in section 2.2.3; due to all tests being performed with the same screw geometry, this can be considered as a constant $C_{geometry}$ and multiplied with the actual screw speed η_{actual} results in the volumetric output. Another factor is the flow behaviour of the material through the channel, which is influenced by the viscosity of the material and the adhesion behaviour between the material to the screw and barrel. Therefore, a material number $M_{material}$ accounts for this material-specific difference. This material number is a multiplier for the base screw speed η_{base} to ensure the correct volumetric output is delivered according to the input bead dimensions and printing speed. Therefore, the volumetric output can be calculated by a simplified equation 5.1

$$\begin{aligned} Q_v &= C_{geometry} * \eta_{actual} \\ \eta_{actual} &= M_{material} * \eta_{base} \end{aligned} \tag{5.1}$$

Another way of calculating the volumetric output is to look at the bead dimensions W_{bead} and H_{Bead} of the printed bead and multiply these bead dimensions by the printing speed $V_{printing}$, which is the speed at which the extruder moves over the given tool path. The formula is given by equation 5.2.

$$Q_v = V_{printing} * W_{bead} * H_{Bead} \tag{5.2}$$

To investigate what the relationship is between actual screw speed and material number one PESU print is performed and changing the material number for each section containing ten layers according to input parameters table 5.1. This test is only performed on one material as the relationship between actual screw speed and the material number is programmed; therefore material independent. However, for both PESU and PPS a print is made changing the material number till the input bead dimensions correspond with the printed bead dimensions indicating the right material number is used for the correct volumetric output, which the results of will be discussed in the next chapter.

Input parameters	Units	1	2	3	4	5	6
Material number	[-]	**2400**	**1950**	**1500**	**1050**	**2850**	**3300**
Nozzle diameter	$[mm]$	4	4	4	4	4	4
Bead dimensions (WxH)	$[mm]$	6x2	6x2	6x2	6x2	6x2	6x2
Printing speed	$[mm/s]$	50	50	50	50	50	50
Temp. Hz 1	$[°C]$	288	288	288	288	288	288
Temp. Hz 2	$[°C]$	299	299	299	299	299	299
Temp. Hz 3	$[°C]$	316	316	316	316	316	316
Temp. Hz 4	$[°C]$	338	338	338	338	338	338

Table 5.1: Printing parameters input settings material number test.

5.1.2. Printing dimensions

The nozzle diameter and aspect ratio determine the printing dimensions. The aspect ratio is the ratio between the width and height of the bead. The width of the bead is generally chosen to be around 1,5 times the inner nozzle diameter. The aspect ratio has a vital influence on the aesthetics of the print and is calculated with equation 5.3. Different aspect ratios were tested for PESU, namely aspect ratios of 4, 3 and 2.4.

$$Aspect\ ratio = \frac{W_{bead}}{H_{Bead}} \tag{5.3}$$

It should be mentioned that the influence of aspect ratio is more obvious when looking at small nozzle sizes, which limit the range of the aspect ratio. With bigger nozzle sizes the range of the aspect ratio still resulting in ascetically good looking prints is also bigger. An example is the polycarbonate sample printed with a twelve millimetre diameter and print dimensions of 20x4, resulting in an aspect ratio of five.

Input parameters	Units	Aspect ratio 4	Aspect ratio 3	Aspect ratio 2.4
Material number	[-]	1950	1950	1950
Nozzle diameter	$[mm]$	4	4	4
Bead dimensions (WxH)	$[mm]$	**6x1.5**	**6x2**	**6x2.5**
Printing speed	$[mm/s]$	90	90	90
Temp. Hz 1	$[°C]$	360	360	360
Temp. Hz 2	$[°C]$	370	370	370
Temp. Hz 3	$[°C]$	380	380	380
Temp. Hz 4	$[°C]$	390	390	390

Table 5.2: Printing parameters input settings printing dimensions test.

5.1.3. Volumetric output

As explained in section 5.1.2, the volumetric output can be calculated using two equations, namely equation 5.1 and 5.2. However, it is unknown how the volumetric output influences the void content. This is important as it can influence the range of printing speeds that can be used and, together with the tool path, influence the previous layer temperature, possibly limiting application use. Therefore, a volumetric influence test is performed on PPS and PESU. By performing it both on PPS and PESU, the difference between semi-crystalline and amorphous polymers can be investigated.

The input settings are used to test the influence of volumetric output for PPS as shown in table 5.3, which shows constant input settings are used except for the printing speed. The heating zone temperatures

are based on the DSC measurement on PPS, where the melting peak ends at around 290 degrees Celsius, as given in figure 3.19. Therefore, the temperature of heating zone 1 is set at 290 degrees. The influence on the average torque, screw speed, nozzle pressure and void content is shown for different volumetric outputs in figures 6.7.

Input parameters	Units	**Test 1**	**Test 2**	**Test 3**	**Test 4**	**Test 5**	**Test 6**	**Test 7**	**Test 8**
Material number	[-]	1900	1900	1900	1900	1900	1900	1900	1900
Nozzle diameter	$[mm]$	4	4	4	4	4	4	4	4
Bead dim. (WxH)	$[mm]$	6x2	6x2	6x2	6x2	6x2	6x2	6x2	6x2
Printing speed	$[mm/s]$	**10**	**20**	**30**	**40**	**50**	**60**	**70**	**80**
Temp. Hz 1	$[°C]$	290	290	290	290	290	290	290	290
Temp. Hz 2	$[°C]$	300	300	300	300	300	300	300	300
Temp. Hz 3	$[°C]$	310	310	310	310	310	310	310	310
Temp. Hz 4	$[°C]$	320	320	320	320	320	320	320	320

Table 5.3: Printing parameters input settings volumetric output tests for PPS.

The input settings are used to test the influence of volumetric output for PPS as shown in table 5.4, which shows constant input settings are used except for the printing speed. The heating zones are based on the information given by the material supplier data-sheet as given in appendix A and information gained from previous testing on this material. The influence on the average torque, screw speed, nozzle pressure and void content is shown for different volumetric outputs in figures 6.7.

Input parameters	Units	**Test 1**	**Test 2**	**Test 3**	**Test 4**
Material number	[-]	1950	1950	1950	1950
Nozzle diameter	$[mm]$	4	4	4	4
Bead dimensions (WxH)	$[mm]$	6x2	6x2	6x2	6x2
Printing speed	$[mm/s]$	**10**	**30**	**50**	**70**
Temp. Hz 1	$[°C]$	360	360	360	360
Temp. Hz 2	$[°C]$	370	370	370	370
Temp. Hz 3	$[°C]$	380	380	380	380
Temp. Hz 4	$[°C]$	390	390	390	390

Table 5.4: Printing parameters input settings volumetric output tests for PESU.

5.1.4. Temperature heating zones

There are two reasons why PPS was tested for different temperature input settings for the heating zones. The first is due to the lack of information from the material supplier and to check if the heating zones deducted from DSC measurements are correct input for this PPS grade. The second is it is known that temperature influences the viscosity of polymer melts following the Arrhenius equation as explained in section 2.1.3 and shown in equation 2.6. The Arrhenius equation describes a decrease in viscosity with increasing temperature. However, the influence of a lower viscosity on the void content is unknown. Therefore, tests are performed over a range of temperature input settings as given in table 5.3. In each test, all heating zones are increased by 10 degrees Celsius.

Input parameters	Units	Test 1	Test 2	Test 3	Test 4	Test 5
Material number	[-]	1900	1900	1900	1900	1900
Nozzle diameter	$[mm]$	4	4	4	4	4
Bead dimensions (WxH)	$[mm]$	6x2	6x2	6x2	6x2	6x2
Printing speed	$[mm/s]$	50	50	50	50	50
Temp. Hz 1	$[°C]$	**290**	**300**	**310**	**320**	**330**
Temp. Hz 2	$[°C]$	**300**	**310**	**320**	**330**	**340**
Temp. Hz 3	$[°C]$	**310**	**320**	**330**	**340**	**350**
Temp. Hz 4	$[°C]$	**320**	**330**	**340**	**350**	**360**

Table 5.5: Printing parameters input settings heating zones temperature tests for PPS.

5.1.5. Nozzle pressure influence

From the volumetric test results as given in graphs 6.7, there seems to be some correlation between void content and nozzle pressure. For this test, the volumetric output Q and, thus, screw speed are kept constant by varying the printing speeds and bead dimensions by using different nozzle diameters. The bead dimensions are determined by multiplying the nozzle diameter by 1,5 for the bead height H_{Bead} and 0,5 for the bead width W_{Bead}. The printing speed is calculated using the bead's dimensions as shown by equation 5.2. The input values for equation 5.2 and the resulting printing speed for the different nozzle diameters are shown in table 5.7.

Input parameters	Units	Test 1	Test 2	Test 3
Material number	[-]	1950	1950	1950
Nozzle diameter	$[mm]$	**4**	**6**	**9**
Bead dimensions (WxH)	$[mm]$	6x2	9x3	13.5x4.5
Printing speed	$[mm/s]$	**50**	**22.2**	**9.9**
Volumetric output	$[mm^3/s]$	600	600	600
Temp. Hz 1	$[°C]$	360	360	360
Temp. Hz 2	$[°C]$	370	370	370
Temp. Hz 3	$[°C]$	380	380	380
Temp. Hz 4	$[°C]$	390	390	390

Table 5.6: Printing parameters input settings nozzle pressure influence test.

Nozzle Diameter $[mm]$	Bead Width $[mm]$	Bead Height $[mm]$	Volumetric Output $[mm^3/s]$	Printing Speed $[mm/s]$
4	6	2	600	50.0
6	9	3	600	22.2
9	13.5	4.5	600	9.9

Table 5.7: Overview of nozzle dimensions and printing speeds.

5.2. Design influence

To answer the second sub-research question, "Which aspect of extruder design influences the printability and the microstructure of high-temperature polymer composite prints, and how could they be improved to minimize void content?" problems observed during testing of section 5.1 are taken into account and are linked to potential design improvements and where possible the design improvements are tested.

5.2.1. Nozzle insulation

During testing with PPS, the problem of nozzle clogging was encountered, indicating a problem with heat loss in the nozzle, decreasing the temperature of the polymer below the crystallisation temperature seen in the blue cooling curve of the DSC measurement seen in figure 3.19. Therefore, a design change was tested by including insulation to the nozzle, as seen in figure 5.1 to reduce this heat loss. Printing test input settings are kept the same for the volumetric output tests and are shown in table 5.8. This is for comparison reasons and to see the influence on the printability by testing the volumetric output range. Only the range of volumetric output was shorted to the upper region due to problems with print bed adhesion. The ambient temperature was lower compared to the volumetric output tests. This problem was, in later testing, resolved by using printed adhesion plates.

Figure 5.1: Nozzle with insulation around it.

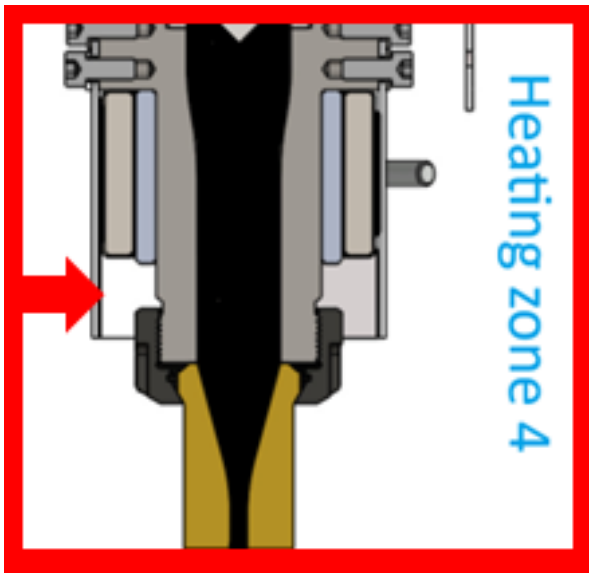

Figure 5.2: Extruder heat zone 4 sections with the red arrow indicating the thermocouple.

Input parameters	Units	Test 1	Test 2	Test 3	Test 4	Test 5
Material number	[-]	1900	1900	1900	1900	1900
Nozzle diameter	$[mm]$	4	4	4	4	4
Bead dimensions (WxH)	$[mm]$	6x2	6x2	6x2	6x2	6x2
Printing speed	$[mm/s]$	**50**	**60**	**70**	**80**	**90**
Temp. Hz 1	$[°C]$	290	290	290	290	290
Temp. Hz 2	$[°C]$	300	300	300	300	300
Temp. Hz 3	$[°C]$	310	310	310	310	310
Temp. Hz 4	$[°C]$	320	320	320	320	320

Table 5.8: Printing parameters input settings for insulation nozzle volumetric output tests for PPS.

Nozzle insulation testing is also performed on PESU to investigate the influence of temperature loss in the nozzle on the void content of amorphous polymers. Performing this test was influenced by the results of the PPS insulation tests shown in graphs 6.16. The PESU testing Tests with nozzle insulation are also performed on PESU to Validate that the problems arising are due to semi-crystallinity and investigate the nozzle cooling effect on amorphous polymers.

Input parameters	Units	**Test 1**	**Test 2**	**Test 3**	**Test 4**
Material number	[-]	1950	1950	1950	1950
Nozzle diameter	$[mm]$	4	4	4	4
Bead dimensions (WxH)	$[mm]$	6x2	6x2	6x2	6x2
Printing speed	$[mm/s]$	**10**	**30**	**50**	**70**
Temp. Hz 1	$[^{\circ}C]$	360	360	360	360
Temp. Hz 2	$[^{\circ}C]$	370	370	370	370
Temp. Hz 3	$[^{\circ}C]$	380	380	380	380
Temp. Hz 4	$[^{\circ}C]$	390	390	390	390

Table 5.9: Printing parameters input settings for insulation nozzle volumetric output tests for PESU.

6

Results and discussion

This chapter presents the results of the conducted tests, structured into two sections to answer the two research sub-questions. The first section is the influence of the printing parameter test. The second section contains the extruder design influence tests.

6.1. The influence of printing parameters

This section gives the testing results to answer the first sub-question of *"What is the influence of printing parameters on the printability and microstructure of high-temperature polymer prints?"*

6.1.1. Material number

The first printing input parameter tested is the material number, which is a multiplier for the screw speed compensating for flow behaviour differences due to differences in material. To make sure a certain volume of material is transported through the extruder per revolution of the screw turns.

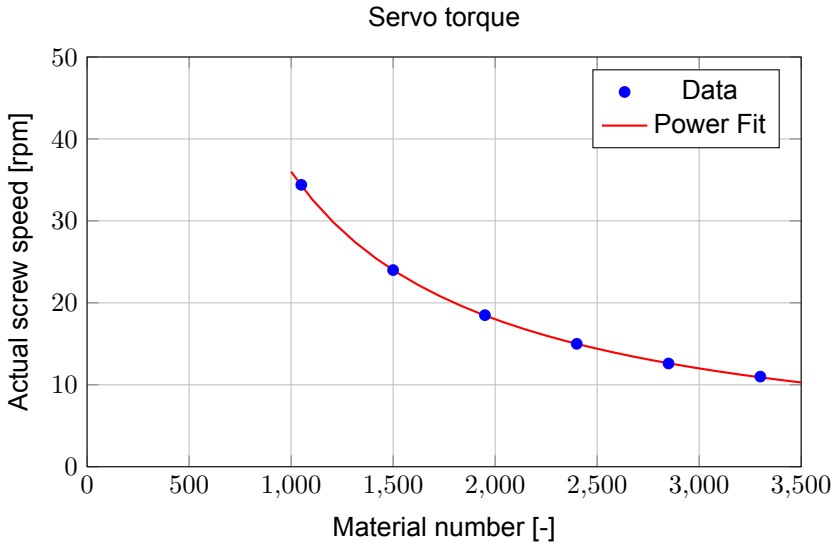

Figure 6.1: Results and trend line material number to actual screw speed test.

From trying different trend lines, it becomes apparent the relationship uses a power law trend line with the relationship given by 6.1 as the coefficient of determination of the power fit, also generally denoted as R^2 is 1, which means a perfect fit. However, it is more likely that the relationship is like 6.2 as the screw speed is programmed to have a relationship with the material number; therefore, whole numbers are more likely.

$$\eta_{actual} = 35789 \cdot M_{material}^{(-0.999)} \tag{6.1}$$

$$\eta_{actual} = \frac{36000}{M_{material}} \tag{6.2}$$

Figures 6.2 and 6.3 illustrate the difference between a bead produced with incorrect and correct material number. For PPS, a material number of 1900 and PESU, a material number of 1950, results in the correct volumetric output. These material numbers are determined by measuring the extruded bead height and width and changing them till they correspond to the input bead dimensions.

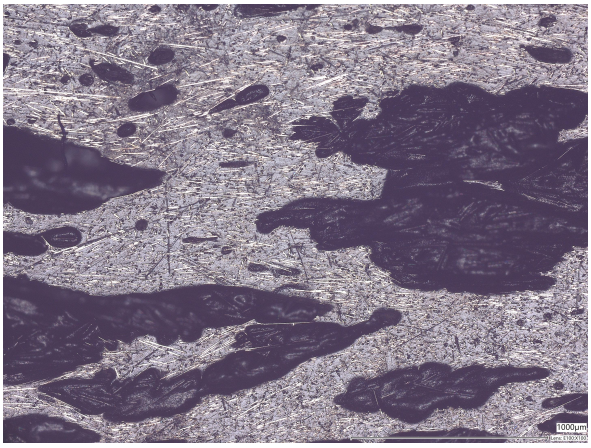

Figure 6.2: microscopic picture of PPS parallel cross-section with the wrong material number.

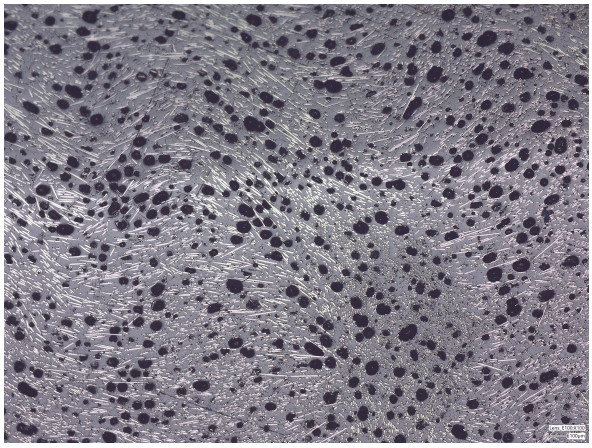

Figure 6.3: Microscopic picture of PPS parallel cross-section with the correct material number.

The microscopic pictures show a big difference in the void content and geometry of voids. The wrong material numbers create a high void content and very big voids, while the right material number results in small voids that are more spread over the sample with a lower void content, indicating that it is important to select the right material number. This difference is due to the wrong material number not having a high enough volumetric output, resulting in a pulling motion on the extruded bead, resulting in higher void content.

6.1.2. Printing dimensions

The input parameters of printing dimensions, namely the bead width and height, are tested by changing the aspect ratio. The test resulted in a most visually pleasing print at a ratio of 3, as can be seen in figures 6.4, 6.5, 6.6.

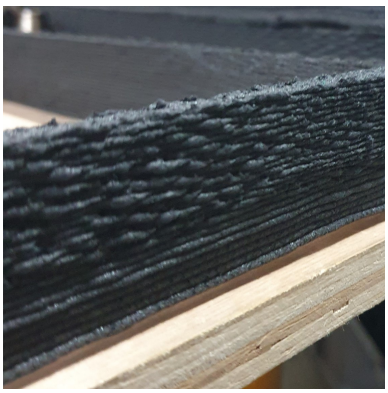

Figure 6.4: PESU print with aspect ratio 4.

Figure 6.5: PESU print with aspect ratio 3.

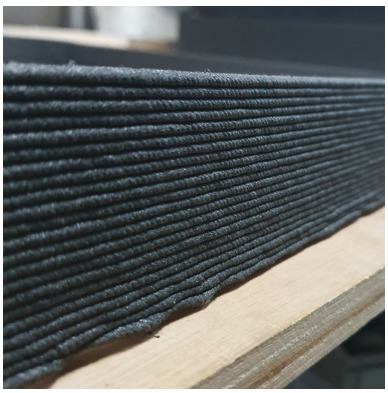

Figure 6.6: PESU print with aspect ratio 2.4.

An uneven surface in the printing direction is observed for an aspect ratio of 4, indicating output fluctuations caused by the extruded material pushing back against the nozzle and generating back pressure. When the back pressure rises, it forces out more material, reducing the back pressure and creating a repeating fluctuating pattern. However, this fluctuation in back pressure is not visible in the nozzle pressure measurements. This probably has to do with the speed at which these fluctuations occur and the nozzle's placement not being very close to the nozzle, meaning the sensor cannot measure these fluctuations.

A diagonal pattern is observed for an aspect ratio of 2.4, indicating that the extruded layer is not directly deposited onto the previous layer. This misalignment creates a pulling force on the extruded material due to gravity, decreasing back pressure and output. However, as the output decreases, back pressure builds up again, increasing volumetric output and causing fluctuations in the pattern. The pattern is diagonal because the increment height step is higher than the deposited layer, which pulls the material deposited closer to the previous layer. If the height between the nozzle and the previous bead is compared to the new printed material height, the effect becomes greater, and almost vertical lines can be observed.

6.1.3. Volumetric output

As explained in section 5.1.3, the volumetric output tests are performed on both PPS and PESU. The test results and results discussion are shown in sections 6.1.3.1 and 6.1.3.2, respectively.

6.1.3.1. Volumetric tests Polyphenylene sulphide (PPS)

This subsection presents the results and result discussion of the volumetric test performed on PPS. Where in figure 6.7, the averages of measured parameters like torque, screw speed, nozzle pressure and void contents in both parallel and perpendicular cross sections are plotted against the volumetric output.

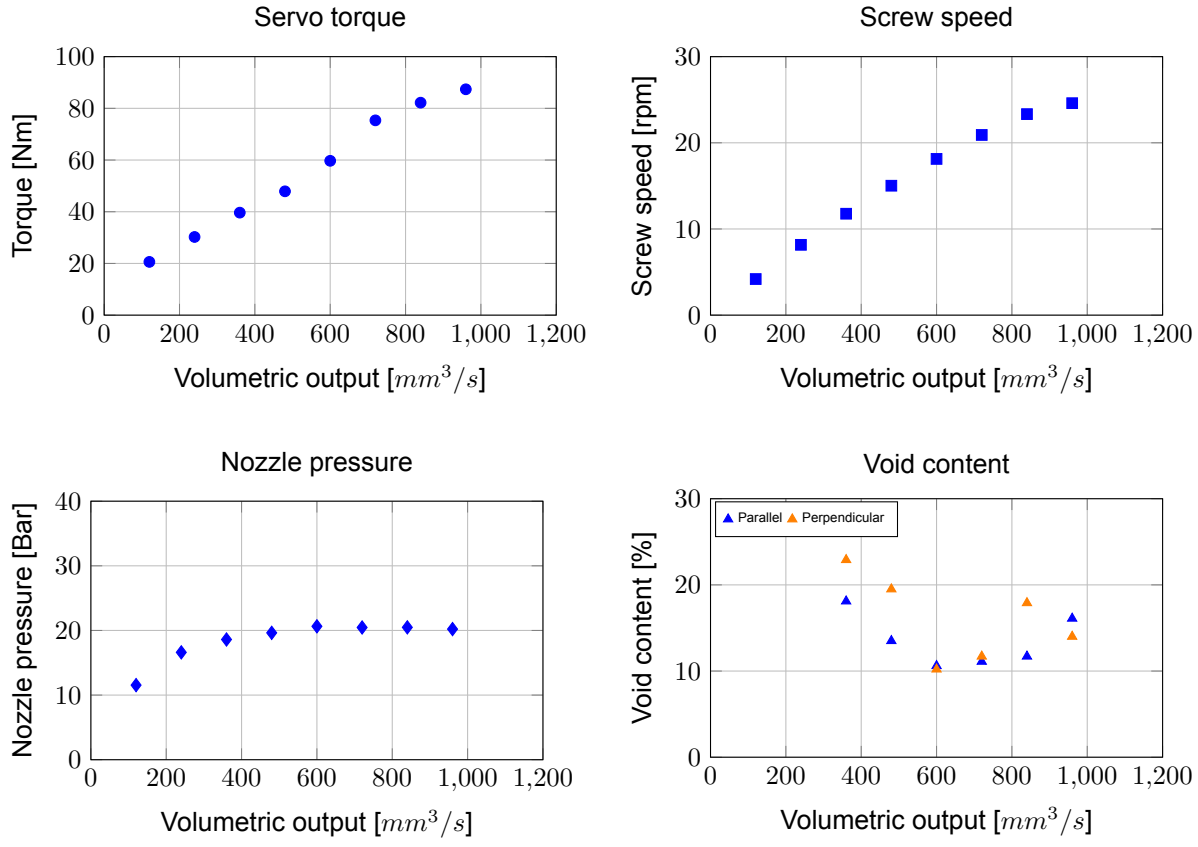

Figure 6.7: Result plots of averages of the measured parameters and void content versus the volumetric output for PPS.

The servo torque graph shows a relatively linear trend in the printing speed, indicating no major differences resulting from changing the volumetric output. However, the torque required is quite high and reaches its limit of 100 Nm at around a volumetric output of 1000 cubic millimetres per second. This can result in problems with higher volumetric outputs for bigger nozzle sizes of 6, 9, or 12 millimetres in diameter, limiting the printability range of PPS.

What is noticeable is the screw speed is not entirely linear to the printing speed, which is programmed to be linearly linked to the volumetric output; however, the box printer uses an older servo, which is known not to work ideally and seems to lose screw speed at higher volumetric outputs resulting in less volume being printed, than intended. This should be taken into account when looking at the void content results.

The nozzle pressure indicates the back pressure generated by the nozzle area. The viscosity, the geometry and the volumetric output influence this, as shown by the Hagen-Poiseuille equation 6.3. Considering the geometry constant as the same nozzle is used for each test and, therefore, the same geometry, a linear relationship would be expected at constant viscosity. However, viscosity is not constant as it is influenced by shear thinning behaviour and temperature. So, the nozzle pressure curve indicates viscosity becomes lower at higher volumetric outputs.

$$\Delta P = \frac{8 * \mu * L_p * Q_v}{\pi * R_n^4} \tag{6.3}$$

Table 6.1 presents the average void content and the standard deviation between the six different positions measured per cross-section of each sample. Additionally, it includes the average maximum void area and its standard deviation. Providing insight into the presence of large voids. Maximum values are used as they offer a more reliable metric, whereas averages can be affected by small voids, which potentially can also be imperfections in grinding and polishing. It also provides a better indication of whether there are macro voids present in the sample and also about the uniformity of the big voids distributed by looking at the standard deviation of the maximum area of the six locations. If the standard deviation is high, it indicates large voids are not evenly spread out over the sample, and when it is low, it indicates large voids are more homogeneous spread.

Volumetric output $[mm^3/s]$	**Cross-section** $[-]$	**Avg void** $[\%]$	**std void** $[\%]$	**Avg max area** $[*10^3\ \mu m^2]$	**Std max area** $[*10^3\ \mu m^2]$
360	Parallel	18.1	3.2	25.2	12.1
360	Perpendicular	22.9	3.7	22.0	19.6
480	Parallel	13.5	3.1	27.4	14.5
480	Perpendicular	19.5	2.0	8.4	1.7
600	Parallel	10.6	1.8	13.6	2.9
600	Perpendicular	10.2	0.9	6.4	1.0
720	Parallel	11.1	1.1	12.9	6.1
720	Perpendicular	11.7	0.9	8.5	2.8
840	Parallel	11.7	0.6	12.3	6.9
840	Perpendicular	17.9	1.6	7.9	2.4
960	Parallel	16.1	0.8	9.6	1.7
960	Perpendicular	14.0	2.4	5.7	1.1

Table 6.1: Void content volumetric output tests PPS.

The results from both the void content versus volumetric output graph and table 6.1 show a relatively high and more variating average void content for lower volumetric outputs researching a low at around a volumetric output of 600 mm^3/s interestingly also the volumetric output after which the nozzle pressure stays constant around 20 bar. This almost indicates a certain minimum pressure is needed in the nozzle in order to push voids out. Furthermore, the maximum void areas and standard deviations of the lower volumetric outputs are also higher, indicating there are bigger voids created and less homogeneous dispersed as can be shown in figures 6.8 and 6.9. The first is for a volumetric output of 360 mm^3/s, and the second is for a volumetric output of 960 mm^3/s.

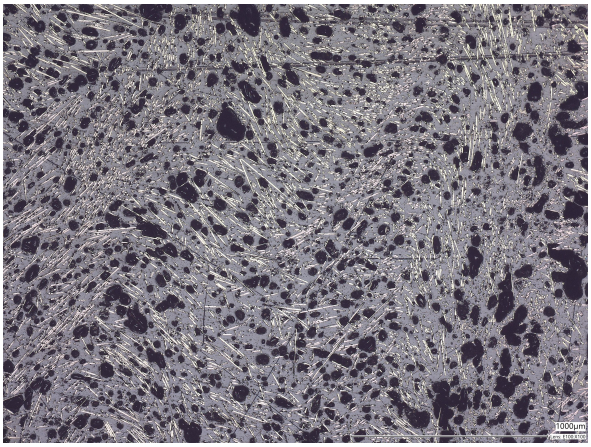

Figure 6.8: Microscopic picture of PPS parallel cross-section at x100 magnification of volumetric output 360 mm^3/s.

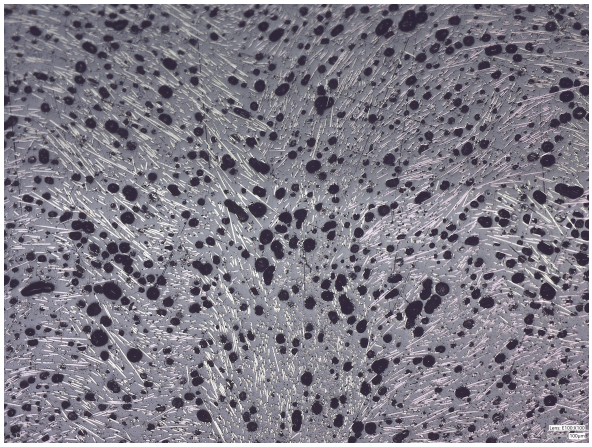

Figure 6.9: Microscopic picture of PPS parallel cross-section at x100 magnification of volumetric output 960 mm^3/s.

Comparing the lowest void content measured at volumetric output of 600 mm^3/s with 10.6% and standard deviation of 1.8% in the volumetric test with the granulate with measured a void content of 14.3% with a standard deviation of 5.5%. Indicating the extruder is able to eliminate the air in-between particles due to stacking and even able to eliminate some voids from inside the granulate.

The increase in void content at higher volumetric outputs, especially at around 960 mm^3/s, can be linked due to a decrease in screw speed, decreasing the actual volumetric output, which was seen in the material number tests to result in higher void content.

So, the results from the void content indicate that around a volumetric output of 600 mm^3/s results in the lowest void content. Furthermore, the nozzle pressure data indicates a non-Newtonian viscosity influence based on the volumetric output influences the nozzle pressure. However, it is difficult to say how much of this is due to the shear thinning effect or due to the difference in temperature of the polymer melt in the nozzle.

6.1.3.2. Volumetric tests PESU

This subsection presents the results and result discussion of the volumetric test performed on PESU. Where in figure 6.10, the averages of measured parameters like torque, screw speed, nozzle pressure and void contents in both parallel and perpendicular cross sections are plotted against the volumetric output.

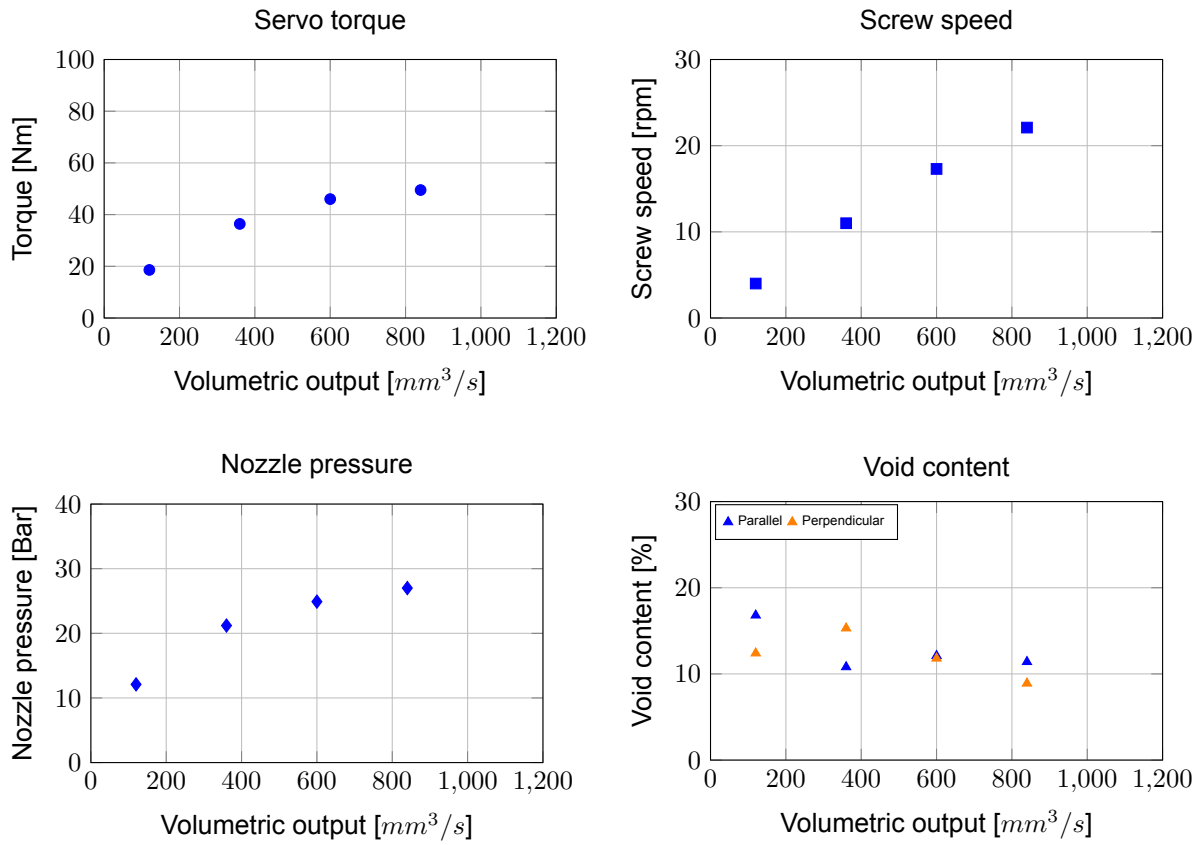

Figure 6.10: Result plots of averages of the measured parameters and void content versus the volumetric output for PESU.

The servo torque graph shows a linear trend at low volumetric outputs, which seems to flatten slightly at higher volumetric outputs. This could indicate the system needs less torque for higher screw speed due to the shear thinning effect, giving the polymer melt a lower viscosity. This statement should be considered with caution as the flattening is slight, and the system is complete. It is unknown if the flow of the molten polymer or the friction part governs the torque of the whole system. The screw speed graph is very similar to the one from PPS, which makes sense as material numbers are very similar in 1900 and 1950 for PESU and PPS, respectively.

The nozzle pressure graph shows a linear part at low volumetric output, after which it also starts to flatten, as also seen with PPS. However, the flattening is less extreme. Also, the nozzle pressures are generally higher than PPS, indicating that the viscosity of the PESU in the nozzle area is higher for these temperature settings. As following the rewritten Hagen-Poiseuille equation given by equation 6.3

Volumetric output $[mm^3/s]$	Cross-section $[-]$	Avg void $[\%]$	std void $[\%]$	Avg max area $[*10^3\ \mu m^2]$	Std max area $[*10^3\ \mu m^2]$
120	Parallel	16.8	2.1	72.5	20.6
120	Perpendicular	12.4	1.6	27.6	7.1
360	Parallel	10.8	1.5	63.1	25.0
360	Perpendicular	15.3	3.3	91.4	57.3
600	Parallel	12.1	2.7	116.5	106.4
600	Perpendicular	11.8	1.4	54.5	28.1
840	Parallel	11.4	5.3	139.8	203.2
840	Perpendicular	8.9	1.4	27.3	10.6

Table 6.2: Void content volumetric output tests PESU.

The results from both the void content versus volumetric output graph and table 6.2 show a slight decrease of the void content for higher volumetric outputs; however, less than with PPS. The average max void areas are also higher compared to the PPS tests, indicating bigger voids are created. Furthermore, the average void areas are also higher than that of PESU granulate, which has an average void content of 5.4% with a standard deviation of 3.0%. This indicates that the system is not working well enough to push all the air between granulate particles out of the system. It was observed that heating zone 1 also dropped during testing, even to a point where the printing stopped. This indicates that the system is not able to introduce enough heat into the system. This also introduces a big problem for the printability of PESU.

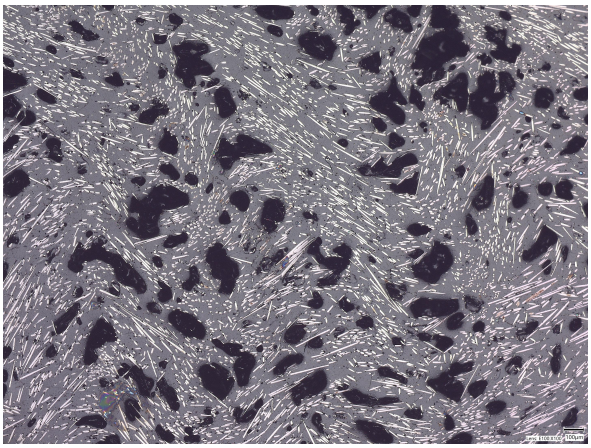

Figure 6.11: Microscopic picture of PESU parallel cross-section at x100 magnification of volumetric output 120 mm^3/s.

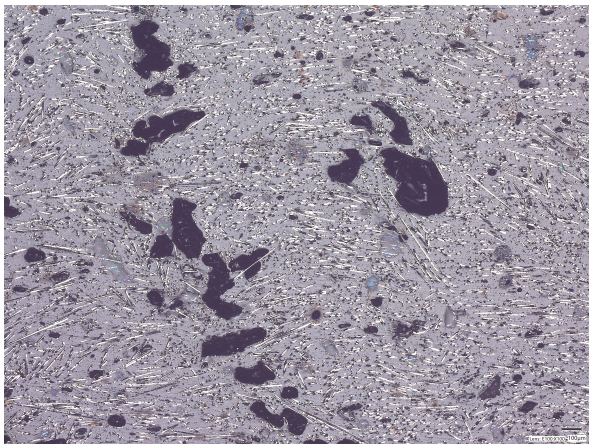

Figure 6.12: Microscopic picture of PESU parallel cross-section at x100 magnification of volumetric output 840 mm^3/s.

Comparing a microscopic picture at the volumetric output of 120 mm^3/s to 840 mm^3/s as shown in figures 6.12 an 6.11, respectively. Both show relatively big voids; however, at a volumetric output of 120 mm^3/s, it is more homogenous dispersed than at a volumetric output of 840 mm^3/s.

6.1.4. Temperature heating zones

This subsection presents the results and result discussion of the influence of temperature of the heating zones performed on PPS. Where in figure 6.13, the averages of measured parameters like torque, screw speed, nozzle pressure and void contents in both parallel and perpendicular cross-sections are plotted against the heating zone 4 temperature. With each heating zone ten degrees lower than the one before, the following input settings are given in table 5.5

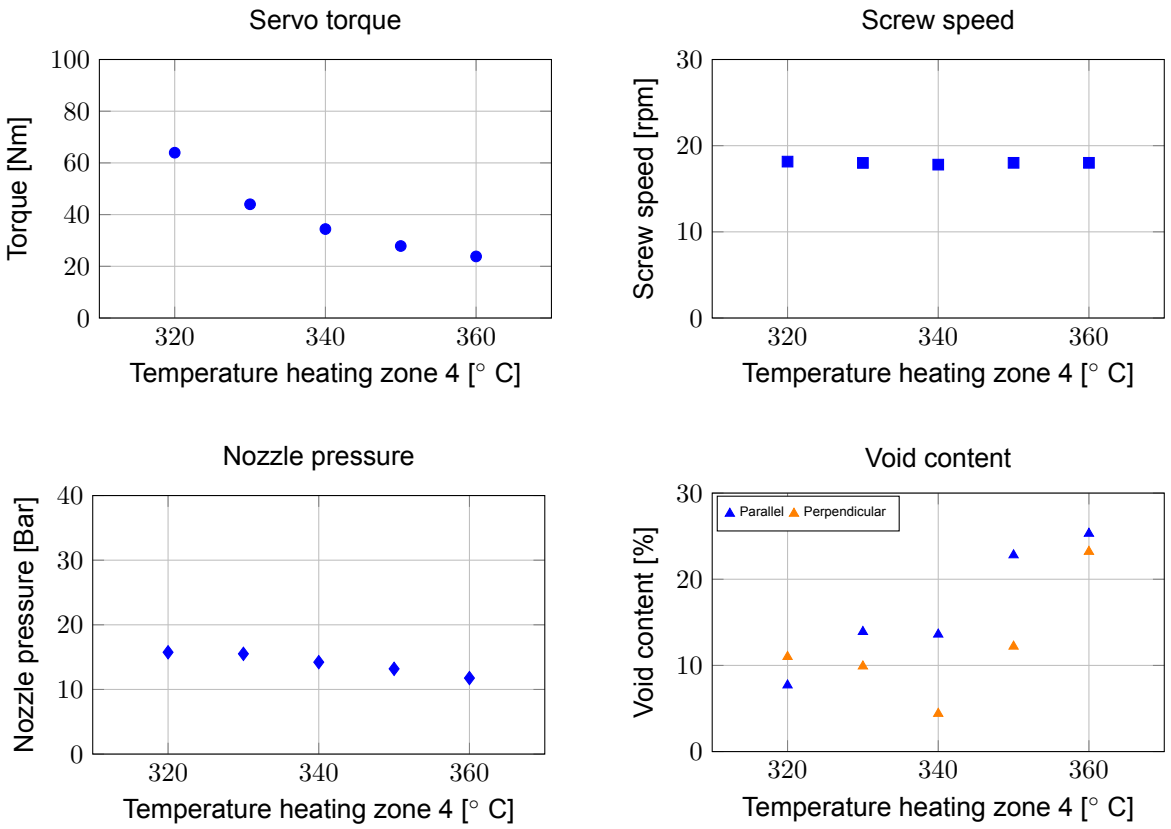

Figure 6.13: Result plots of averages of the measured parameters and void content versus the temperature of heating zone 4 for PPS.

The servo torque decreases with increasing heating zones temperatures, indicating less force is needed by the servo. Indicating higher heating zone temperature increases the printability of PPS due to decreasing friction or viscosity in one region. However, due to the increase of all heating zones, it is unknown which heating zone region is creating the torque.

The screw speed stays constant, as expected. Nozzle pressure decreases with increasing heating zones temperatures.

The nozzle pressure drops with increasing heating zone temperatures, which makes sense as viscosity decreases with increasing temperature following the Arrhenius equation as given in equation 2.6.

Temperature hz4 [$°C$]	**Cross-section** [$-$]	**Avg void** [%]	**std void** [%]	**Avg max area** [$*10^3\ \mu m^2$]	**Std max area** [$*10^3\ \mu m^2$]
320	Parallel	7.7	3.8	30.7	8.5
320	Perpendicular	11.0	0.9	6.4	0.8
330	Parallel	13.9	1.2	29.7	6.6
330	Perpendicular	9.9	1.4	5.0	0.7
340	Parallel	13.6	3.5	41.0	11.5
340	Perpendicular	4.4	2.7	8.5	1.9
350	Parallel	22.8	3.4	36.4	6.6
350	Perpendicular	12.2	3.1	20.8	4.9
360	Parallel	25.3	2.1	76.6	18.8
360	Perpendicular	23.2	2.8	23.1	3.3

Table 6.3: Void content results different heating zone 4 temperature for PPS.

The results from both the void content versus heating zone 4 temperature graph and table 6.3 shows an increase in average void content when heating zone 4 is increased to 350 degrees Celsius. Indicating that increasing heating zones temperature is not always a viable solution for increasing printability by lowering torque as it can increase void content.

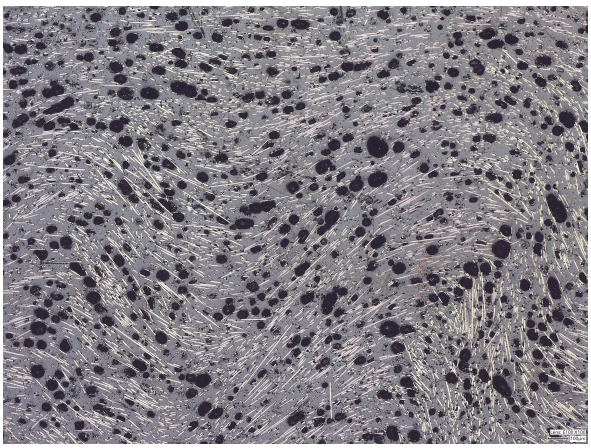

Figure 6.14: Microscopic picture of PPS parallel cross-section at x100 magnification with heating zone 4 temperature of 330 degrees Celsius

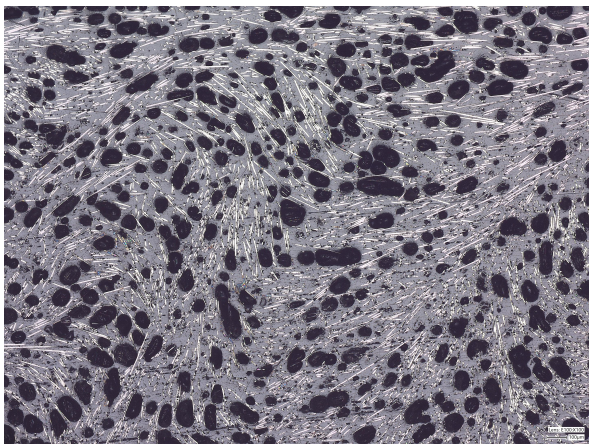

Figure 6.15: Microscopic picture of PPS parallel cross-section at x100 magnification with heating zone 4 temperature of 360 degrees Celsius

Comparing a microscopic picture with heating zone 4 temperature of 320 and 360 degrees Celsius, as shown in figures 6.14 and 6.15, respectively. Shows a clear increase in void sizes. This could be linked to less pressure in the nozzle, meaning the voids are less compressed, or due to lower viscosity, the voids are able to merge into bigger voids.

6.1.5. Nozzle pressure influence

This subsection presents the results and result discussion of the influence of nozzle pressure influence performed on PESU. The interesting findings in the volumetric tests indicate that a minimum pressure is needed. To test this, the screw speed is the same for different nozzle sizes, following the input settings from table 5.6.

Where figure 6.4 shows the results of the average nozzle pressure, average void content, standard deviation of the average void content and the average and standard deviation of the maximum area.

Nozzle Diameter [mm]	**avg nozzle pressure** [Bar]	**avg void** [%]	**std void** [%]	**Avg max area** [$*10^3\ \mu m^2$]	**Std max area** [$*10^3\ \mu m^2$]
4	19.5	7.0	1.1	14.5	5.5
6	9.9	7.9	1.5	123.5	115.4
9	5.7	14.3	5.4	340.9	223.5

Table 6.4: Results influence pressure test.

The results are shown in table 6.4 and show no major difference between the void content for the pressures of 19.5 and 9.9 bar. However, the average maximum area and standard deviation do differ much, indicating that a lower pressure does not mean an increased void content but does influence the void size and distribution within the sample.

For even lower nozzle pressures of 5.7 bar there is an increase in the average void content and the standard deviation. Insinuating there is a lower limit need for the nozzle pressure needed somewhere between 10 and 6 bar. This is lower than would be expected from the volumetric output tests given in figure 6.10.

The big standard deviation of void content for the 5.7 bar results also indicates the voids are not spread out evenly over the bead, furthermore the average and standard deviation of the maximum area also indicates large voids unevenly spread out over the sample. This could be due to the nozzle pressure not creating enough back pressure, potentially limiting the ability of air entrapped between granulates to be pushed out along the screw channel.

6.2. Design influence

This section gives the results for the second subquestion of *Which aspect of extruder design influences the printability and the microstructure of high-temperature polymer prints, and how could they be improved to minimize void content?*

6.2.1. Nozzle insulation test Polyphenyl sulphide (PPS)

The volumetric output test with nozzle insulation is compared to those performed without insulation from section 6.1.3.1.

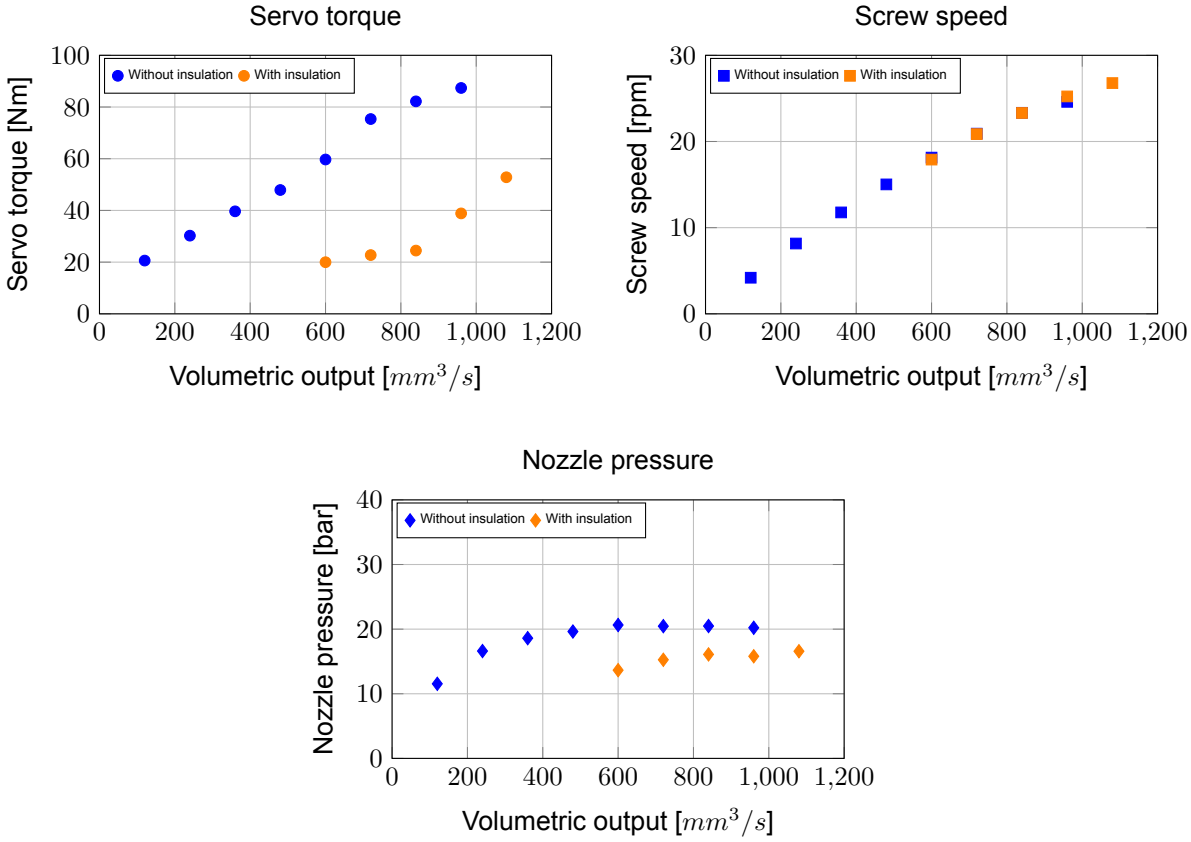

Figure 6.16: Result plots of averages of the measured parameters versus the volumetric output for PPS, with and without an insulated nozzle.

The results show that nozzle insulation reduces the required servo torque, which benefits the printability of PPS. Interestingly, the servo torque is even lower than that observed in the heating zone temperature tests, indicating that the nozzle was the governing factor for the high torque. However, the torque increases more rapidly beyond a volumetric output of 860 mm^3/s, suggesting that something in the extruder changes, requiring more torque. Based on testing experience, this may be due to insufficient heat transfer to the granulate at higher volumetric outputs, particularly in heating zone 1. If melting does not initiate before reaching heating zone 2, solid granulate is compressed in the compression zone, leading to a higher torque requirement. A simple solution is to increase the temperature of heating zone 1.

The screw speed stays consistent as expected, and the nozzle pressure decreases. This decrease in nozzle pressure indicates a decrease in viscosity due to less heat loss in the nozzle. This influences the servo torque needed,d indicating the system has a problem when viscosity decreases in the nozzle.

The nozzle insulation also has an interesting influence on fibre orientation. Normally, a wavy pattern with random orientations is visible, as shown in figure 6.17. However this waviness becomes less with nozzle insulation as shown in figure 6.18. Now the hypothesis of the creation of the wavy pattern is due to the spinning of the screw exerting a rotational force on the molten polymer present in the nozzle. This decreases due to lower viscosity in the nozzle.

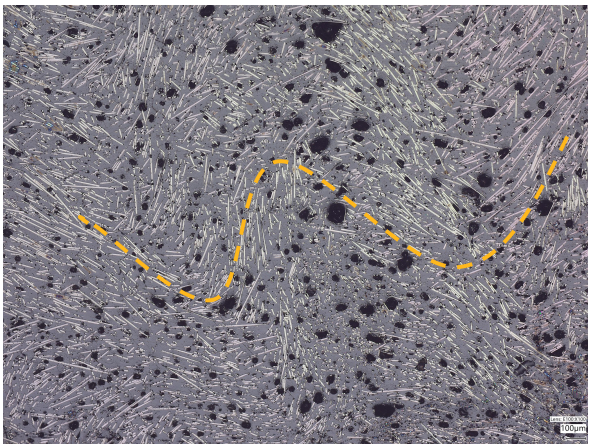

Figure 6.17: Microscopic picture of PPS parallel cross-section at x100 magnification for volumetric output of 600 mm^3/s without nozzle insulation.

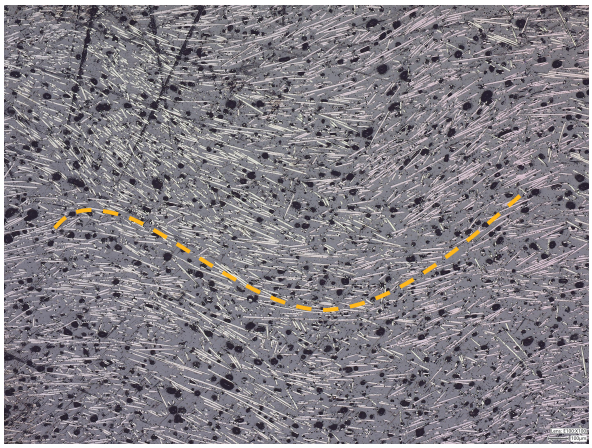

Figure 6.18: Microscopic picture of PPS parallel cross-section at x100 magnification for volumetric output of 600 mm^3/s with nozzle insulation.

In the horizontal printing direction, the striped orange-yellow lines visualize the approximate fibre orientation. The hypothesis regarding the influence of viscosity and screw rotation appears to be supported by the increased waviness observed at higher volumetric outputs, as shown in Figures 6.19 and 6.20, for cases without and with nozzle insulation.

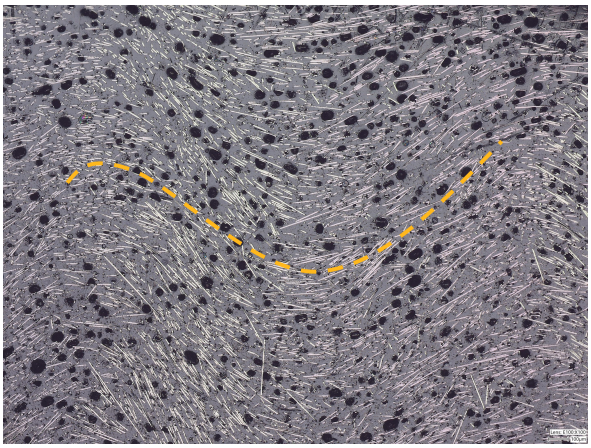

Figure 6.19: Microscopic picture of PPS parallel cross-section at x100 magnification for volumetric output of 1080 mm^3/s without nozzle insulation.

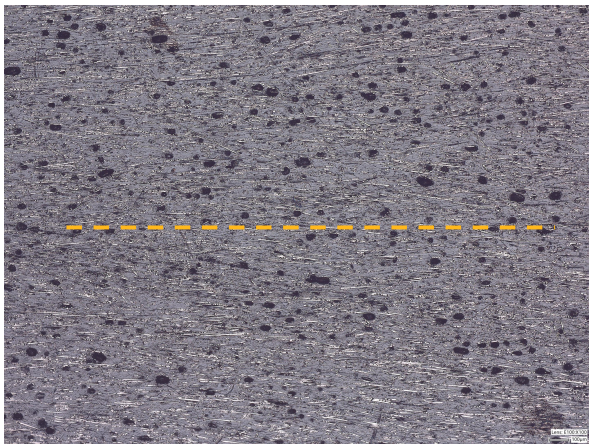

Figure 6.20: Microscopic picture of PPS parallel cross-section at x100 magnification for volumetric output of 1080 mm^3/s with nozzle insulation.

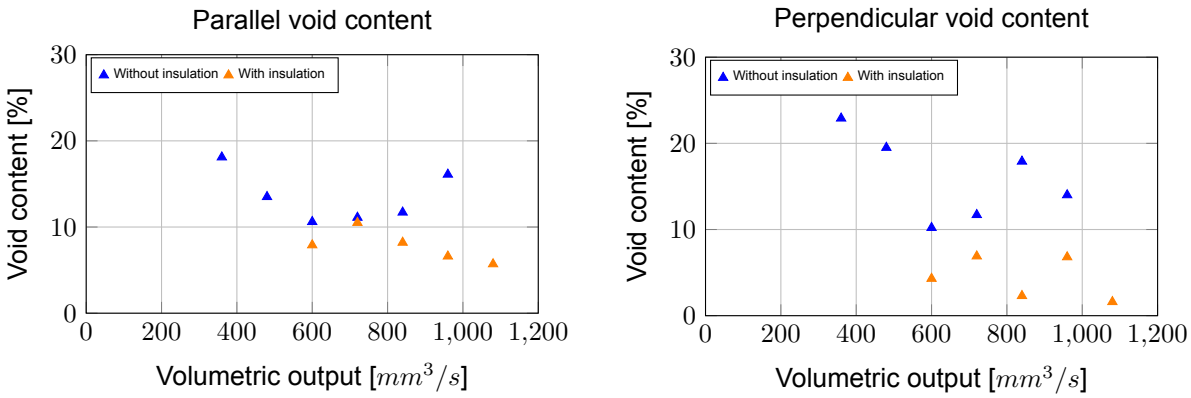

Figure 6.21: Void content vs volumetric output test results plots for both cross-section directions comparing results without and with insulation.

Volumetric output [mm^3/s]	**Cross-section** [$-$]	**Avg void** [%]	**std void** [%]	**Avg max area** [$*10^3$ μm^2]	**Std max area** [$*10^3$ μm^2]
600	Parallel	7.9	0.8	6.4	1.3
600	Perpendicular	4.3	1.6	5.5	1.6
720	Parallel	10.5	1.9	6.3	0.7
720	Perpendicular	6.9	1.4	5.0	0.6
840	Parallel	8.2	1.6	13.8	3.8
840	Perpendicular	2.3	0.4	7.7	2.2
960	Parallel	6.6	0.7	5.5	0.6
960	Perpendicular	6.8	1.3	4.7	0.8
1080	Parallel	5.7	1.3	6.1	0.9
1080	Perpendicular	1.6	0.4	2.5	0.4

Table 6.5: Void content volumetric output tests results of PPS with insulated nozzle.

The results from the graphs in fig 6.21 and the results in table 6.5 indicate a positive effect of nozzle insulation on the average void content and all have relative small average maximum areas.

6.2.2. Nozzle insulation test Polyethersulphone (PESU)

The problem with nozzle clogging was not observed with PESU. However, due to the overall positive effect seen in the PPS insulation tests, the same volumetric output tests with nozzle insulation are performed and compared to those without nozzle insulation from section 6.1.3.2.

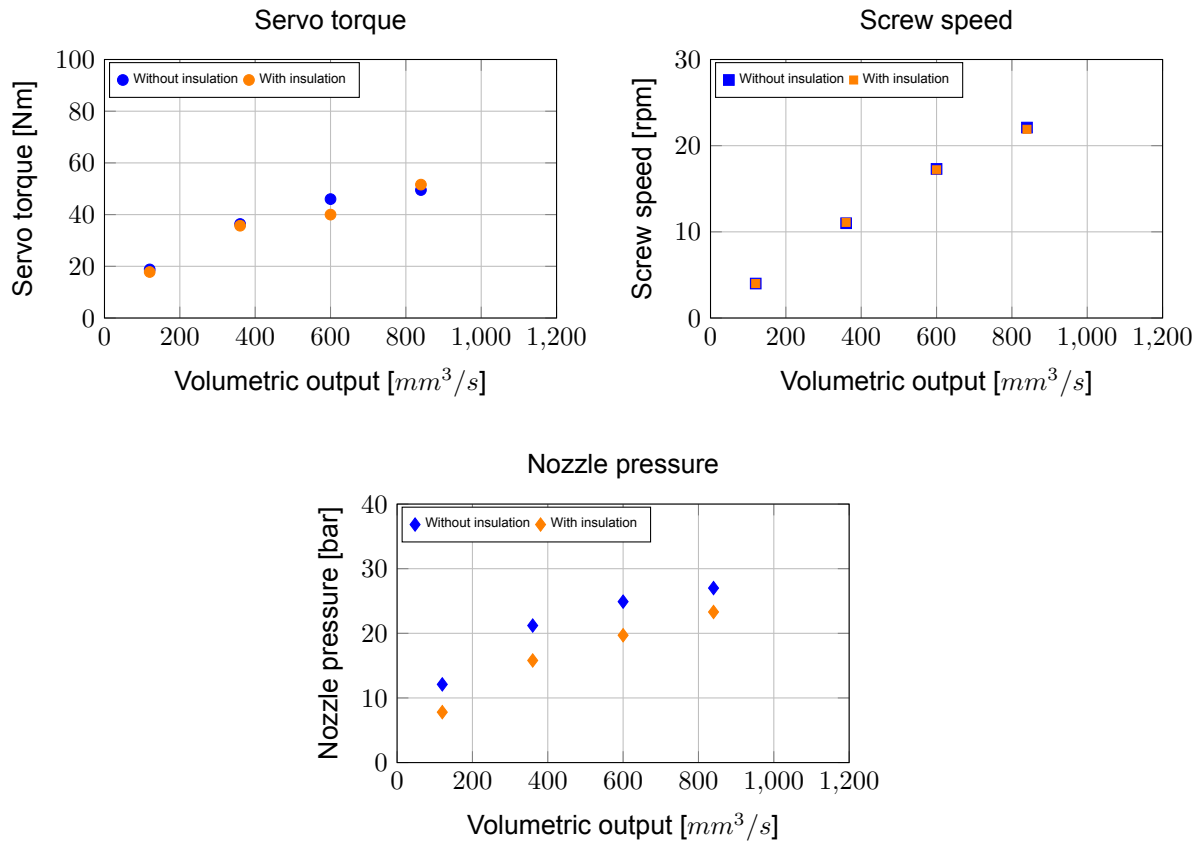

Figure 6.22: Result plots of averages of the measured parameters versus the volumetric output for PESU, with and without an insulated nozzle.

The results show no difference for both the servo torque and screw speed. Indicating that the heat loss in the nozzle is not the limiting factor for PESU. For the nozzle pressure, a decrease is observed, indicating a decrease in viscosity in the nozzle, as also seen for PPS.

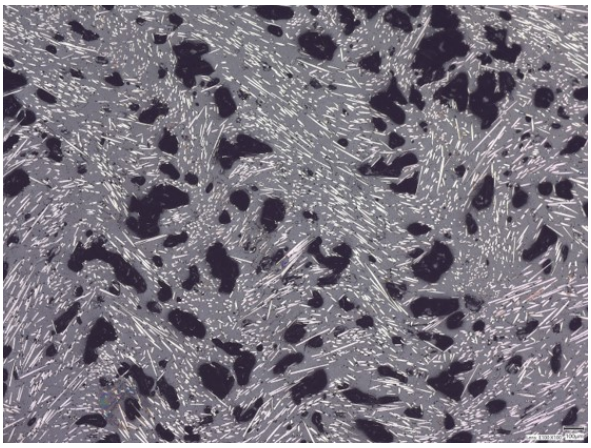

Figure 6.23: Microscopic picture of PESU parallel cross-section at x100 magnification for volumetric ouput of 120 mm^3/s without nozzle insulation.

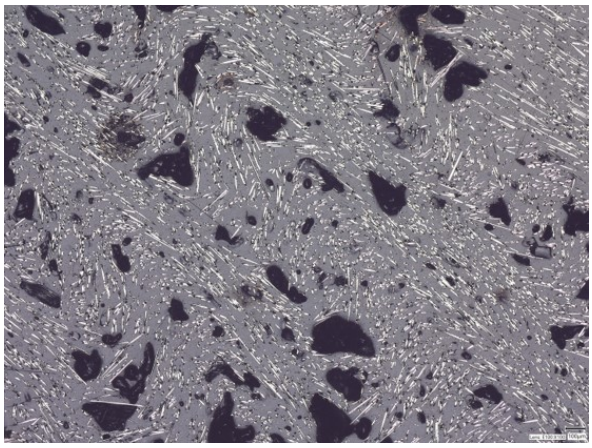

Figure 6.24: Microscopic picture of PESU parallel cross-section at x100 magnification for volumetric ouput of 120 mm^3/s with nozzle insulation.

Examining the microscopic pictures of PESU at volumetric output of 120 mm^3/s without and with nozzle insulation as shown in figure 6.23 and 6.24, respectively, reveals little difference in waviness pattern of the fibres.

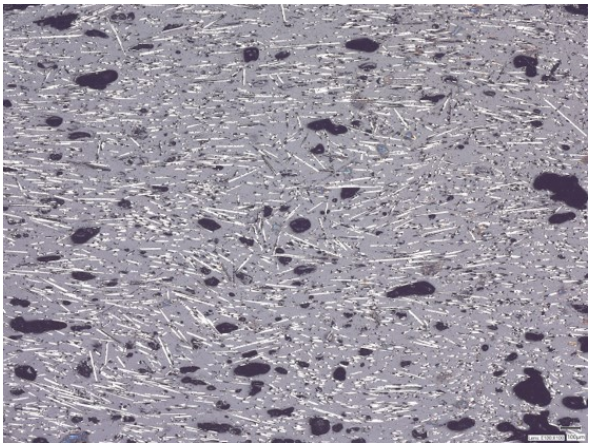

Figure 6.25: Microscopic picture of PESU parallel cross-section at x100 magnification for volumetric output of 840 mm^3/s without nozzle insulation.

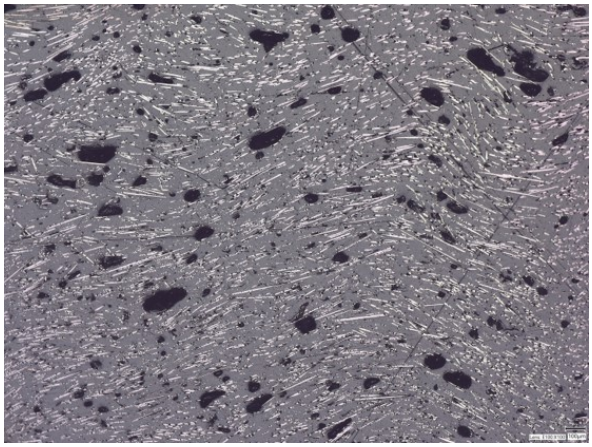

Figure 6.26: Microscopic picture of PESU parallel cross-section at x100 magnification for volumetric output of 840 mm^3/s with nozzle insulation.

At higher volumetric outputs, as shown in figure 6.25 and 6.26, for cases without and with nozzle insulation, respectively, no noticeable difference is observed. However, similar to PPS, the waviness pattern decreases with increasing volumetric output.

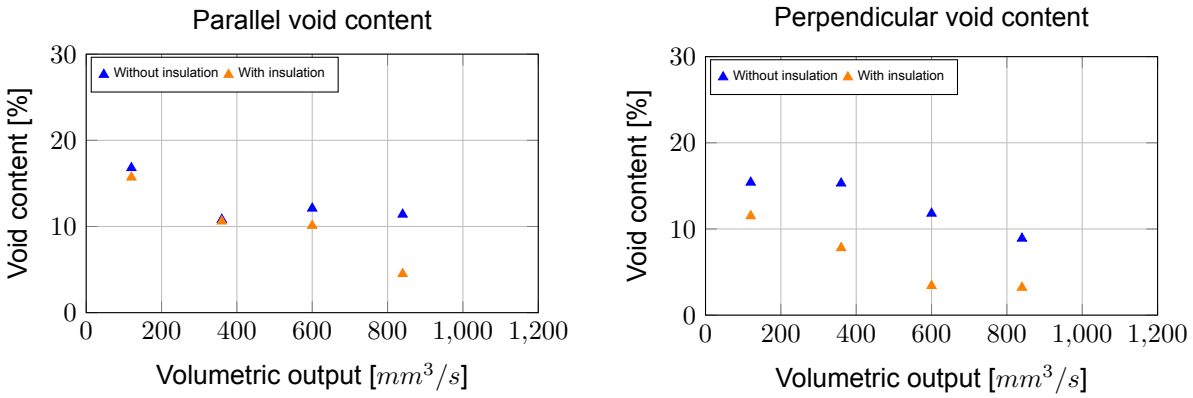

Figure 6.27: Void content vs volumetric output test results plots for both cross-section directions comparing results without and with insulation.

Volumetric output [mm^3/s]	**Cross-section** [–]	**Avg void** [%]	**std void** [%]	**Avg max area** [$*10^3$ μm^2]	**Std max area** [$*10^3$ μm^2]
120	Parallel	15.7	2.1	97.7	56.2
120	Perpendicular	22.9	3.7	57.0	31.8
360	Parallel	10.6	7.5	128.8	145.4
360	Perpendicular	7.8	0.9	34.5	18.9
600	Parallel	10.1	10.0	261.1	527.2
600	Perpendicular	3.4	0.9	13.3	6.5
840	Parallel	4.5	1.0	14.3	2.5
840	Perpendicular	3.2	0.9	11.2	6.8

Table 6.6: Void content volumetric output tests results of PESU with insulated nozzle.

The results from the graphs in figure 6.22 and the data results in table 6.6 indicate no major difference in average void content in the parallel cross-section direction. However, the maximum area measurements show high averages and standard deviations, suggesting the presence of large voids that are not evenly dispersed throughout the sample. Instead, these voids appear to accumulate and form larger voids due to the lower viscosity, which is an undesirable effect. This suggests that the issue in PESU is not primarily in the nozzle area but is more likely related to heating zone 1.

Interestingly, there is a positive effect on void content in the perpendicular cross-section direction. This suggests that the voids either become smaller and more elongated or the likelihood of cutting through a large void in this direction is lower, meaning larger voids do not appear as frequently in the dataset.

7

Conclusion and Recommendations

This chapter contains the conclusion and the recommendations made for design improvements and further research possibilities.

7.1. Conclusion

In response to the main research question, *What is the influence of printing parameters, extruder design and material properties on printability and microstructure of high-temperature polymer prints?"*, the findings confirm that printing parameters have an impact on both printability and microstructure, with viscosity playing a key role. However, distinguishing whether this influence is primarily due to temperature effects or shear thinning of the polymer remains challenging. Additionally, improvements to the extruder design, such as nozzle insulation, can enhance printability and microstructure by reducing void content for semi-crystalline polymer composites.

To address the first sub-question, *"What is the influence of printing parameters on the printability and microstructure of high-temperature polymer composite prints?"*, we can refer to the results and discussions in Section 6.1, where all input parameters were analysed. Key findings are the high torque required to extrude PPS, which limits its printable range of volumetric outputs and the problem encountered of nozzle clogging, leading to printing issues. For PESU, the problem of insufficient heating in heating zone 1 was observed, which prevented the barrel from reaching the necessary temperature.

The influence on microstructure becomes evident when examining the volumetric output tests and heating zone temperature range tests. The data shows that viscosity plays a crucial role in the system, as higher void content is observed when the system does not function correctly. However, increasing heating zone temperatures is not always a solution, as seen in the test performed for PPS, where excessive heating negatively affects the void content.

To address the second sub-question, *"Which aspect of extruder design influences the printability and the microstructure of high-temperature polymer composite prints, and how could they be improved to minimize void content?"*, two conclusions can be drawn.

Heat loss at the nozzle greatly affects semi-crystalline polymers due to the drastic viscosity change near the crystallization temperature. This effect is less pronounced for amorphous polymers, but lowering viscosity leads to fewer yet larger voids that are unevenly distributed across the sample, which is undesirable.

Problems arise in heating zone 1 due to the big temperature difference between the granulate and barrel. The heating band is insufficiently powerful to heat the barrel and granulate, making it a limiting factor in the extruder design. The next section discusses recommendations for improvement.

7.2. Recommendations

An overview of all the sections, the problem arising and possible solutions are shown in figure 7.1. Furthermore, this chapter will explain all the recommendations for CEAD to increase printability and reduce void content for high-temperature polymer composites and potential design upgrades.

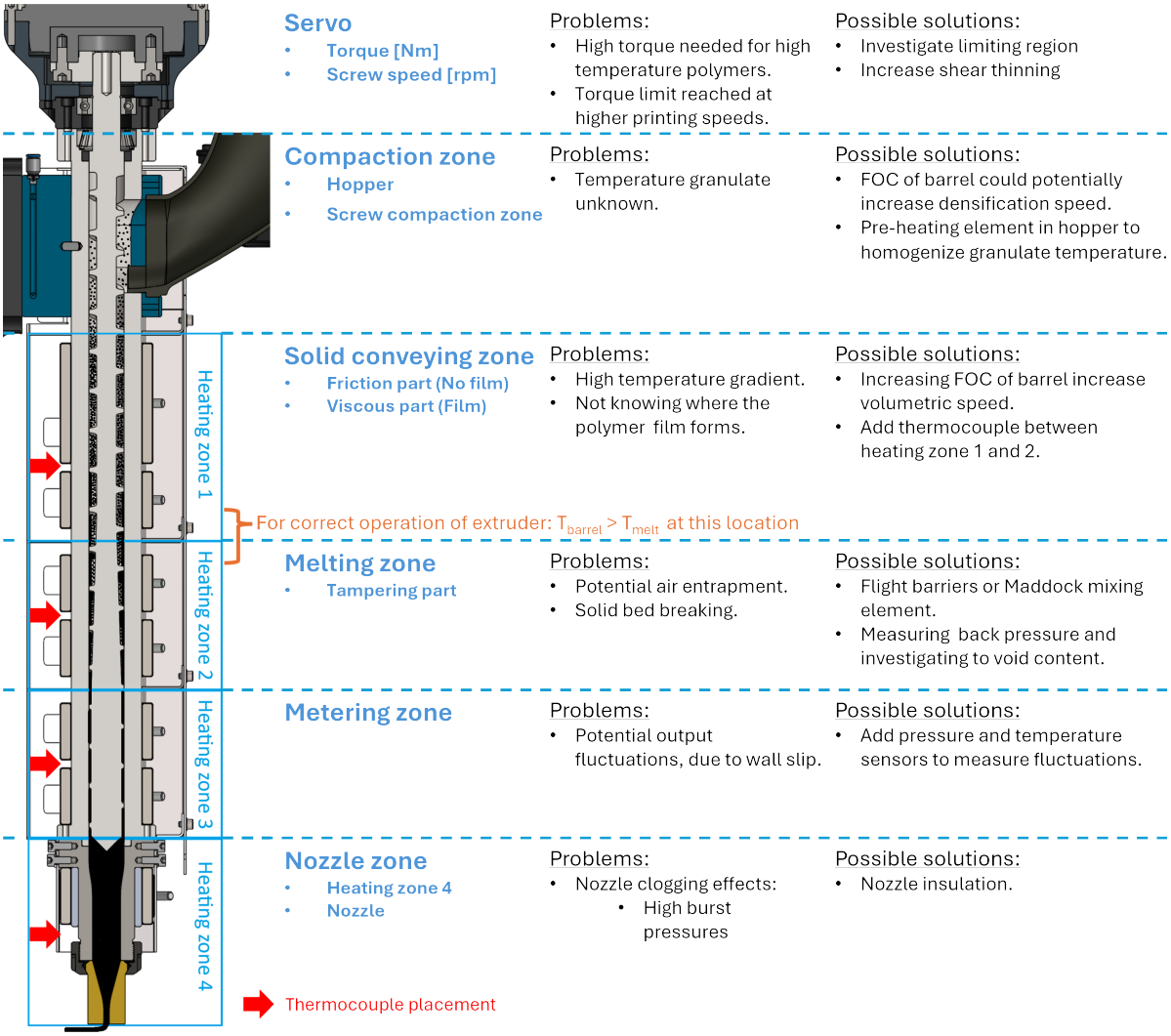

Figure 7.1: Extruder overview with the different regions, problems and possible solutions.

7.2.1. Nozzle viscosity measurement design

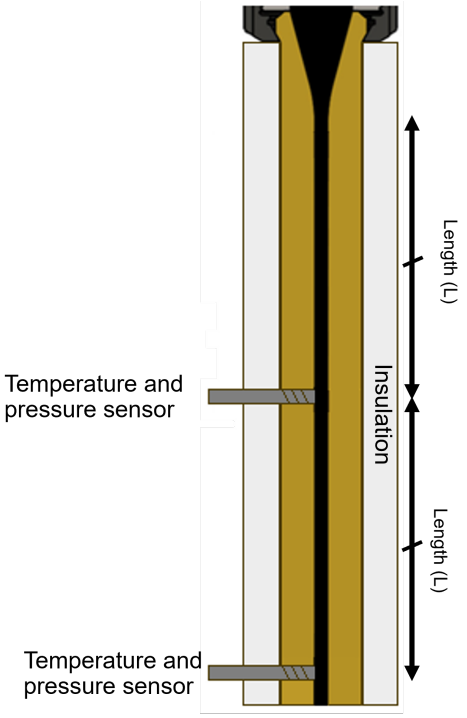

Figure 7.2: Viscosity measuring nozzle design

The data indicates an influence of temperature and volumetric output on the viscosity of the polymer melt. However, isolating these two components is difficult in the current test setup. To investigate this, high-temperature rheology tests can be performed. However, these tests are costly. Therefore, A recommendation for a nozzle design with two pressure and temperature sensors is suggested, as shown in figure 7.2. It is important that the temperature does not change much over the length of the nozzle. This can be done by using proper insulation material or using heating elements. The nozzle length is taken to ensure the viscosity is measured under laminar flow. This means it needs to be at least ten times the diameter of the nozzle channel. This setup is relatively cheap and easy to implement, which can give valuable insight into viscosity changes for different volumetric outputs and temperatures for various materials and material grades.

7.2.1.1. Volumetric output

The first step is to determine the volumetric output; this is done by weighing the extruded material, measuring the time of extrusion, and using the density provided by the material supplier. Using equation 7.1, the volumetric flow is calculated.

$$Q_v = \frac{m_{ex}}{\rho * t_{ex}} \tag{7.1}$$

By measuring the pressure difference over a range of volumetric outputs, the power law index n and the flow consistency index k can be determined with the Hagen-Poiseuille equation for power law cases shown in equation 7.2 [8].

$$Q_v = \frac{n}{3n+1} * \pi * R_n^3 * \left(\frac{R_n}{2k} * \frac{dp}{dz}\right)^{\frac{1}{n}} \tag{7.2}$$

Plotting the volumetric output's natural logarithmic values against the pressure differences natural logarithmic values should create a linear relationship as given by equation 7.3.

$$ln(Q_v) = ln\left(\frac{n}{3n+1} * \pi * R_n^3\right) + \frac{1}{n} ln\left(\frac{R_n}{2k}\right) + *\frac{1}{n} ln\left(\frac{dp}{dz}\right) \tag{7.3}$$

To determine the power law index n and the flow consistency index k, a linear trend line is used where the slope given in equation 7.4 denoted as b is equal to $\frac{1}{n}$. The determined power law index is used in the part of the equation which is equal to C as given by 7.5 and rewrite it to equation 7.6 to calculate the flow consistency index.

$$y = C + b * x \tag{7.4}$$

$$C = ln\left(\frac{n}{2n+1} * \pi * R_n^3\right) + \frac{1}{n} ln\left(\frac{R_n}{2k}\right) \tag{7.5}$$

$$k = \frac{R_n}{2} * e^{-n*C} * \left(\frac{n * \pi * R_n^3}{3n+1}\right) \tag{7.6}$$

Knowing the power law and flow consistency indexes opens opportunities to calculate the viscosity using equation 7.8 [8]. Therefore, the shear rate at the wall needs to be determined. This is done by using equation 7.7 [27], with the assumption of no-slip condition.

$$\dot{\gamma}_w = \frac{3n+1}{4n} * \frac{4Q}{\pi * R_n^3} \tag{7.7}$$

$$\mu = -k * \dot{\gamma}_w^{n-1} \tag{7.8}$$

7.2.1.2. Temperature

Using the volumetric output tests as described in section 7.2.1.1 for different temperatures allows for determining the material properties of activation energy E_a and the pre-exponential factor A using the Arrhenius equation given by equation 7.9.

$$\mu = A * e^{\frac{E_a}{R*T}} \tag{7.9}$$

When the viscosity is measured over a temperature range, the natural logarithm of the viscosity $\ln(\mu)$ can be plotted against the inverse temperature $\frac{1}{T}$ should create a linear relationship as shown in equation 7.10. The slope of this trend line is equal to the activation energy E_a dived by the gas constant R, and the interception with the y-axis is equal to the natural logarithmic of the pre-exponential factor $\ln(A)$.

$$\ln(\mu) = \ln(A) * \frac{E_a}{R} * \frac{1}{T} \tag{7.10}$$

The idea of using a viscosity measuring nozzle can be extended to other regions, such as investigating the influence of roughness without needing to change anything inside the extruder itself, reducing cost and increasing practicability.

So, the use of a viscosity-measuring nozzle can give insight into the influence of temperature and shear rate on the viscosity. This makes it possible to investigate material properties such as the power law index, consistency index, and activation energy. Opening possibilities to better understand the viscosity behaviour in different regions of the extruder and creating possibilities for optimizing the input parameters for different volumetric outputs.

7.2.2. Extruder design changes

This subsection contains the recommendations for the extruder design.

7.2.2.1. Recomendation barrel

Adding more temperature and pressure sensors for the barrel is advised to provide greater insight into the extruder's internal conditions. This would help identify problem areas and determine whether melting occurs at the correct position inside the extruder. Together with the viscosity measuring nozzle, this can essentially create a clearer view of the extrusion process, which is currently lacking, making it difficult to isolate and fully understand system behaviour.

The specific placement of temperature and pressure sensors, as shown in figure 7.3, opens many possibilities to divide the different sections. The pressures at the start and end of the compression zone area is of particular interest as this allows us to measure the back pressure generated in this section, which is one of the main mechanisms currently placed to reduce void content. Measuring this back pressure could potentially result in a back pressure threshold per material needed to achieve a desired constant void content.

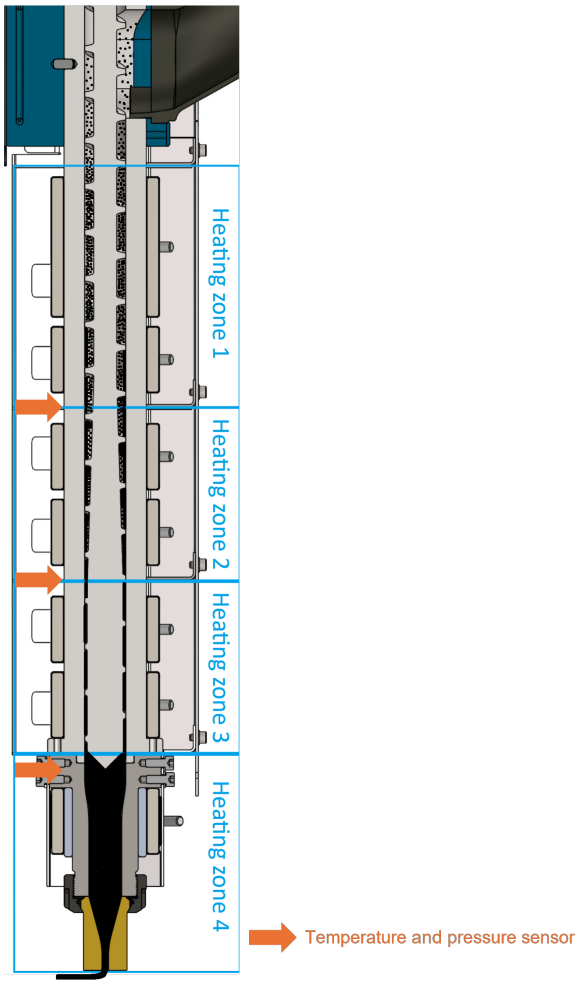

Figure 7.3: Extruder with recommended temperature and pressure sensors.

Additionally, by adding the pressure and temperature sensors, different screw designs, such as barrier screws, Maddock mixing elements, or CRDZ screw designs, could be tested. Investigating the influence of surface roughness on the system may also lead to potential improvements. An interesting solution could be optimizing roughness levels in different regions of the extruder, depending on their function.

7.2.2.2. Recommendation hopper

The conclusion highlights that the heating band in heating zone 1 is not powerful enough to maintain the desired barrel temperature. Therefore, using a more powerful heating band is proposed as a solution. However, due to the poor heat conduction of polymers, simply increasing the power of the heating band or raising the temperature of heating zone 1 could lead to polymer degradation caused by a high-temperature gradient.

To address this, it is suggested that the use of heated hoppers be investigated to homogenize the temperature before the granulate enters the extruder. An example of a hopper design is given in figure 7.4, which used insulation material to mitigate heat loss and good thermal conductivity material like aluminium could be used to better homogenise the heat to the granulate. This could be particularly important for larger extruders with higher volumetric outputs as the issue becomes more pronounced at greater scales.

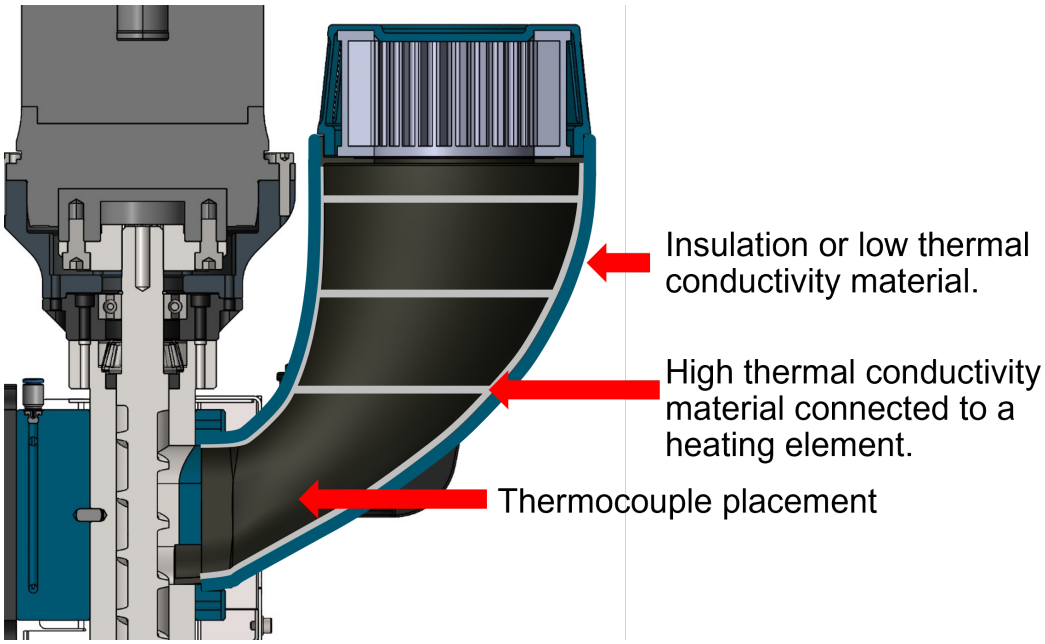

Figure 7.4: Hopper design improvement

A

Materials data-sheets

This appendix contains all the material data-sheets provided by material suppliers.

A.1. Datasheet Polyphenylene sulfide (PPS)

	Methode	Eenheid	KTA2023/240
Materiaal			Witcom PPS-2023/240 Black 50% PIR
Lotnummer			2231137
IZOD kerfslagsterkte	ISO 180/1A	kJ/m^2	6,2
Melt Volume Rate (315C/5kg)	ISO 1133	cc/10 min	13,8
Oppervlakte Weerstand - between	ASTM D257	Ohm/sq	330
Soortelijk Gewicht	ISO 1183	kg/l	1,44

Figure A.1: Datasheet of PPS

A.2. Datasheet Polyehersulfone (PESU)

Electrafil® PESU 1810 3DP

Techmer Polymer Modifiers - Polyethersulfone Monday, November 14, 2022

General Information

General	
Material Status	• Commercial: Active
Availability	• North America
Features	• Electrically Conductive
Appearance	• Natural Color
Forms	• Pellets
Processing Method	• 3D Printing, Fused Filament Fabrication (FFF)

ASTM & ISO Properties [1]

Physical	Nominal Value	Unit	Test Method
Density / Specific Gravity	1.46	g/cm³	ASTM D792
Mechanical	**Nominal Value**	**Unit**	**Test Method**
Tensile Modulus	17200	MPa	ASTM D638
Tensile Strength (Yield)	159	MPa	ASTM D638
Tensile Elongation (Break)	2.0	%	ASTM D638
Flexural Modulus	15900	MPa	ASTM D790
Flexural Strength	248	MPa	ASTM D790
Compressive Modulus	5520	MPa	ASTM D695
Compressive Strength	183	MPa	ASTM D695
Impact	**Nominal Value**	**Unit**	**Test Method**
Notched Izod Impact (23°C, 3.18 mm)	64	J/m	ASTM D256
Thermal	**Nominal Value**	**Unit**	**Test Method**
Deflection Temperature Under Load			ASTM D648
0.45 MPa, Unannealed	224	°C	
Deflection Temperature Under Load			ASTM D648
1.8 MPa, Unannealed	222	°C	
Specific Heat	1440	J/kg/°C	ASTM C351
Electrical	**Nominal Value**	**Unit**	**Test Method**
Surface Resistivity	2.0 to 6.0	ohms	ASTM D257

Processing Information

Injection	Nominal Value	Unit
Drying Temperature	138	°C
Drying Time	3.0 to 6.0	hr
Suggested Max Moisture	< 0.040	%
Rear Temperature	288 to 304	°C
Middle Temperature	316 to 343	°C
Front Temperature	349 to 382	°C
Nozzle Temperature	343 to 371	°C
Processing (Melt) Temp	349 to 385	°C

Injection Notes

If material is to remain in dryer for more than 6 hours in dried state, reduce dryer temperature to 150°F to prevent degradation of material.

Figure A.2: Datasheet of PESU

A.3. Datasheet Polycarbonate (PC)

TECHNICAL DATA

Physicals	Typical Values	Test Method
Base Polymer	Modified PC	
Reinforcements	Carbon Fibre	
% Fibre Loading	20%	
Tensile Strength		
X Direction	112,4 MPa	Modified ASTM D638
Z Direction	50,3 MPa	Modified ASTM D638
Tensile Modulus		
X Direction	11 GPa	Modified ASTM D638
Z Direction	3,0 GPa	Modified ASTM D638
Flexural Strength		
X Direction	180 MPa	Modified ASTM D790
Z Direction	93,8 MPa	Modified ASTM D790
Flexural Modulus		
X Direction	10,8 GPa	Modified ASTM D790
Z Direction	3,8 GPa	Modified ASTM D790
HDT, 1,82 MPa, 3,22 mm	144°C	ASTM D648 (Annealed)
Density as Printed	1,21 g/cc	ASTM D792

*Where X is the bead print direction and Z is through the bead thickness.

Figure A.3: Datasheet of PC part 1

Physicals	Typical Value
Drying Temperature Inlet	245°F (118°C)
Drying Temperature Outlet	195°F (91°C)
Drying Time	5 hours
Post Drying Hold Temperature Inlet	195°F (91°C)
Post Drying Hold Temperature Outlet	145°F (118°C)
Maximum Moisture Content	0.02 %
Extruder Zone 1 Temp	530°F (277°C)
Extruder Zone 2 Temp	550°F (288°C)
Extruder Zone 3 Temp	570°F (299°C)
Extruder Zone 4 Temp	600°F (316°C)
Extruder Zone 5 Temp	600°F (316°C)
Extruder Nozzel Temp	640°F (338°C)
Post Print Annealing Required	No

Figure A.4: Datasheet of PC part 2

B

Critical F-value table

This appendix contains the F-table with a significance factor of 0.05 needed to determine the critical F-value.

$df_w \backslash df_B$	1	2	3	4	5	6	8	10	15	20	30
1	647	799	864	900	922	937	957	969	985	993	1001
2	38.5	39.0	39.2	39.2	39.3	39.3	39.4	39.4	39.4	39.5	39.5
3	17.4	16.0	15.4	15.1	14.9	14.7	14.5	14.4	14.2	14.2	14.1
4	12.2	10.65	9.98	9.60	9.36	9.20	8.98	8.84	8.66	8.56	8.46
5	10.0	8.43	7.76	7.39	7.15	6.98	6.76	6.62	6.43	6.33	6.23
6	8.81	7.26	6.60	6.23	5.99	5.82	5.60	5.46	5.27	5.17	5.07
7	8.07	6.54	5.89	5.52	5.29	5.21	4.90	4.76	4.57	4.47	4.36
8	7.57	6.60	5.42	5.05	4.82	4.65	4.43	4.30	4.10	4.00	3.89
9	7.21	5.71	5.08	4.72	4.48	4.32	4.10	3.96	3.77	3.67	3.56
10	6.94	5.46	4.83	4.47	4.24	4.07	3.85	3.72	3.52	3.42	3.31
15	6.20	4.77	4.15	3.80	3.58	3.41	3.20	3.06	2.86	2.76	2.64
20	5.87	4.46	3.86	3.51	3.29	3.13	2.91	2.77	2.57	2.46	2.35
30	5.57	4.18	3.59	3.25	3.03	2.87	2.65	2.51	2.31	2.20	2.07

Table B.1: Critical F-value table extracted from the book by Buijs [2]

C

Microscopy steps

This Appendix provides a detailed instruction on how to prepare the samples and on how to perform the void content measurements.

C.1. Sample preperation

This section gives a step-by-step guide on how to prepare the samples for microscopy.

1. Cut samples out of the print using a band say, as shown in figure C.1.
2. Grind the samples using grinding papers P180, P320, P800, P1200 and P2000 for around 30 seconds per grinding paper. Using the struers grinding machine, as shown in figure C.2.
3. Clean samples using an ultrasonic bath for at least 10 minutes.
4. Polish the sample with a medium-density molycloth with a 3-micrometer diamond paste for around 4 minutes. Using the Struers polishing machine, as shown in figure C.3.
5. Polish the sample with a medium-density napped cloth with a 1-micrometer diamond paste for around 5 minutes. Using the Struers polishing machine, as shown in figure C.3.
6. Clean and dry sample.

Note: The time steps are guidelines; however, check in between each step to see if the sample is ready for the next step; otherwise, continue grinding or polishing.

Figure C.1: The band saw used for sample cutting

Figure C.2: The Struers grinding machine.

Figure C.3: The Struers polishing machine.

C.2. Void content measurements

This section contains a step-by-step guide on void content measurements.

1. Level the sample and place it under the microscope.
2. Move to the sample and zoom in to x100 by selecting the x100 magnification as highlighted in figure C.4.

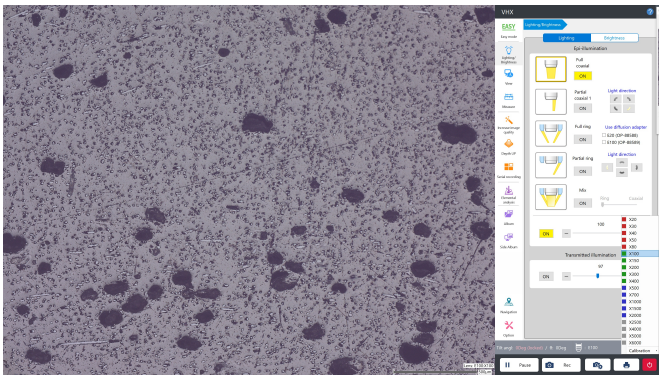

Figure C.4: Microscopic display highlighting the zoom.

3. Select mix illumination and make sure the slider is fully to the ring side as shown in figure C.5. Make a picture and save.

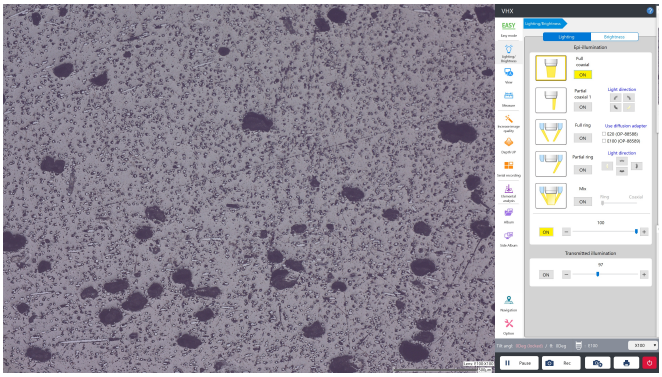

Figure C.5: Microscopic display showing the mix illumination settings.

4. Select the Full coaxial illumination, make a picture and save it.

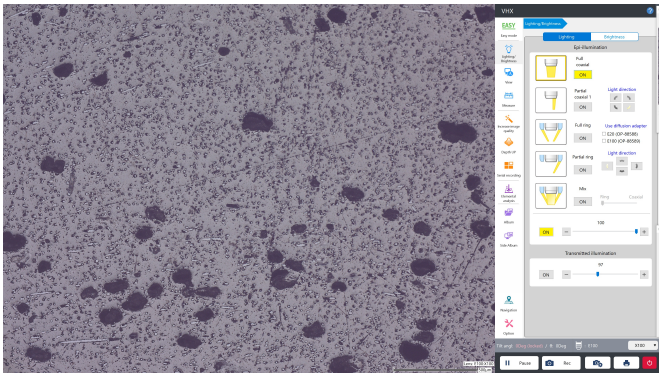

Figure C.6: Microscopic display highlighting the auto area measurement.

5. select the measuring tap to select the ”Auto-area measurement (grain count)” and choose the ”Brightness” setting as highlighted in figure C.7.

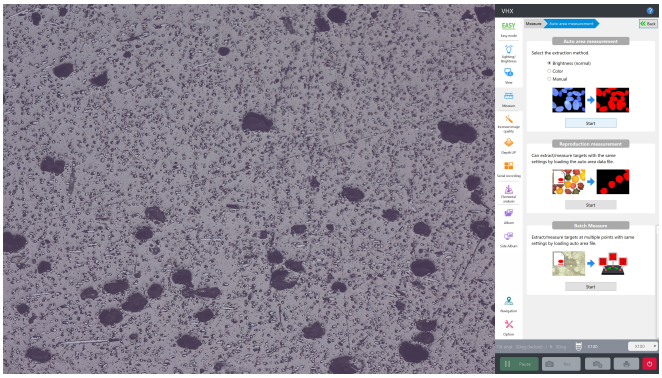

Figure C.7: Microscopic display highlighting the auto area measurement.

6. Select the ”Dark” setting, adjust the slider till the voids are selected correctly, and select ”Fill holes”. For the display set the slider to 50 as shown in figure C.8.

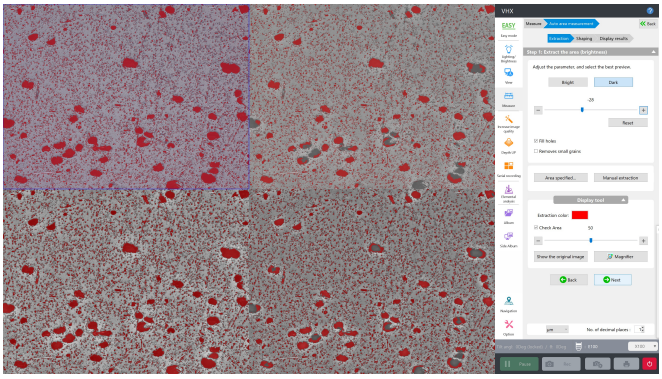

Figure C.8: Microscopic display showing the brightness selection settings.

7. Optional: Select a specific area by using the ”Area specified” button and select the area as shown in figure C.9.

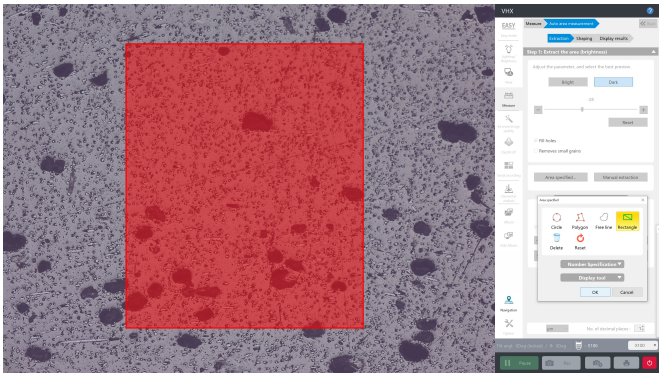

Figure C.9: Microscopic display showing the specific area selection.

8. Use the ”Eliminate grains” and set ”Upper limit” to 100 square micrometres and push the ”Apply” button as shown in figure C.10.

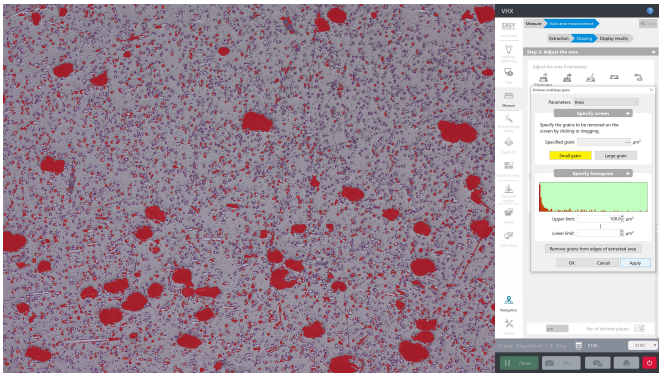

Figure C.10: Microscopic display showing the small grain elimination.

9. Click on the ”Measrued Results” and save the csv file. Also, save the image by using the ”Rec” button.

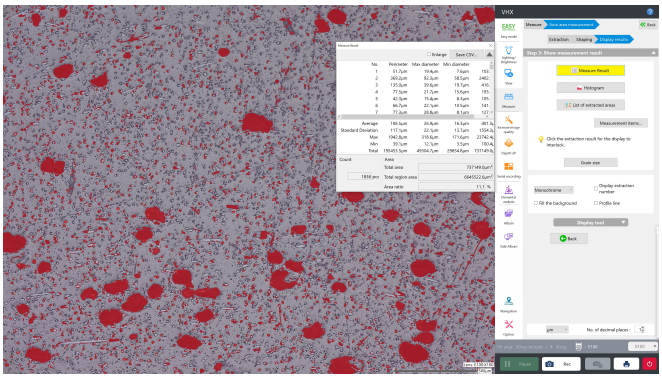

Figure C.11: Microscopic display showing the measured results selection.